
Systematic Data Extraction in High-Frequency Electromagnetic Fields

Systematische Datenextraktion aus Hochfrequenzfeldern

Zur Erlangung des akademischen Grades Doktor-Ingenieur (Dr.-Ing.)

genehmigte Dissertation von M.Sc. Todorka Banova aus Shtip

August 2014 — Darmstadt — D 17



TECHNISCHE
UNIVERSITÄT
DARMSTADT

Fachbereich Elektrotechnik und
Informationstechnik
Institut für Theorie
Elektromagnetischer Felder (TEMF)

Systematic Data Extraction in High-Frequency Electromagnetic Fields
Systematische Datenextraktion aus Hochfrequenzfeldern

Genehmigte Dissertation von M.Sc. Todorka Banova aus Shtip

1. Gutachten: Prof. Dr.-Ing. Thomas Weiland
2. Gutachten: Prof. Dr. rer. nat. habil. Ursula van Rienen

Tag der Einreichung: 22.04.2014

Tag der Prüfung: 21.07.2014

Darmstadt – D 17

Bitte zitieren Sie dieses Dokument als:

URN: [urn:nbn:de:tuda-tuprints-41170](https://nbn-resolving.org/urn:nbn:de:tuda-tuprints-41170)

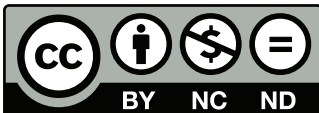
URL: <http://tuprints.ulb.tu-darmstadt.de/4117>

Dieses Dokument wird bereitgestellt von tuprints,

E-Publishing-Service der TU Darmstadt

<http://tuprints.ulb.tu-darmstadt.de>

tuprints@ulb.tu-darmstadt.de



Die Veröffentlichung steht unter folgender Creative Commons Lizenz:

Namensnennung – Keine kommerzielle Nutzung – Keine Bearbeitung 3.0 Deutschland

<http://creativecommons.org/licenses/by-nc-nd/3.0/de/>



Dedicated to my parents





Contents

Kurzfassung	vii
Abstract	ix
1. Introduction	1
1.1. Microwave Cavities	1
1.2. Motivation and Objective	2
1.3. Adequate Numerical Methods	4
1.4. Outline of the Thesis	7
2. Electrodynamics	9
2.1. Continuous Electrodynamics	9
2.1.1. The Maxwell's Equations	9
2.1.2. Material Equations	11
2.1.3. Boundary Conditions	12
2.1.4. Wave Equation	13
2.2. Discrete Electrodynamics	14
2.3. Finite Integration Technique	15
2.3.1. Spatial Discretization by Computational Grids	16
2.3.2. The Maxwell's Grid Equations	17
2.3.3. Properties of the Matrices	22
2.3.4. Material Discretization	22
2.3.5. Boundary Conditions	24
2.3.6. Time-Harmonic Fields (Frequency Domain)	25
2.3.7. Transient Fields (Time Domain)	27
2.4. Finite Element Method	29
2.4.1. Space Discretization	30
2.4.2. Solution Approximation	31
2.4.3. Equation Approximation	32
2.4.4. Matrix Assembly	36

3. Eigenvalue Extraction from Time-Domain Computations	39
3.1. Fourier Analysis	39
3.1.1. Fourier Series of Functions with Periodicity $2p$	40
3.1.2. The Fourier Transform	41
3.1.3. Transform Pairs	42
3.1.4. Properties of the Fourier Transform	45
3.1.5. Convolution	48
3.1.6. The Discrete Fourier Transform	50
3.2. Spectral Leakage	50
3.3. Windowing	54
3.4. Parametric Fitting	56
3.4.1. Parametric Fit with Library Models	56
3.4.2. Custom Parametric Fitting	57
3.4.3. Nonlinear Least Squares	57
3.5. Time-Domain Approach for Eigenfrequency Extraction	58
3.5.1. Field Simulation in Time Domain	58
3.5.2. Post-processing of the Time-Domain Computations	59
3.6. Extension of the Time-Domain Approach for Eigenfrequency Extraction	61
4. Eigenvalue Determination in Frequency Domain	63
4.1. Basic Lanczos Algorithm	63
4.1.1. Lanczos Algorithm with Shift-and-Invert	66
4.2. Lanczos Algorithm with Polynomial Filtering	67
4.2.1. Filtering Technique	67
4.3. B-Lanczos Algorithm	69
4.3.1. B-Lanczos Algorithm with Shift-and-Invert	70
5. Implementation Details	73
5.1. Time-Domain Approach	73
5.1.1. Limitations from the Finite Simulation Time	74
5.1.2. Fast Fourier Transformation	76
5.1.3. Technique for Locating a Gaussian Pulse	76
5.1.4. Fitting Models	77
5.1.5. Accuracy of the Time-Domain Approach	81
5.1.6. Robustness of the Time-Domain Approach	84
5.2. Frequency-Domain Approach	85
5.2.1. Numerical Setup	86
5.2.2. Lanczos Eigenvalue Solvers	86
5.2.3. Accuracy of the Frequency-Domain Approach	88
5.2.4. Robustness of the Frequency-Domain Approach	89

6. Simulation Results	91
6.1. Application Example: Billiard Cavity	91
6.1.1. Field Simulation in Time Domain	93
6.1.2. Accuracy of the Time- and the Frequency-Domain Approach	95
6.1.3. Robustness of the Time- and the Frequency-Domain Approach	96
6.1.4. Performance Analysis	99
6.1.5. Comparison with Other Eigenvalue Solvers	102
6.1.6. Scalability	105
6.1.7. Level-Spacing Analysis	108
6.2. Application Example: Dirac Billiard Cavity	112
6.2.1. Level-Density Analysis	112
7. Summary and Outlook	117
7.1. Contributions	117
7.2. Outlook	119
A. Fourier Transforms	121
Acronyms and Symbols	129
Acronyms	129
Roman Letters	130
Greek Letters	135
General Symbols and Conventions	136
Bibliography	145
Danksagung	147
Curriculum Vitae	149



Kurzfassung

Der Schwerpunkt dieser Arbeit liegt auf der Untersuchung von Billard Resonatoren mit ihren statistischen Eigenschaften der Eigenwertverteilung. Insbesondere werden supraleitende Mikrowellenresonatoren mit chaotischen Eigenschaften simuliert und dabei ihre Eigenfrequenzen bestimmt, die für die statistische Auswertung benötigt werden. Die Eigenfrequenzanalyse erfordert viele (in der Größenordnung von Tausend) Eigenfrequenzen, wobei die genaue Bestimmung der Werte von entscheidender Bedeutung ist. Im Rahmen dieser Arbeit decken die Forschungsinteressen folglich alle Aspekte von der numerischen Berechnung vieler Eigenwerte und Eigenvektoren bis hin zur Anwendungsentwicklung ab, um die zur Verfügung stehenden Distributed-Memory- und Shared-Memory-Multiprozessoren optimal auszunutzen. Außerdem gibt diese Arbeit einen Überblick zur Lösung großer Eigenwertprobleme durch eine detaillierte Auswertung der verwendeten numerischen Ansätze bezüglich der erzielbaren Genauigkeit, der Rechenzeiten und des Speicherbedarfs.

Der erste Ansatz für eine präzise Eigenfrequenzextraktion berücksichtigt den berechneten Zeitverlauf des elektrischen Feldes einer supraleitenden Resonanzstruktur. Bei Anregung des Hohlraums wird die elektrische Feldstärke an ausgewählten Beobachtungspunkten im Inneren des Hohlraums aufgenommen. Danach wird eine Fourier-Analyse der erfassten Signale durchgeführt und mittels Signalverarbeitungsverfahren und Anpassungstechniken die gewünschten Eigenfrequenzen auf der Basis optimierter Modellparameter extrahiert.

Der zweite numerische Ansatz basiert auf der numerischen Berechnung elektromagnetischer Felder im Frequenzbereich und verwendet die Lanczos Methode zur Eigenwertbestimmung. Basierend auf der Methode der Finiten Integration wird die numerische Lösung eines Standard-Eigenwertproblems betrachtet, um ein elektromagnetisches Problem für einen supraleitenden Resonator zu lösen. Entsprechend führt eine Diskretisierung desselben Problems mit Hilfe der Finiten Elemente Methode und gekrümmten Tetraedern auf ein großes verallgemeinertes Eigenwertproblem. Zu deren Lösung kombinieren die implementierten Lanczos Löser zwei Hauptbestandteile und verwenden einerseits den Lanczos-Algorithmus mit Polynom-Filterung sowie andererseits eine geeignete Parallelisierung der benötigten Algorithmen.



Abstract

The focus of this work is on the investigation of billiards with its statistical eigenvalue properties. Specifically, superconducting microwave resonators with chaotic characteristics are simulated and the eigenfrequencies that are needed for the statistical analysis are computed. The eigenfrequency analysis requires many (in order of thousands) eigenfrequencies to be calculated and the accurate determination of the eigenfrequencies has a crucial significance. Consequently, the research interests cover all aspects from accurate numerical calculation of many eigenvalues and eigenvectors up to application development in order to get good performance out of the programs for distributed-memory and shared-memory multiprocessors. Furthermore, this thesis provides an overview and detailed evaluation of the used numerical approaches for large-scale eigenvalue calculations with respect to the accuracy, the computational time, and the memory consumption.

The first approach for an accurate eigenfrequency extraction takes into consideration the evaluated electric field computations in Time Domain (TD) of a superconducting resonant structure. Upon excitation of the cavity, the electric field intensity is recorded at different detection probes inside the cavity. Thereafter, Fourier analysis of the recorded signals is performed and by means of signal-processing and fitting techniques, the requested eigenfrequencies are extracted by finding the optimal model parameters in the least squares sense.

The second numerical approach is based on a numerical computation of electromagnetic fields in Frequency Domain (FD) and further employs the Lanczos method for the eigenvalue determination. Namely, when utilizing the Finite Integration Technique (FIT) to solve an electromagnetic problem for a superconducting cavity, which encloses excited electromagnetic fields, the numerical solution of a standard large-scale eigenvalue problem is considered. Accordingly, if the numerical solution of the same problem is treated by the Finite Element Method (FEM) based on curvilinear tetrahedrons, it yields to the generalized large-scale eigenvalue problem. Afterward, the desired eigenvalues are calculated with the direct solution of the large (generalized) eigenvalue formulations. For this purpose, the implemented Lanczos solvers combine two major ingredients: the Lanczos algorithm with polynomial filtering on the one hand and its parallelization on the other.



1 Introduction

The eigenvalue calculations arise in many scientific and engineering application areas as well as in the computational science. Over the last years, the increasing number of applications has stimulated the development of new methods and software for the numerical solution of large-scale algebraic eigenvalue problems. At the same time, the realistic applications frequently challenge the limit of both computer hardware and numerical algorithms, as one might possibly need large number of eigen pairs located in a specified frequency range for matrices with dimension in excess of several millions. Particularly, structures with complicated geometry require a large number of grid points to achieve accurate simulation results. Thus, the thesis deals with the development of numerical techniques, which will use low computational costs during the accurate and robust calculation of thousands of eigenfrequencies for microwave cavities. In this introductory chapter of the thesis, the motivation for this work will be explained as well as the major challenges posed by the work will be stated.

1.1 Microwave Cavities

A device that exhibits resonant behavior is called a resonator. Inside the resonator the vibrations travel as waves, bouncing back and forth between its sides. The oppositely moving waves interfere with each other and create a pattern of standing waves. A resonator oscillates naturally at some frequencies with greater amplitude than at the others. These frequencies are called resonant frequencies and a resonator can have as many frequencies as it has degrees of freedom. In different application areas, the knowledge of the resonant frequencies has a great significance.

A special type of resonator, consisting of a closed metal structure that confines electromagnetic fields in the microwave region of the spectrum, is called a microwave cavity or Radio Frequency (RF) cavity [64]. In case that the shape of the microwave cavity is rectilinear and the medium inside is homogeneous (the waves travel at a constant speed), the resonant frequencies, also called normal modes, are harmonics of the lowest fundamental frequency. On the other side, if the cavity has a non-rectilinear shape, like the microwave cavities introduced in the next section, the resonant frequencies may not occur at equally spaced multiples of the fundamental frequency and they may follow a clustered distribution.

This thesis is concerned with cavities having electromagnetic oscillations and in particular, being characterized with a clustered eigenvalue distribution. Namely, the interest is to calculate large amount of eigenfrequencies for superconducting microwave resonators. Hereby, the excited electromagnetic fields inside closed resonators are considered under the assumption of perfectly electric conducting walls. As a result, the main aim of this study coincides with solving the electromagnetic problem for a superconducting cavity, which encloses excited electromagnetic fields. In this direction, detailed numerical approaches for calculation of thousands of eigenfrequencies will be presented in later chapters. Prior to that, some applications will be listed and a brief overview of the numerical techniques will be given.

1.2 Motivation and Objective

The following incomplete list indicates just a few of the applications areas, where the eigenvalue calculations arise, and how diverse they are [68]: acceleration of charged particles, electrical networks, clustering analysis, physics, chemistry, structural dynamics, Markov chain techniques, combustion processes, macro-economics, control theory, to mention just a few. A recent application is the search engine Google, which uses the eigenvector corresponding to the eigenvalue one for an extremely large sparse stochastic matrix [21]. In fact, the Google PageRank algorithm is the largest eigenvalue problem in the world. Additionally, in many applications of electromagnetic fields a large number of precisely calculated eigenfrequencies is also required. The numerical methods for eigenvalue calculation for some cavity structures might fail or result in slow convergence when stable and precise results are required, e.g., Superconducting Proton Linac (SPL) cavities [20]. Here, there are many higher order modes, which can lead to particle beam instabilities [61]. Therefore, in SPL cavities hundreds of highly precise eigenfrequencies are needed for the calculation of the 3D-field distribution and the shunt impedance for the higher order modes. Consequently, this is an important issue for using these cavities in particle accelerators.

Next, a few applications are addressed in which thousands of eigenvalues are used or may be used in the future. A field of application, which has motivated this work and where the necessity for calculation of thousands of eigenfrequencies is emphasized, is the field of quantum chaos. It encompasses the study of the manifestations of classical chaos in the properties of the corresponding quantum or more generally, wave-dynamical system (nuclei, atoms, quantum dots, and electromagnetic or acoustic resonators). Prototypes are billiards of arbitrary shape. In its interior a point-like particle moves freely and is reflected specularly at the

boundaries. Depending on the shape its properties could exhibit chaotic dynamics. Within this thesis, quantum billiards are investigated together with its statistical eigenvalue properties, which reveal the periodic orbits in the quantum spectra and give the quantum chaotic scattering [26]. Specifically, a microwave resonator with chaotic characteristics is simulated, see figure 1.1, and the investigations comprise efficient and robust computation of eigenfrequencies that are needed for its level-spacing analysis [27]. Accordingly, the eigenfrequency level-spacing analysis for the determination of the statistical properties requires many (in order of thousands) eigenfrequencies to be calculated and the accurate determination of the eigenfrequencies has a crucial significance. Moreover, considering that the problem is to compute a large number of eigenfrequencies along with their associated eigenvectors, they can be often located in different ranges, i.e. left-most, right-most, or interior portions of the spectrum could be sought.

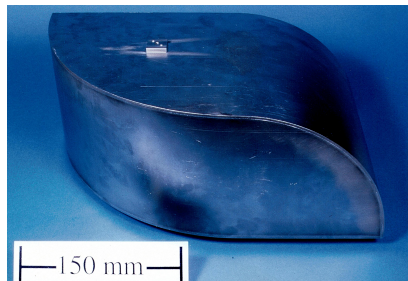


Figure 1.1.: Three-dimensional generalized stadium billiard, consisted of two quarter cylinders with different radii. It is made of niobium, which becomes superconducting at temperatures below 9.2 K. The picture of the billiard cavity was kindly provided by the Institute for Nuclear Physics at the Technical University (TU) of Darmstadt [27, 29, 1].

Another field of research in which thousands of eigenfrequencies have been successfully used is given by the modelling of the properties of graphene with the help of a microwave photonic crystal [16, 17]. Graphene is a monoatomic layer of carbon atoms arranged on a honeycomb lattice and it can be described as one-atom thick layer of the layered mineral graphite [59, 58]. High-quality graphene is very strong, light, nearly transparent, and an excellent conductor of heat and electricity. Its interaction with other materials and light, and its inherently two-dimensional nature produce unique properties. Due to its peculiar electronic properties, the carbon allotrope attracted a lot of attention over the last years, which culminated in a Nobel prize in 2010. Andre Geim and Konstantin Novoselov at the University

of Manchester won the Nobel prize in physics “for groundbreaking experiments regarding the two-dimensional material, graphene”. It is worth mentioning that the band structure of the photonic crystal, which is displayed in figure 1.2, possesses similar properties. The photonic crystal considered in the present work (Dirac billiard cavity) is three-dimensional and composed of rows of metallic cylinders, which are arranged to form the triangular lattice. The purpose of this work is to compare the spectral properties of the superconducting Dirac billiard cavity, which were numerically calculated, with the measurements being conducted from the Institute for Nuclear Physics at the Technical University (TU) of Darmstadt. Herewith, precise statistics for the Dirac billiard cavity can be generated only if thousands of eigenfrequencies have been calculated. As already stated for the billiard cavity, the problem to compute a large number of eigenfrequencies along with their associated eigenvectors can be also interior.

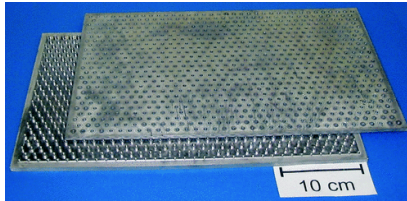


Figure 1.2.: Superconducting microwave Dirac billiard cavity containing 888 metal cylinders. It is constructed from brass and coated with lead. On the figure, the lid is shifted with respect to the billiard body. The picture of the Dirac billiard cavity is copyrighted and property of the Institute for Nuclear Physics at the Technical University of Darmstadt [28].

Summing up, the goals of this work overlap with those of the described application examples from above. Finally, computing a large number of interior eigenvalues remains one of the most difficult problems in computational linear algebra today. Hence, the major challenges posed by this work will be: first, the ability of the numerical approaches to tackle the large-scale eigenvalue problem, second, the capability to extract many, i.e. order of thousands, eigenfrequencies for the considered cavities, and third, the ability to ensure high accuracy as well as robustness of the underlying approaches.

1.3 Adequate Numerical Methods

Reflecting the fact that the analytical solutions of the electromagnetic problems from section 1.2 are not available, the work resorts to the numerical solution using

either the Finite Integration Technique (FIT) [83] or the Finite Element Method (FEM) based on higher order curvilinear elements [7, 6]. In this context, the investigations comprise efficient, robust, and accurate computations of many desired eigenfrequencies in a reasonable time, which also constitute the main aim of the study.

In case that the FIT is used for the solution of the electromagnetic problem, an approach for extraction of resonant frequencies given the output from time-domain computations of closed resonators is covered. The proposed approach uses the advantage that one single time-domain simulation can provide the whole response of an electromagnetic system in a wide frequency band, whereas a frequency-domain formulation naturally concentrates on individual frequency samples and uses one computation for each individual frequency. In addition, due to the fact that the time-domain computations in the field of electromagnetics are already highly developed and considerably more efficient as well as the fact that the transient solver contained in CST Microwave Studio[®] (CST MWS) [2] uses a high degree of parallelization provided with the modern Graphics Processing Units (GPUs) feature, the simulation can be dramatically accelerated. Therefore, the time-domain responses for a wide frequency band can be easily and quickly obtained. In this way, a significant reduction in computational time can be achieved and therefore, a high interest within this thesis leads to the time-domain computations for electromagnetic problems.

Additionally, the FIT, introduced in [83], can be also used for solving the electromagnetic problem in Frequency Domain (FD), ending up with a standard large-scale eigenvalue problem for a real symmetric matrix \mathbf{A} , such that

$$\mathbf{A} \vec{x}_k = \lambda_k \vec{x}_k. \quad (1.1)$$

On another side, if the FEM is used for the electromagnetic solution, the outcome is an algebraic generalized eigenvalue problem for given real symmetric sparse matrix pencils \mathbf{A} and \mathbf{B} , derived from the Maxwell's equations for a loss-free and source-free bounded domain with perfectly electric conducting walls on its surface. Hereby, the numerical solution of the generalized large-scale eigenvalue problem for the matrix pair (\mathbf{A}, \mathbf{B}) is considered. It is the task of finding the real scalars λ_k and the corresponding real-valued vectors $\vec{x}_k \neq 0$ such that

$$\mathbf{A} \vec{x}_k = \lambda_k \mathbf{B} \vec{x}_k, \quad (1.2)$$

where $\mathbf{A} \in \mathbb{R}^{n \times n}$ and $\mathbf{B} \in \mathbb{R}^{n \times n}$ are symmetric matrices, \mathbf{B} is positive definite matrix, $k = 1, 2, \dots, n$, and n is several thousands. The scalars λ_k are called the generalized

eigenvalues and the vectors \vec{x}_k are the generalized eigenvectors. Typically, the FIT and the FEM matrices are diagonally dominant and sparse. That is, they have very few nonzero entries, as it will be explained in chapter 2 of this thesis. In conclusion, both cases result in solving one of the fundamental problems, the large-scale eigenvalue problem and later in the text, the entire process for eigenvalue determination in FD is referred to as frequency-domain approach.

Various types of numerical methods for eigenvalue determination exist, such as Jacobi-Davidson [72], Arnoldi [8], Lanczos [42, 41], Krylov-Schur [74], and so on. Some of the above mentioned methods are available in different software packages: CST [2], Computational Electromagnetics 3D (CEM3D) [7], Matlab [3], Pysparse library [32], Scalable Library for Eigenvalue Problem Computations (SLEPc) [35], PReconditioned Iterative MultiMethod Eigensolver (PRIMME) library [73], Trilinos [9], along with others. Despite the fact that many algorithms for eigenvalue determination exist, accompanied by the numerical models that are becoming increasingly more sophisticated, not as many are specifically adapted for computing a large number of eigen pairs. They can usually calculate limited number of extreme or interior eigenfrequencies, and relatively few are designed for effectively reusing a large number of good initial presumptions, when they are available. Thus, an additional challenge from these applications is that the dimension of the desired eigen subspace is large, namely, one might possibly need thousands of eigen pairs located in a specified range, also referred to as a 'window', of matrices with dimension in excess of several millions. Along the project requirements, the numerical methods for eigenvalue determination might result in an extremely time consuming simulation, along with slow convergence and huge storage as well as memory requirements.

The Lanczos algorithm with its variations is very attractive for the project necessities. Some variations of the Lanczos method are: the implicitly restarted Lanczos method [23], which is implemented in Arnoldi Package (ARPACK) [44], restarted Lanczos bidiagonalization [40], thick-restart Lanczos method [39], and so on. The major practical advantage of the Lanczos method is the tridiagonal reduction of the eigenvalue problem that yields minimal storage requirements, as do the associated algorithms for its eigenvalue and eigenvector computations. Also, the required arithmetic operations are small, allowing work with very large tridiagonal matrices and therefore, with very large real symmetric matrices. Furthermore, the Lanczos method takes a significant advantage over its competitors, which concentrate on individual frequency samples per iteration. Concluding, based on the project requirements the investigations comprise efficient, robust, and accurate computations of many desired eigenfrequencies by employing a proper numerical solution

of the electromagnetic problem and an efficient implementation of the Lanczos method to solve the large-scale eigenvalue problem.

1.4 Outline of the Thesis

The thesis is structured as follows. The fundamental concepts of classical electrodynamics, which are needed for the following chapters will be briefly presented in chapter 2. The chapter focuses on the Maxwell's equations describing the continuous electrodynamics as well as their discretization by the FIT and the FEM.

In the following chapter, a fast approach for an accurate eigenfrequency extraction, taken into consideration the evaluated electric field computations in time domain of a superconducting resonant structure will be addressed. Consequently, in chapter 3 all the steps that constitute the eigenvalue extraction from time-domain computations will be described. Additionally, the theory of interest for this method is also explained in this chapter.

In chapter 4, another promising approach for high precision eigenfrequency determination will be reviewed. It is based either on a finite element or finite integration formulation of an electromagnetic problem for a superconducting cavity and the Lanczos method for the eigenvalue determination itself. Here, the basic Lanczos algorithm for the standard eigenvalue problem will be described, followed by a description of the B-Lanczos algorithm and its variations, which will be used to solve the generalized eigenvalue formulation. Further contribution of this work includes the presentation of the Lanczos method with polynomial filtering.

Chapter 5 summarizes the implementation details for the methods presented in chapter 3 and 4.

Chapter 6 investigates the simulation scenarios for the billiard and Dirac billiard cavity together with the obtained numerical results. Here, it will be demonstrated that the proposed approaches are able to extract many eigenfrequencies of a closed resonator in a relatively short time. In addition to the need to ensure a high precision of the calculated eigenfrequencies as well as to verify and validate the results, comparisons with reference numerical FEM simulations and measurements will be given. Furthermore, the high accuracy of the techniques and the good agreement with the reference data will be reviewed in this chapter. At the end, it will be shown that the suggested techniques can be used for precise extraction of many eigenfrequencies.

Finally, a summary in chapter 7 recapitulates the main results of this work as well as it provides a short outlook to further studies.



2 Electrodynamics

In this chapter, a few aspects of the classical electrodynamics are summarized in order to introduce the underlying concepts, which are needed for the successive chapters. Starting with the Maxwell's equations, the constitutive equations that are required for their solution as well as the boundary conditions are introduced and the resulting wave equations are derived in section 2.1. Apart from limited number of special cases, the Maxwell's equations have no analytical solution. Nevertheless, an approximate numerical solution of the discretized Maxwell's equations can be found. Therefore they are discretized by approximating the continuous space through discrete, finite-dimensional spaces and by introducing discrete instants in time. Afterward, the approximate solutions are found using the numerical methods. From the numerous discretization techniques that exist to discretize integral or differential equations, the Finite Integration Technique (FIT) and the Finite Element Method (FEM) are introduced in section 2.3 and 2.4, respectively. At the beginning of each section, the principles of the applied numerical methods are reviewed, followed by the derivation of the resulting discrete (generalized) eigenvalue formulation.

2.1 Continuous Electrodynamics

2.1.1 The Maxwell's Equations

The modern society relies on electromagnetic devices, e.g. computers, television, radio, internet, microwave ovens, mobile telephones, radar and medical devices, electrical motors, electrical power networks, and many more. Each of these examples is used in a broad range of situations and doubtless, the electromagnetic phenomena have a profound impact on the present society.

The understanding of the electromagnetic phenomena is treated by the electromagnetic field theory, which describes the interactions between the electric charges by the Maxwell's equations. Although many famous scientists in the 18th and 19th century partly contributed to the Maxwell's equations, they are named after the Scottish physicist and mathematician James Clerk Maxwell (1831-1879), who first published the full form of the Maxwell's equations in [51]. Analytical solutions in closed form are known for only a very limited number of special cases, which

hardly ever are directly applicable to real-world applications [85]. Instead, more or less crude approximations have been employed in various attempts to bridge the gap between the theory and the advanced applications. Nowadays, it is possible to find an approximate numerical solution of the discretized Maxwell's equations.

The continuous Maxwell's equations [55, 80] are expressed in terms of the electric field strength indicated by \vec{E} , the electric flux density \vec{D} , the magnetic field strength \vec{H} , the magnetic flux density denoted by \vec{B} , the electric current density \vec{J} , and the electric charge density ρ . The spatial variable is denoted by \vec{r} and the time dependency by t . The integral form of the Maxwell's equations reads

$$\oint_{\partial A} \vec{E}(\vec{r}, t) \cdot d\vec{s} = - \int_A \frac{\partial}{\partial t} \vec{B}(\vec{r}, t) \cdot d\vec{A} \quad (2.1a)$$

$$\oint_{\partial A} \vec{H}(\vec{r}, t) \cdot d\vec{s} = \int_A \left(\frac{\partial}{\partial t} \vec{D}(\vec{r}, t) + \vec{J}(\vec{r}, t) \right) \cdot d\vec{A} \quad (2.1b)$$

$$\oint_{\partial V} \vec{D}(\vec{r}, t) \cdot d\vec{A} = \int_V \rho(\vec{r}, t) dV \quad (2.1c)$$

$$\oint_{\partial V} \vec{B}(\vec{r}, t) \cdot d\vec{A} = 0 \quad (2.1d)$$

for any surface A and volume V . The equation (2.1a) is called Faraday's law, whereas with (2.1b) is given the Ampère's law. These two equations connect the time derivative of the magnetic flux density or the time derivative of the electric flux density and the electric current density over a surface A with the closed line integral of the field vector along its boundary ∂A . The remaining equations, (2.1c) and (2.1d), are known as Gauss' law and Gauss' law of magnetism (or non-existence of magnetic charges), respectively. They relate the total amount of charges within an arbitrary volume V to the surface integrals of the flux quantities over the closed surface ∂V of the volume V .

By applying the Kelvin-Stokes' theorem [18] to the Ampère's and the Faraday's law and the Gauss-Ostrogradsky's theorem to the Gauss' laws, the Maxwell's equations can be expressed equivalently in their differential form. Using the Stokes' theorem

$$\oint_{\partial A} \vec{E}(\vec{r}, t) \cdot d\vec{s} = \int_A (\nabla \times \vec{E}(\vec{r}, t)) \cdot d\vec{A} \quad (2.2)$$

and the Gauss' theorem

$$\oint_{\partial V} \vec{B}(\vec{r}, t) \cdot d\vec{A} = \int_V (\nabla \cdot \vec{B}(\vec{r}, t)) dV, \quad (2.3)$$

as applied to \vec{E} and \vec{B} , the corresponding differential form of the Maxwell's equations (2.1a)-(2.1d) is given with

$$\nabla \times \vec{E}(\vec{r}, t) = -\frac{\partial}{\partial t} \vec{B}(\vec{r}, t) \quad (2.4a)$$

$$\nabla \times \vec{H}(\vec{r}, t) = \frac{\partial}{\partial t} \vec{D}(\vec{r}, t) + \vec{J}(\vec{r}, t) \quad (2.4b)$$

$$\nabla \cdot \vec{D}(\vec{r}, t) = \rho(\vec{r}, t) \quad (2.4c)$$

$$\nabla \cdot \vec{B}(\vec{r}, t) = 0. \quad (2.4d)$$

The electric current density \vec{J} in (2.1b) and (2.4b) may consist of three parts: a conductive part \vec{J}_c , a convective part \vec{J}_{cv} , and an impressed current density \vec{J}_i

$$\vec{J}(\vec{r}, t) = \vec{J}_c(\vec{r}, t) + \vec{J}_{cv}(\vec{r}, t) + \vec{J}_i(\vec{r}, t). \quad (2.5)$$

As already stated in the introductory words of the thesis, the electric current density \vec{J} will not be considered within this work as the interest is in loss-free problems with no additional sources of an electromagnetic field.

2.1.2 Material Equations

The Maxwell's equations (2.4a)-(2.4d) form a coupled set of first-order linear partial differential equations that relate sources (charges and currents) to the electromagnetic fields and fluxes. Subsequently, each equation cannot be solved individually and here, the constitutive equations enable their solution [80]. For a macroscopic media the dynamical response of the aggregates of atoms is summarized in the constitutive equations

$$\vec{D}(\vec{r}, t) = \epsilon_0 \vec{E}(\vec{r}, t) + \vec{P}(\vec{E}, \vec{r}, t) \quad (2.6a)$$

$$\vec{B}(\vec{r}, t) = \mu_0 \vec{H}(\vec{r}, t) + \mu_0 \vec{M}(\vec{H}, \vec{r}, t) \quad (2.6b)$$

$$\vec{J}(\vec{r}, t) = \sigma(\vec{r}) \vec{E}(\vec{r}, t), \quad (2.6c)$$

where the material constant ε_0 is the free-space electric permittivity, the μ_0 indicates the magnetic permeability of vacuum, and the $\vec{P}(\vec{E}, \vec{r}, t)$ and $\vec{M}(\vec{H}, \vec{r}, t)$ denote the electric and magnetic dipole moment density, respectively. The constitutive equations consider the electromagnetic properties of the medium in which the fields exist and connect the vectors \vec{D} and \vec{J} with \vec{E} , and \vec{H} with \vec{B} . While the first terms in (2.6a) and (2.6b) describe the linear contributions of the field, \vec{P} and \vec{M} describe the macroscopic behavior of the physical effects inside the materials. In general, they are time-variant, frequency dependent, and non-linear as well as non-isotropic functions of \vec{E} and \vec{H} , respectively.

Due to the fact that this thesis is concerned with the eigenvalue calculations for resonators, whose walls have an infinite conductivity and are filled with a lossless material, for arbitrary time dependence the considerations are restricted to linear, frequency-independent, isotropic, and non-dispersive materials, such that

$$\vec{D}(\vec{r}, t) = \varepsilon \vec{E}(\vec{r}, t) = \varepsilon_0 \varepsilon_r \vec{E}(\vec{r}, t) \quad \text{with } \varepsilon_0 = 8.854 \cdot 10^{-12} \frac{\text{As}}{\text{Vm}} \quad (2.7a)$$

$$\vec{B}(\vec{r}, t) = \mu \vec{H}(\vec{r}, t) = \mu_0 \mu_r \vec{H}(\vec{r}, t) \quad \text{with } \mu_0 = 4\pi \cdot 10^{-7} \frac{\text{Vs}}{\text{Am}}, \quad (2.7b)$$

where ε , ε_r , μ , and μ_r are real-valued time-invariant quantities. Here, the ε_r and μ_r are the relative permittivity and permeability of the material.

2.1.3 Boundary Conditions

With the aim of finding proper solutions of the Maxwell's equations, the behavior of the electromagnetic field should be known at the boundary interface that is shared from medium 1 and 2. Accordingly, on one hand, it is assumed that the first medium is characterized by ε_1 , μ_1 , and σ_1 , and on the other hand the medium 2 has different properties given with ε_2 , μ_2 , and σ_2 . At the interface, the tangential and the normal fields must satisfy so-called boundary conditions, which are the consequences of the Maxwell's equations.

Applying the Faraday's and the Ampère's law on a surface, which intersects the material interface, will result in the following conditions for the electric and the magnetic field strengths

$$\vec{n} \times (\vec{E}_2 - \vec{E}_1) = 0 \quad (2.8a)$$

$$\vec{n} \times (\vec{H}_2 - \vec{H}_1) = \vec{J}_s, \quad (2.8b)$$

where \vec{J}_s is the surface current density and \vec{n} is the unit vector normal to the boundary and pointing into medium 2. The equation (2.8a) simply states that the tangential electric field components must be continuous across the boundary, whereas the equation (2.8b) shows that the tangential components of the magnetic field strength are continuous only if the surface current density is zero on the interface.

Analogously, the application of the Gauss' laws on a closed volume containing the both materials leads to the following conditions for the electric and magnetic flux densities

$$\vec{n} \cdot (\vec{D}_2 - \vec{D}_1) = \rho_s \quad (2.9a)$$

$$\vec{n} \cdot (\vec{B}_2 - \vec{B}_1) = 0, \quad (2.9b)$$

with ρ_s being the surface charge density. The above equations state that the normal component of the magnetic flux density is always continuous at the interface of two media with different properties, while the normal component of the electric flux density is discontinuous in case that surface charges are present at the interface.

2.1.4 Wave Equation

Combining the first two Maxwell's equations in differential form (2.4a)-(2.4b) and supplementing them by the linear isotropic material equations with time-independent material parameters (2.7a)-(2.7b), the second-order forms of the Maxwell's equations in terms of the electric and the magnetic field strength can be deduced

$$\nabla \times (\nabla \times \vec{E}(\vec{r}, t)) + \mu \varepsilon \frac{\partial^2}{\partial t^2} \vec{E}(\vec{r}, t) = -\mu \frac{\partial}{\partial t} \vec{J}(\vec{r}, t) \quad (2.10a)$$

$$\nabla \times (\nabla \times \vec{H}(\vec{r}, t)) + \mu \varepsilon \frac{\partial^2}{\partial t^2} \vec{H}(\vec{r}, t) = \nabla \times \vec{J}(\vec{r}, t). \quad (2.10b)$$

As already mentioned above, in this thesis it is assumed that the waves propagate far enough from sources, such that $\vec{J} = 0$ and $\rho = 0$. Consequently, the previous equation can be transformed into

$$\nabla \times (\nabla \times \vec{E}(\vec{r}, t)) + \mu \varepsilon \frac{\partial^2}{\partial t^2} \vec{E}(\vec{r}, t) = 0 \quad (2.11a)$$

$$\nabla \times (\nabla \times \vec{H}(\vec{r}, t)) + \mu \varepsilon \frac{\partial^2}{\partial t^2} \vec{H}(\vec{r}, t) = 0. \quad (2.11b)$$

Using the property of the double-cross product and the Gauss' laws for homogeneous media, the following equations can be obtained

$$\begin{aligned}\nabla \times (\nabla \times \vec{E}(\vec{r}, t)) &= \nabla (\nabla \cdot \vec{E}(\vec{r}, t)) - \Delta \vec{E}(\vec{r}, t) \\ &= \frac{1}{\varepsilon} \nabla \rho - \Delta \vec{E}(\vec{r}, t) = -\Delta \vec{E}(\vec{r}, t)\end{aligned}\quad (2.12a)$$

$$\nabla \times (\nabla \times \vec{H}(\vec{r}, t)) = \nabla (\nabla \cdot \vec{H}(\vec{r}, t)) - \Delta \vec{H}(\vec{r}, t) = -\Delta \vec{H}(\vec{r}, t). \quad (2.12b)$$

Wherefore, (2.11a) and (2.11b) transform to

$$\Delta \vec{E}(\vec{r}, t) - \mu\varepsilon \frac{\partial^2}{\partial t^2} \vec{E}(\vec{r}, t) = 0 \quad (2.13a)$$

$$\Delta \vec{H}(\vec{r}, t) - \mu\varepsilon \frac{\partial^2}{\partial t^2} \vec{H}(\vec{r}, t) = 0, \quad (2.13b)$$

which are called homogeneous wave equations with no losses in terms of the electric or the magnetic field strength.

2.2 Discrete Electrodynamics

The first step in the process of obtaining discrete solutions to the Maxwell's equations is to set up a computational grid in the domain of interest. Therefore, the complete domain of interest $\Omega \subset (\mathbb{R}^1, \mathbb{R}^2, \mathbb{R}^3)$ in the continuous space is mapped to a finite set of discrete elements, which depend on the dimensionality of Ω and do not overlap. In this way, a set of spatial elements is defined, which is a topological structure in space and is referred to as a computational grid G . For practical reasons, typically basic geometrical shapes like triangles or rectangles in a Two Dimensional (2D) domain and tetrahedrons or hexahedra in a Three Dimensional (3D) domain are used, cf. figure 2.1.

The resulting discrete equations are solved with the help of numerical methods. Namely, the powerful computers have enabled the ability to solve the Maxwell's equations using computational methods that allow solution for large classes of problems without broad modifications of the computer programs. The part of the electromagnetics that deals with the computational methods is known as Computational Electromagnetics (CEM). Although the CEM is a young discipline, it has developed into a main design tool with the aim to find numerical approximations to the continuous Maxwell's equations. The most frequently used algorithms in the CEM are the Finite Integration Technique (FIT), the Finite Differences (FD), the Finite Element Method (FEM), and the Boundary Element Method (BEM), which is

usually referred to as Method of Moments (MoM). From the numerous techniques that are known for discretizing the Maxwell's equations, the FIT and the FEM will be introduced in the sections 2.3 and 2.4, respectively.

2.3 Finite Integration Technique

The Finite Integration Technique (FIT) is a spatial discretization scheme to numerically solve electromagnetic field problems in Time Domain (TD) and in Frequency Domain (FD). The technique was proposed by Thomas Weiland [83, 84] in 1977. It provides a discrete reformulation of the Maxwell's equations in their integral form, which guarantees the physical properties of the computed fields and leads to an unique solution. The FIT can be also viewed as a generalization of the Finite-Difference Time-Domain Method (FDTD). At the beginning, the FIT was utilized for the numerical calculation of the resonance frequencies in FD. Afterward, the range of applications was continuously expanded over the years. Currently, this technique allows a simulation of real-world electromagnetic field problems with complex geometries and therefore, covers wide range of applications, e.g. electro- and magnetostatics, stationary current problems as well as low- and high-frequency problems.

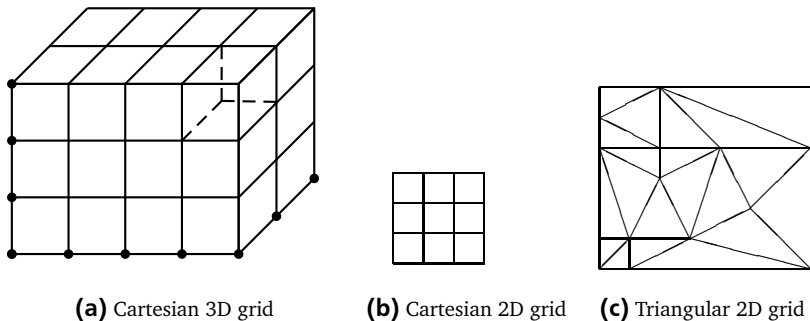


Figure 2.1.: (a) Cartesian 3D grid used for discretizing a structure with $4 \times 3 \times 2$ hexahedral mesh elements. (b) Cartesian 2D equidistant grid. (c) Triangular 2D grid.

2.3.1 Spatial Discretization by Computational Grids

Within this thesis, the analyzed resonators are discretized with a hexahedral computational grid. An example of a hexahedral computational grid for a brick-shaped geometry is illustrated in figure 2.1a. However, it should be noted that the FIT is not restricted to three-dimensional Cartesian meshes, but it also allows to consider all types of coordinate meshes [76, 70, 82].

In the three-dimensional domains \mathbb{R}^3 , the discrete elementary volumes V_n with $n = 1, \dots, N_V$, also called mesh cells, are bounded by several mesh facets A_n (where $n = 1, \dots, N_A$) each bounded with four mesh edges L_n (where $n = 1, \dots, N_L$) and four mesh points $P_n(i, j, k)$ (where $n = 1, \dots, N_P$). The grid points $P(i, j, k) = (x_i, y_j, z_k)$ are indexed in the following way

$$\begin{aligned} x_1 &< x_2 < \dots < x_i < \dots < x_{N_x} \\ y_1 &< y_2 < \dots < y_j < \dots < y_{N_y} \\ z_1 &< z_2 < \dots < z_k < \dots < z_{N_z}, \end{aligned} \tag{2.14}$$

where N_x , N_y , and N_z represent the number of points in each coordinate direction, and i , j , k are the corresponding indices. The mesh facets and the mesh edges are oriented entities, with arbitrary user-defined orientation, while the volumes and the nodes are not oriented [81, 82]. Moreover, all mesh entities of the same kind are numbered sequentially. Except the favored orientation and the numbering techniques, which make the algorithms more efficient, there is no principal restriction on how the entries are oriented or numbered. The edge between the points $P(i, j, k)$ and $P(i + 1, j, k)$ is denoted with $L_x(i, j, k)$. Accordingly, the electric voltage along the mesh edge $L_x(i, j, k)$ is indicated with $\widehat{e}_x(i, j, k)$. Similar, the voltage between the points $P(i, j, k)$ and $P(i, j + 1, k)$ is denoted with $\widehat{e}_y(i, j, k)$ as well as the voltage between $P(i, j, k)$ and $P(i, j, k + 1)$ as $\widehat{e}_z(i, j, k)$ (see figure 2.2). The face in y -direction with the points $P(i, j, k)$, $P(i + 1, j, k)$, $P(i + 1, j, k + 1)$, and $P(i, j, k + 1)$ is named as $A_y(i, j, k)$, and the appropriate flux as $\widehat{b}_y(i, j, k)$.

For the discretization of the integral form of the Maxwell's equations the FIT uses a primary grid G and a dual grid \widetilde{G} . Analogous to the primary grid G , the dual grid \widetilde{G} contains: dual mesh cells \widetilde{V}_n with $n = 1, \dots, N_{\widetilde{V}}$, bounded by several mesh facets \widetilde{A}_n (where $n = 1, \dots, N_{\widetilde{A}}$) each bounded with four mesh edges \widetilde{L}_n (where $n = 1, \dots, N_{\widetilde{L}}$) and four mesh points $\widetilde{P}_n(i, j, k)$ (where $n = 1, \dots, N_{\widetilde{P}}$). In the following all of the marks for the dual grid will be represented with tilde.

The dual grid is constructed according to the following duality conditions: the grid points \widetilde{P} of the dual grid \widetilde{G} are co-located with the centers of the primary grid cells. Figures 2.3a and 2.3b show the primary grid relative to its dual. Namely,

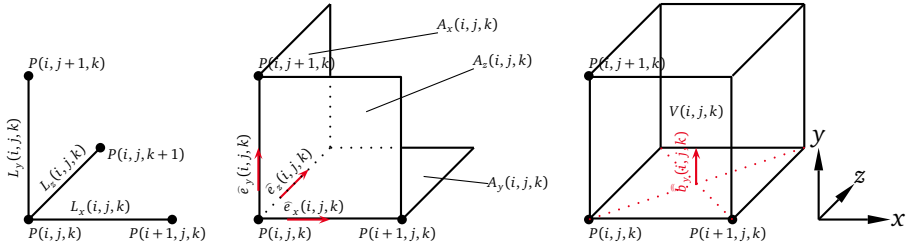


Figure 2.2.: Indexing of the edges and the faces. Each edge and face has the same index in x -, y -, and z -direction as well as the same starting node (point).

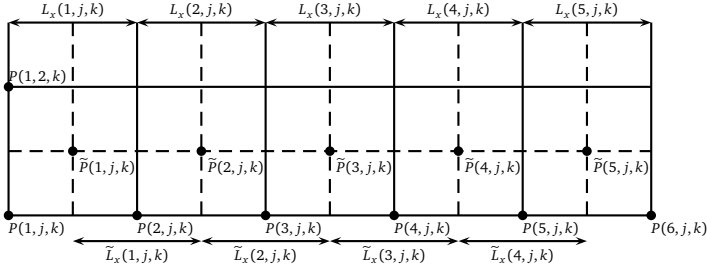
each dual (primary) cell contains exactly one primary (dual) point. All of the grid elements of the dual and the primary grid have the same index. The orientation of a dual (primary) edge coincides with the orientation of the primary (dual) surface. Furthermore, every primary surface is cut by exactly one dual edge and every primary edge is cut exactly by one dual surface (cf. figure 2.3b). In principal, the respective cutting angles can be arbitrary. If they are 90° , the orthogonality condition is met. Given an arbitrary primary grid G , the construction of a dual grid \tilde{G} that fulfills all of the conditions is generally possible and the grids are then referred to as dual orthogonal. Throughout this thesis, a homogeneous material is assumed in every resulting elementary volume.

When using the FIT, the closed line and the surface integrals in the continuous Maxwell's equations are splitted into integrals along the grid edges and over the grid surfaces, respectively. The Faraday's and the Gauss' law of magnetism use the primary (electric) grid, while the Ampère's and the Gauss' law exploit the dual (magnetic) grid [78]. As a result, the discrete equations are exact representations of the continuous Maxwell's equations. However, the approximations will be introduced by the discretization of the material relations (2.6a)-(2.6c), as will be explained in section 2.3.4. At that point, the necessary coupling between the primary and the dual grid is also accomplished.

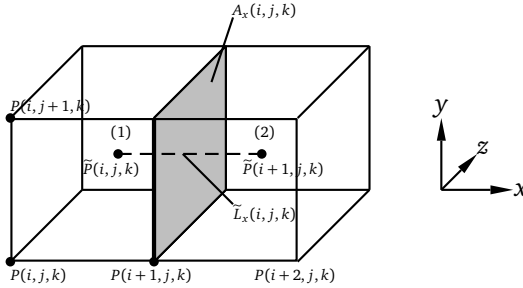
2.3.2 The Maxwell's Grid Equations

Discretization of the Faraday's law

In order to transfer the Faraday's law in integral form (2.1a) to the grid space, the FIT uses the electric grid G [81, 82]. The loop integral on its left hand side is carried out along the edges. Integrating the continuous electric field \vec{E} along



(a) Cartesian primary and dual 2D grid



(b) Cartesian primary and dual 3D grid

Figure 2.3.: Depiction of the primary grid G relative to the dual grid \tilde{G} . (a) An example of a Cartesian primary and dual 2D grid. The grid points \tilde{P} of the dual grid \tilde{G} are co-located with the centers of the primary grid cells. Namely, each dual (primary) cell contains exactly one primary (dual) point. All of the grid elements of the dual and the primary grid have the same index. (b) An example of a Cartesian primary and dual 3D grid. Every primary surface is cut by exactly one dual edge and every primary edge is cut exactly by one dual surface.

an edge $L_p(i, j, k)$ with $p \in \{x, y, z\}$ yields a discrete electric voltage denoted by $\hat{e}_p(i, j, k)$, where $p \in \{x, y, z\}$. The electric grid voltage $\hat{e}_p(i, j, k)$ is given with

$$\hat{e}_p(i, j, k) = \int_{L_p(i,j,k)} \vec{E} \cdot d\vec{s}. \quad (2.15)$$

Summing up the discrete electric voltages along all edges enclosing a cell face leads to an exact discrete representation of the continuous closed loop integral. At

the same time, integrating the continuous magnetic flux density \vec{B} over a surface $A_p(i, j, k)$ yields the discrete magnetic integral flux $\widehat{\vec{b}}_p(i, j, k)$

$$\widehat{\vec{b}}_p(i, j, k) = \int_{A_p(i, j, k)} \vec{B} \cdot d\vec{A}. \quad (2.16)$$

According to figure 2.4a, it can be noticed that the discrete electric voltages of directly neighboring cells can be mutually canceled. Therefore, it is satisfactory that only one mesh cell is considered, e.g. the cell displayed in figure 2.4b. From here, it holds

$$\widehat{e}_x(i, j, k) + \widehat{e}_y(i+1, j, k) - \widehat{e}_x(i, j+1, k) - \widehat{e}_y(i, j, k) = -\frac{d}{dt} \widehat{\vec{b}}_z(i, j, k). \quad (2.17)$$

As a result, if the Faraday's law holds for one elementary facet, it holds for all faces

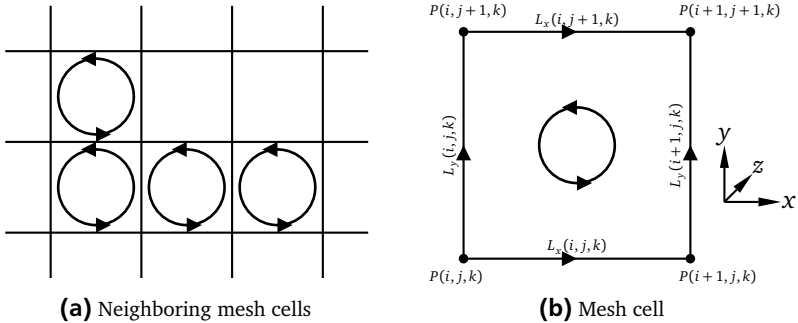


Figure 2.4.: Integration path for the derivation of the first Maxwell's grid equation.

too. Applying the derivative in time, the discrete Faraday's law can be obtained in the following form

$$\mathbf{C} \widehat{\mathbf{e}} = -\frac{d}{dt} \widehat{\mathbf{b}}, \quad (2.18)$$

where all the electric voltages are grouped in the vector $\widehat{\mathbf{e}}$ and all the magnetic fluxes for the faces of the computational grid G are grouped in the vector $\widehat{\mathbf{b}}$. As already mentioned, this is an exact representation of the Faraday's law. It should be noted that when passing from (2.1a) to (2.18) on a given discretization mesh, no approximations are made and therefore, no discretization error is introduced. The matrix \mathbf{C} is sparse and singular and as apparent from equation (2.17), each

row has two entries 1 and two -1 . It is, thus, a topological matrix that plays the role of the curl operator in the discrete equations

$$\mathbf{C} = \begin{pmatrix} 0 & \begin{array}{c} \diagdown +1 \\ \diagup -1 \end{array} & \begin{array}{c} \diagdown -1 \\ \diagup +1 \end{array} \\ \begin{array}{c} \diagdown -1 \\ \diagup +1 \end{array} & 0 & \begin{array}{c} \diagdown -1 \\ \diagup +1 \end{array} \\ \begin{array}{c} \diagdown +1 \\ \diagup -1 \end{array} & \begin{array}{c} \diagdown -1 \\ \diagup +1 \end{array} & 0 \end{pmatrix}. \quad (2.19)$$

The matrix \mathbf{C} is the incidence matrix of edges to faces, i.e. it describes in a topological manner which edges belong to each face. It has a number of rows equal to the number of faces N_A , and a number of columns equal to the number of edges N_L in the primary mesh. An element of this matrix is equal to 1 if a given edge belongs to a given face and their orientations match, it is equal to -1 if the edge belongs to the face but their orientations are opposite, and it is equal to 0 if the edge does not belong to the given face.

Discretization of the Gauss' law of magnetism

For the discretization of the Gauss' law of magnetism the FIT uses the electric grid G . Assuming that the surface integral of the magnetic flux density over a mesh cell in the Gauss' law of magnetism is splitted in surface integrals over the cell-surfaces, the discrete Gauss' law of magnetism can be derived. At this point, it should be pointed out that the discrete magnetic flux densities of directly neighboring cells can be mutually eliminated. According to the above, only one cell is adequate to be considered, as shown in figure 2.5a. The surface integrals over this cell give

$$\begin{aligned} \widehat{\widehat{b}}_x(i, j, k) - \widehat{\widehat{b}}_x(i + 1, j, k) + \widehat{\widehat{b}}_y(i, j, k) - \widehat{\widehat{b}}_y(i, j + 1, k) \\ + \widehat{\widehat{b}}_z(i, j, k) - \widehat{\widehat{b}}_z(i, j, k + 1) = 0. \end{aligned} \quad (2.20)$$

The resulting equation for the discrete Gauss' law of magnetism has the form

$$\mathbf{s} \widehat{\widehat{\mathbf{b}}} = 0, \quad (2.21)$$

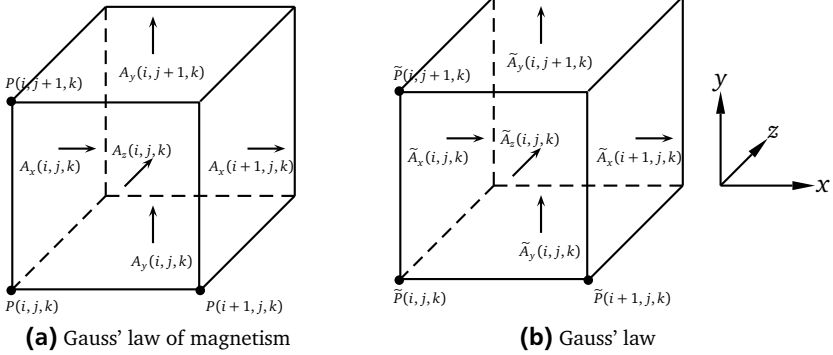


Figure 2.5.: (a) Primary mesh cell for the discretization of the Gauss' law of magnetism. (b) Dual mesh cell for the discretization of the Gauss' law.

where \mathbf{S} is a sparse topological matrix or in other words, the discrete equivalent of the divergence operator, as shown below

$$\mathbf{S} = \left(\begin{array}{c} \begin{array}{c} \diagup \quad \diagdown \\ -1 \quad +1 \end{array} \quad \begin{array}{c} \diagdown \quad \diagup \\ -1 \quad +1 \end{array} \quad \begin{array}{c} \diagup \quad \diagdown \\ -1 \quad +1 \end{array} \end{array} \right). \quad (2.22)$$

The matrix \mathbf{S} as an incidence matrix of faces to volumes describes in a topological manner which faces belong to each volume and what is their relative orientation. The matrix \mathbf{S} has a number of rows equal to the number of volumes N_V and a number of columns equal to the the number of faces N_A in the primary mesh. An element of this matrix is equal to 1 if a given face belongs to the given volume and their orientations match, it is equal to -1 if the face belongs to the volume but their orientations are opposite, and it is equal to 0 if the face does not belong to the given volume.

Discretization of the Ampère's law and the Gauss' law

In order to accomplish the discretization of the Ampère's and the Gauss' law the FIT uses the magnetic grid $\tilde{\mathcal{G}}$. Hence, the magnetic voltages $\tilde{h}_p(i, j, k)$ and the electric flux densities $\tilde{d}_p(i, j, k)$ with $p \in \{x, y, z\}$ are mapped to the grid edges $\tilde{L}_p(i, j, k)$ and the grid surfaces $\tilde{A}_p(i, j, k)$, respectively (see figure 2.5b).

Summing up, the Maxwell's grid equations for loss-free problems with no additional sources of an electromagnetic field read

$$\nabla \times \vec{E} = -\frac{\partial}{\partial t} \vec{B} \quad \longrightarrow \quad \mathbf{C} \hat{\mathbf{e}} = -\frac{d}{dt} \hat{\mathbf{b}} \quad (2.23a)$$

$$\nabla \times \vec{H} = \frac{\partial}{\partial t} \vec{D} \quad \longrightarrow \quad \tilde{\mathbf{C}} \hat{\mathbf{h}} = \frac{d}{dt} \hat{\mathbf{d}} \quad (2.23b)$$

$$\nabla \cdot \vec{D} = 0 \quad \longrightarrow \quad \tilde{\mathbf{S}} \hat{\mathbf{d}} = 0 \quad (2.23c)$$

$$\nabla \cdot \vec{B} = 0 \quad \longrightarrow \quad \mathbf{S} \hat{\mathbf{b}} = 0, \quad (2.23d)$$

where the incidence matrices $\tilde{\mathbf{S}}$ and $\tilde{\mathbf{C}}$ are the discrete equivalents of the divergence and the curl operators corresponding to the dual grid \tilde{G} .

2.3.3 Properties of the Matrices

The solutions of the continuous Maxwell's equations obey the following vector relation

$$\nabla \cdot (\nabla \times \vec{E}) = 0. \quad (2.24)$$

In [81, 79] it is aimed to derive that a discrete analogue of this equation exists and it holds for both the primary and the dual grid. Namely, it can be shown that the product of the discrete divergence operator by the discrete curl operator is identical zero for the both grids

$$\mathbf{S} \mathbf{C} = 0 \quad (2.25a)$$

$$\tilde{\mathbf{S}} \tilde{\mathbf{C}} = 0. \quad (2.25b)$$

This is a very important property, which mimics in the discrete setup the continuous relation (2.24). Lastly, the duality condition of G and \tilde{G} can be expressed with respect to the matrices \mathbf{C} and $\tilde{\mathbf{C}}$ by

$$\tilde{\mathbf{C}} = \mathbf{C}^T. \quad (2.26)$$

2.3.4 Material Discretization

Until now, the Maxwell's equations are discretized with no errors within the FIT. The discretization error will occur in the discretization of the material relations

(2.6a)-(2.6c). On the one hand, the electric voltage \widehat{e} and the magnetic flux quantity \widehat{b} have to be connected with the electric flux density \widehat{d} and the magnetic field strength \widehat{h} , respectively. On the other hand, a suitable averaging has to be assumed for the generally discontinuous and location-dependent material properties at the intersection points of the edges and the surfaces of the both grids.

The calculation is accomplished in a two-step procedure, which uses the example of the relation between \widehat{h} and \widehat{b} for the case when two primary cells are intersected by one dual edge \widetilde{L}_x (see figure 2.3b). The line integral of \vec{H} along the edge $\widetilde{L}_x(i, j, k)$ can be divided into two parts corresponding to the primary cells

$$\begin{aligned} \widehat{h}_x(i, j, k) &= \int_{\widetilde{L}_x(i, j, k)} \vec{H} \cdot d\vec{s} = \int_{\widetilde{L}_x(i, j, k)^{(1)}} B_x / \mu_1 dx + \int_{\widetilde{L}_x(i, j, k)^{(2)}} B_x / \mu_2 dx \\ &\approx B_x \left(\widetilde{L}_x(i, j, k)^{(1)} / \mu_1 + \widetilde{L}_x(i, j, k)^{(2)} / \mu_2 \right) \\ &= B_x \overline{\mu^{-1}}(i, j, k) \widetilde{L}_x(i, j, k). \end{aligned} \quad (2.27)$$

More precisely, the dual edge sections $\widetilde{L}_x(i, j, k)^{(1)}$ and $\widetilde{L}_x(i, j, k)^{(2)}$ traverse two primary cells, which may have different permeability values μ_1 and μ_2 , respectively. The averaging of the inverse permeability along the dual edge leads to the desired relation. Namely, the averaged inverse permeability can be defined as follows

$$\overline{\mu^{-1}}(i, j, k) = \frac{\int \mu^{-1} ds}{\int ds}. \quad (2.28)$$

The normal component of the magnetic flux density is continuous at the intersection point. With the assumption that its variation in the vicinity of the intersection point is small, the following equation is valid

$$\widehat{b}_x(i, j, k) = \iint_{A_x(i, j, k)} \vec{B} \cdot d\vec{A} = \iint_{A_x(i, j, k)} B_x dy dz \approx B_x A_x(i, j, k). \quad (2.29)$$

With (2.29) and (2.27) the relation between \widehat{b} and \widehat{h} follows as

$$\widehat{b}_x(i, j, k) = \frac{A_x(i, j, k)}{\widetilde{L}_x(i, j, k) \overline{\mu^{-1}}(i, j, k)} \widehat{h}_x(i, j, k). \quad (2.30)$$

In matrix notation, the discrete analogue of (2.6b) is obtained as

$$\widehat{\mathbf{h}} = \mathbf{M}_{\mu^{-1}} \widehat{\mathbf{b}}. \quad (2.31)$$

The material equation for \mathbf{M}_ϵ can be derived with an analogous consideration using dual faces and primary edges. In this case, the averaged permittivity $\bar{\epsilon}(i, j, k) = \iint \epsilon \, dA / \iint dA$ is used. Summarizing, in case of linear, frequency-independent material, the discrete material relations read

$$\widehat{\mathbf{d}} = \mathbf{M}_\epsilon \widehat{\mathbf{e}} \quad (2.32a)$$

$$\widehat{\mathbf{h}} = \mathbf{M}_{\mu^{-1}} \widehat{\mathbf{b}}. \quad (2.32b)$$

Thus, the Maxwell's grid equations in terms of $\widehat{\mathbf{e}}$ and $\widehat{\mathbf{h}}$ together with the material equations read

$$\mathbf{C} \widehat{\mathbf{e}} = -\frac{d}{dt} \mathbf{M}_\mu \widehat{\mathbf{h}} \quad (2.33a)$$

$$\widetilde{\mathbf{C}} \widehat{\mathbf{h}} = \frac{d}{dt} \mathbf{M}_\epsilon \widehat{\mathbf{e}} \quad (2.33b)$$

$$\mathbf{S} \mathbf{M}_\mu \widehat{\mathbf{h}} = 0 \quad (2.33c)$$

$$\widetilde{\mathbf{S}} \mathbf{M}_\epsilon \widehat{\mathbf{e}} = 0. \quad (2.33d)$$

2.3.5 Boundary Conditions

In principle, the boundaries are defined in order to determine the local fields and to model the influence of the surrounding on the computational domain. They are diverse and correspond to the surrounding they model. Because the energy exchange with the surrounding does not take place when the superconducting resonators are analyzed, within this thesis the closed boundary conditions are applied. Commonly, the Dirichlet and the Neumann boundary conditions are used in such situations. The Dirichlet boundary condition forces the field solution to a specific value on the boundary, while the Neumann boundary condition sets the normal field derivative to a defined value at the boundary. For the special case of structures with perfectly electric surrounding, the ideal electric boundary conditions are obtained, which are implemented by using the Dirichlet boundary condition.

2.3.6 Time-Harmonic Fields (Frequency Domain)

For the solution of the time-dependent system of Maxwell's equations (2.23a)-(2.23d), which represent ordinary differential equations, a suitable method for their integration must be applied. However, in many cases the interest is to consider only the steady-state solution for the electromagnetic field (the so-called harmonic field) as produced by currents having sinusoidal time dependence. Any harmonic field vector oscillating at the frequency ω can be represented by a complex-phasor space vector, which is independent of time. The time derivative in the Maxwell's equations may then be substituted by denoting the time dependence of all quantities as $e^{j\omega t}$. For instance, the electric field vector \vec{E} can be written as

$$\vec{E}(\vec{r}, t) = \vec{E}(\vec{r}) \cos(\omega t + \varphi(\vec{r})) = \text{Re} \{ \vec{E}(\vec{r}) e^{j\varphi(\vec{r})} e^{j\omega t} \} = \text{Re} \{ \underline{\vec{E}}(\vec{r}) e^{j\omega t} \} \quad (2.34)$$

in which the $\underline{\vec{E}}$ denotes the complex-phasor space vector. By using the phasor representation, the time derivative d/dt may be replaced by the factor $j\omega$ since $de^{j\omega t}/dt = j\omega e^{j\omega t}$. Consequently, the time-derivative becomes an algebraic multiplication of the complex amplitude by the factor $j\omega$.

Hence, the Maxwell's grid equations (2.33a)-(2.33d) with steady-state sinusoidal time dependence become complex algebraic equations in FD, given as

$$\mathbf{C} \underline{\hat{\mathbf{e}}} = -j\omega \underline{\hat{\mathbf{b}}} \quad (2.35a)$$

$$\tilde{\mathbf{C}} \underline{\hat{\mathbf{h}}} = j\omega \underline{\hat{\mathbf{d}}} \quad (2.35b)$$

$$\mathbf{S} \underline{\hat{\mathbf{b}}} = 0 \quad (2.35c)$$

$$\tilde{\mathbf{S}} \underline{\hat{\mathbf{d}}} = 0, \quad (2.35d)$$

where the time dependence $e^{j\omega t}$ vanishes from both sides. The unknown discrete vectors with complex amplitude, e.g. $\underline{\hat{\mathbf{e}}}$ and $\underline{\hat{\mathbf{b}}}$, are called discrete phasors.

Discrete Curl-Curl Eigenvalue Equation

This section considers the case of homogeneous, isotropic, linear, and lossless matter ($\sigma = 0$, $\varepsilon, \mu \in \mathbb{R}$) in source free space. Analogously to the continuous wave equations, (2.11a) and (2.11b), by combining the first two grid Maxwell's equations, (2.35a)-(2.35b), and the discretized material equations, (2.32a)-(2.32b), an equation in terms of the electric $\underline{\hat{\mathbf{e}}}$ or the magnetic grid voltage $\underline{\hat{\mathbf{h}}}$ can be derived.

When the magnetic grid voltage $\widehat{\mathbf{h}}$ is eliminated, the discrete curl-curl equation has the following form

$$\mathbf{M}_\epsilon^{-1} \widetilde{\mathbf{C}} \mathbf{M}_{\mu-1} \mathbf{C} \widehat{\mathbf{e}} = \omega^2 \widehat{\mathbf{e}}. \quad (2.36)$$

Due to the discrete curl operators applied twice in succession this equation is called discrete curl-curl equation and corresponds to the continuous equation (2.11a) in frequency domain. Additionally, this is an algebraic eigenvalue problem of the form

$$\mathbf{A}_{\text{CC}} \widehat{\mathbf{e}} = \omega^2 \widehat{\mathbf{e}}. \quad (2.37)$$

The solutions of an equation of this type are non-trivial eigenvectors $e_i \neq 0$ and the associated real or complex eigenvalues ω_i^2 . A matrix of dimension n has always a maximum of n such linearly independent solutions. Consequently, the equation (2.36) is called a discrete curl-curl-eigenvalue equation with the system matrix

$$\mathbf{A}_{\text{CC}} = \mathbf{M}_\epsilon^{-1} \widetilde{\mathbf{C}} \mathbf{M}_{\mu-1} \mathbf{C} \quad (2.38)$$

and it corresponds to the continuous eigenvalue equation for resonators. The eigenvalues of the equation are the squared resonance frequencies ω_i^2 and the eigenvectors correspond to the fields of the associated cavity modes. The characteristics of the FIT discretization can be examined by analyzing the algebraic properties of the system matrix \mathbf{A}_{CC} . In the form of equation (2.36), this matrix is asymmetric. Therefore, the transformation

$$\widehat{\mathbf{e}}' = \mathbf{M}_\epsilon^{1/2} \widehat{\mathbf{e}} \quad (2.39)$$

is performed, where the $\mathbf{M}_\epsilon^{1/2}$ is defined as

$$\mathbf{M}_\epsilon^{1/2} \mathbf{M}_\epsilon^{1/2} = \mathbf{M}_\epsilon \quad \mathbf{M}_\mu^{1/2} \mathbf{M}_\mu^{1/2} = \mathbf{M}_\mu \quad (2.40a)$$

$$\mathbf{M}_\epsilon^{-1/2} \mathbf{M}_\epsilon^{-1/2} = \mathbf{M}_\epsilon^{-1} \quad \mathbf{M}_\mu^{-1/2} \mathbf{M}_\mu^{-1/2} = \mathbf{M}_\mu^{-1}. \quad (2.40b)$$

This leads to the formulation

$$\mathbf{M}_\epsilon^{-1/2} \widetilde{\mathbf{C}} \mathbf{M}_{\mu-1} \mathbf{C} \mathbf{M}_\epsilon^{-1/2} \widehat{\mathbf{e}}' = \omega^2 \widehat{\mathbf{e}}' \quad (2.41)$$

with the real symmetric system matrix

$$\begin{aligned} \mathbf{A}'_{\text{CC}} &= \mathbf{M}_\epsilon^{1/2} \mathbf{A}_{\text{CC}} \mathbf{M}_\epsilon^{-1/2} = \mathbf{M}_\epsilon^{-1/2} \widetilde{\mathbf{C}} \mathbf{M}_{\mu-1} \mathbf{C} \mathbf{M}_\epsilon^{-1/2} \\ &= (\mathbf{M}_\epsilon^{-1/2} \widetilde{\mathbf{C}} \mathbf{M}_\mu^{-1/2}) (\mathbf{M}_\epsilon^{-1/2} \widetilde{\mathbf{C}} \mathbf{M}_\mu^{-1/2})^T. \end{aligned} \quad (2.42)$$

Finally, the problem to be solved is

$$\mathbf{A}'_{\text{CC}} \underline{\hat{\mathbf{e}}}' = \omega^2 \underline{\hat{\mathbf{e}}}', \quad (2.43)$$

where the eigenvalues of \mathbf{A}_{CC} and \mathbf{A}'_{CC} remain identical. One objective of the thesis is to solve this large-scale eigenvalue problem with the capabilities to calculate thousands of eigenfrequencies for matrices with dimension in excess of several millions. The algorithms and the details towards the solution of the discrete standard eigenvalue problem will be discussed in chapter 4.

2.3.7 Transient Fields (Time Domain)

The calculation of the transient processes with the FIT is carried out for the already spatially discretized Maxwell's grid equations by a discretization of the time axis. Here, the time axis will be considered at discrete-time points t_m , which define a grid T

$$T := \{t_m \in \mathbb{R}^+ | t_0 \leq t_m \leq t_M, t_m := t_{m-1} + \Delta t_m\}. \quad (2.44)$$

In the following section, a formulation for the time-domain integration of the Maxwell's grid equations is presented. The approach integrates the complete Maxwell's grid equations in time and allows the numerical simulation of fast-changing problems. This thesis will employ the implementation of the Leapfrog algorithm from the transient solver in CST Microwave Studio® (CST MWS).

Leapfrog Algorithm

If the Maxwell's grid equations are applied to the transient problems with general time dependence, then in addition to the spatial operators the time derivatives must be still resolved. For high-frequency applications, the so-called Leapfrog scheme has been proved to work successfully for the time integration. In the context of simulation of electromagnetic fields, the scheme was first described by Kane S. Yee in 1966 [85]. The FDTD, proposed by Yee, in the simplest case for Cartesian grids coincides with the FIT in TD, as described in the following.

The starting point of the procedure, is to write the first two Maxwell's grid equations in the form of

$$\frac{d}{dt} \hat{\mathbf{h}}(t) = -\mathbf{M}_{\mu-1} \mathbf{C} \hat{\mathbf{e}}(t) \quad (2.45a)$$

$$\frac{d}{dt} \hat{\mathbf{e}}(t) = \mathbf{M}_{\epsilon}^{-1} \tilde{\mathbf{C}} \hat{\mathbf{h}}(t). \quad (2.45b)$$

With respect to the time derivatives this is a system of ordinary differential equations of first order. The discretization of the time derivatives for the above equations is carried out on an equidistant grid T of the time axis [81]. For example, if the function $f(t)$ is sampled at the time intervals $t_m := t_0 + m \Delta t$, the derivative $f'(t)$ can be approximated in the center of each two samples, that is at half time steps

$$t_{m+1/2} := t_0 + (m + 1/2) \Delta t. \quad (2.46)$$

That means

$$f'(t_0 + (m + 1/2) \Delta t) = \frac{f(t_0 + (m + 1) \Delta t) - f(t_0 + m \Delta t)}{\Delta t} + \mathcal{O}(\Delta t^2) \quad (2.47)$$

or

$$f'(m+1/2) = \frac{f^{(m+1)} - f^{(m)}}{\Delta t} + \mathcal{O}(\Delta t^2). \quad (2.48)$$

As suggested from above, the error of this approximation is of second order of the time step size.

The time-dependent Maxwell's grid equations (2.45a)-(2.45b) connect the time derivative of the discrete vector, $\widehat{\mathbf{e}}$ or $\widehat{\mathbf{h}}$, with the other vector. For the time discretization, one of the vectors can be evaluated on the whole time steps $t_0 + m \Delta t$ of the time grid, while the other vector is discretized on the half time steps $t_0 + (m + 1/2) \Delta t$. If arbitrarily will be chosen that the magnetic grid voltage is discretized on the whole time steps

$$\widehat{\mathbf{h}}^{(m)} := \widehat{\mathbf{h}}(t_m = t_0 + m \Delta t), \quad (2.49)$$

then according to the above principle it must be also set that

$$\widehat{\mathbf{e}}^{(m+1/2)} := \widehat{\mathbf{e}}(t_{m+1/2} = t_0 + (m + 1/2) \Delta t). \quad (2.50)$$

When the time derivatives

$$\frac{d}{dt} \widehat{\mathbf{h}}^{(m+1/2)} \approx \frac{\widehat{\mathbf{h}}^{(m+1)} - \widehat{\mathbf{h}}^{(m)}}{\Delta t} \quad (2.51a)$$

$$\frac{d}{dt} \widehat{\mathbf{e}}^{(m+1)} \approx \frac{\widehat{\mathbf{e}}^{(m+3/2)} - \widehat{\mathbf{e}}^{(m+1/2)}}{\Delta t} \quad (2.51b)$$

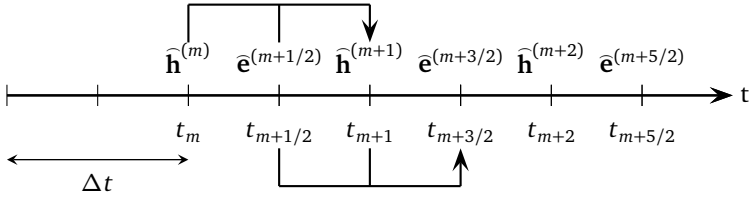


Figure 2.6.: Update scheme of the Leapfrog method in which the magnetic grid voltages are evaluated at the whole time steps $t_m = t_0 + m \Delta t$ and the electric grid voltages at the half time steps $t_{m+1/2} = t_0 + (m + 1/2) \Delta t$. The recursion includes each of the magnetic and the electrical parameters of the last time step with length Δt .

are inserted into (2.45a) and (2.45b), the Leapfrog method follows as

$$\widehat{\mathbf{h}}^{(m+1)} := \widehat{\mathbf{h}}^{(m)} - \Delta t \mathbf{M}_{\mu^{-1}} \mathbf{C} \widehat{\mathbf{e}}^{(m+1/2)} \quad (2.52a)$$

$$\widehat{\mathbf{e}}^{(m+3/2)} := \widehat{\mathbf{e}}^{(m+1/2)} + \Delta t \mathbf{M}_{\epsilon}^{-1} \widetilde{\mathbf{C}} \widehat{\mathbf{h}}^{(m+1)}. \quad (2.52b)$$

The update equations (2.52a) and (2.52b) define a recursion, in which the new vectors can be calculated by using the old values of $\widehat{\mathbf{e}}$ and $\widehat{\mathbf{h}}$. This solution employs an explicit formula and does not solve system of equations. The update scheme of the Leapfrog method in which the magnetic grid voltages are evaluated at the whole time steps $t_m = t_0 + m \Delta t$ and the electric grid voltages at the half time steps $t_{m+1/2} = t_0 + (m + 1/2) \Delta t$ is given with figure 2.6.

The Leapfrog scheme, as an explicit recursion method, in which only one old vector must be used (and saved!), has a nearly optimal efficiency in the computational time of rapidly changing problems [30]. Since the algorithm only includes matrix-vector multiplications and vector additions, the algorithm effort is comparatively low and the practicability on the modern computer architectures is very good.

2.4 Finite Element Method

The Finite Element Method (FEM) is a standard tool for solving differential equations in many disciplines, e.g., electromagnetics, solid and structural mechanics,

fluid dynamics, acoustics, and thermal conduction. The differential equations to be solved by the FEM are given with

$$F u(x, t) = b(x, t), \quad (2.53)$$

in the spatial domain Ω with the following boundary conditions

$$f_s(u, t) = h(x, t) \text{ on the boundary } \partial\Omega. \quad (2.54)$$

In the above equations, F is an operator, b denotes the source, and u is the unknown function that has to be numerically determined. Furthermore, x is a generic point of the domain Ω , whereas t stands for a time instant. As a matter of choice, the functions could depend on the frequency of operation f , instead of t .

Jin [38] and Peterson [63] give good accounts of the FEM for electromagnetics. Additionally, more mathematical treatments of the same topic are given in [52, 19]. This chapter gives an introduction to the FEM for the Maxwell's equations. A very high advantage of the FEM and certainly, the main reason why it is a broadly used method in many branches of engineering, is its ability to deal with complex geometries by using unstructured grids. Moreover, the unstructured grids allow for higher resolution locally in order to resolve fine geometries and rapid variations of the solution. Additionally, a strong point of the FEM is that it provides a well-defined representation of the sought function everywhere in the solution domain. This makes it possible to apply many mathematical tools and prove important properties concerning the stability and the convergence.

On the other side, a disadvantage of the FEM is that the explicit formulas for the field updates in the time-domain simulations cannot be derived in the general case. Instead, a linear system of equations has to be solved. Consequently, the FEM requires more computer resources, both in terms of computational time and memory consumptions.

When using the FEM, the solution of a specific problem attains three steps: space discretization, solution approximation, and equation approximation [54]. In the following sections an overview of each step will be shortly presented as well as the solution of the electromagnetic problem for a superconducting cavity will be systematically derived by employing the FEM.

2.4.1 Space Discretization

At this step, the solution domain Ω is subdivided into cells, or elements. For the space discretization, the FEM can use in principle any type of geometric ele-

ments. Usually, the unstructured grids could be consisted of triangles, rectangles, or quadrilaterals in two dimensions whereas tetrahedrons, hexahedra, and prisms can be exploited in the 3D case. The employment of the unstructured meshes, for instance with tetrahedrons, allows good representations of curved structures, which can be very hardly (or impossibly) approximated on Cartesian grids. Due to the fact that this thesis deals with cavities having curved boundaries, the tetrahedral meshes have been used for their approximation.

2.4.2 Solution Approximation

After the space discretization is done, the solution should be approximated by an expansion in a finite number of basis functions. Namely, the spatial variation of the sought solution is described as a linear combination of space-dependent basis functions

$$u(x) = \sum_{j=1}^n a_j w_j(x), \quad (2.55)$$

where x is a point in the solution domain Ω , w_j represents a basis function, and a_j expresses an unknown coefficient of the linear combination.

Generally, the basis functions have a number of common characteristics. In most cases they are nonzero only on a small sub-domain of Ω , i.e. they are functions with compact support. This choice makes the integration of the functions on the solution domain easier to be calculated. Additionally, they are typically polynomials and a common choice is that of linear basis functions, i.e. polynomials of first degree. However, in this thesis higher order polynomials will be used to increase the accuracy of the solution while maintaining a relatively coarse spatial discretization mesh [7].

The type of the basis functions should be appropriate to the type of the main unknown of the problem. Thus, the choice is between scalar and vectorial basis functions. On the one hand, the scalar basis functions are allocated either on nodes (scalar potential) or volumes (electric charge), and on the other hand, the vectorial basis functions could be allocated on edges (field intensities) or surfaces (flux densities). That is, if a mesh with N nodes, E edges, F facets, and T tetrahedra is considered, then the geometric elements of the mesh on which the basis functions can be aligned are:

- nodes (not oriented entities)
- edges with an orientation given by the order of the nodes,

- faces with an orientation also defined by the order of the nodes (whereby, a cyclic permutation of the nodes expresses the same face), or
- volumes (not oriented entities).

To deal with vector quantities, such as the electric field strength \vec{E} , a first attempt might be to expand each vector component separately in nodal basis functions. However, it turned out that such an approach leads to nonphysical solutions, referred to as spurious modes. This can be avoided by using edge elements [57], which are very well suited for approximating electromagnetic fields. Once the type of the geometric entity is chosen, the basis functions for the edge elements are constructed such that their tangential components are continuous across the element borders, whereas their normal components are allowed to be discontinuous. Each geometric element (e.g. edge) allocates one basis function. That is, each edge has an “own” basis function and each basis function “lives” on an “own” edge. The magnitude of each edge basis function is normalized such that the integral of the function on the own edge is 1 and it is zero on all other edges.

For the incomplete first order elements, there are few choices of basis functions. Each basis function has a constant tangential component along one edge and zero tangential component along all the other edges. However, for higher order elements there are more alternatives and many bases have been presented in the literature. These can be divided into two groups: interpolatory bases [33] and hierarchical bases [77]. The most popular bases today are the hierarchical, and previous sets of the hierarchical basis functions include those by Webb [77], which will be used within this thesis [36]. Webb uses results for an equilateral tetrahedron to make the basis functions as orthogonal as possible in an L^2 -sense.

2.4.3 Equation Approximation

Weighted Residuals

In case that the problem to be solved (2.53)-(2.54) would be approached with an analytical approach, the unknown solution u would be available in each point of the spatial domain Ω . Otherwise, if a numerical technique is exploited, the unknown u can only be calculated in a finite number of points and therefore, the relation (2.53) will not be satisfied exactly in each point of Ω .

The residual of the equation $f(u) = b$ is formed as

$$R(x) = f(u(x)) - b(x), \tag{2.56}$$

where x is a generic point of Ω . In case that u is the exact solution, then the residual will be zero in every point of the domain as desirable

$$R(x) = 0, \forall x \in \Omega. \quad (2.57)$$

However, in general, it is not required that the residual is zero pointwise, but to be zero in the so-called weak sense by forcing the average of the weighted residual on the whole domain Ω to be zero

$$\int_{\Omega} g(x)R(x) dV = 0, \forall g \in U, \quad (2.58)$$

where g is a weighting function belonging to a function space U . This relation is usually denoted as a projection of the residual R on the function g . It should be fulfilled for all the functions g that belong to the space U . On the occasion that there are n geometric entities in the mesh, then the dimension of U must be also n . Assuming that there is a basis for the space U , then all the functions of U can be written as linear combinations of the functions in this basis. In this case, if the equation (2.58) is fulfilled for the n basis functions of the space U , the relation will be also fulfilled for any other function of U . Consequently, it is sufficient to perform the projection from (2.58) only for each basis function of the space U

$$\int_{\Omega} g_k(x)R(x) dV = 0, \forall g_k \in \text{the basis of } U, \quad (2.59)$$

with

$$R(x) = f(u(x)) - b(x). \quad (2.60)$$

After insertion of the expression (2.55) into (2.59), a linear system of n equations with the n unknowns a_j , $j = 1 \dots n$ is obtained

$$\int_{\Omega} g_k \cdot f\left(\sum_{j=1}^n a_j w_j\right) dV = \int_{\Omega} g_k \cdot b dV, k = 1 \dots n. \quad (2.61)$$

The functions w_j in the representation of the unknown u are called trial functions, whereas the functions g_k on which the projection is made are called test functions. A well-known variant of the FEM is the Galerkin's method, in which the weighting (test) functions are the same as the trial functions.

The Curl-Curl Equation

In this section, the wave equation in harmonic state will be considered as well as a domain of space with linear, time-invariant material parameters. As already mentioned, this thesis deals with the problem of determining the eigenfrequencies of a closed cavity with perfect metallic walls and therefore, in the following loss-free and source-free problem will be analyzed. When the complex transformation is applied to the first two time-dependent Maxwell's equations, it results in the following system of equations

$$j\omega \underline{\vec{B}} + \nabla \times \underline{\vec{E}} = 0 \quad (2.62a)$$

$$\nabla \times \underline{\vec{H}} = j\omega \underline{\vec{D}} = 0 \quad (2.62b)$$

together with the material relations

$$\underline{\vec{B}} = \mu \underline{\vec{H}} \quad (2.63a)$$

$$\underline{\vec{D}} = \varepsilon \underline{\vec{E}}. \quad (2.63b)$$

The second-order equation in terms of the electric field strength can be derived by combining the above equations. For a cavity with perfect metallic walls, the tangential component of the electric field strength on the boundary will be zero

$$n \times \underline{\vec{E}} = 0 \text{ on } \partial\Omega, \quad (2.64)$$

whereas the electromagnetic field within the domain Ω will be defined by the following second-order equation

$$\nabla \times (\nabla \times \underline{\vec{E}}) - \omega^2 \mu \varepsilon \underline{\vec{E}} = 0. \quad (2.65)$$

Edge Elements

Under the assumption that the edge basis functions are denoted by \vec{w}^e , then they will belong to the basis of the space of edge functions \vec{W}^e . According to the equation (2.55), the solution $\underline{\vec{E}}$ can be expanded as a linear combination of the basis functions \vec{w}^e

$$\underline{\vec{E}}(\vec{x}) = \sum_{j=1}^E e_j \vec{w}_j^e(\vec{x}), \quad (2.66)$$

where E is the total number of mesh edges and e_j denotes the unknown electric voltage along an edge of the mesh. The essential boundary conditions for the electric field strength require that $\underline{\vec{E}}$ has zero tangential component on the boundaries.

Thereupon, they have to be imposed directly on the solution. In other words, the solutions in a space of functions, which satisfy the essential boundary conditions, are sought. The space is given with W^0

$$\vec{E} \in W^0 = \{\vec{w} : \vec{w} \in W^e, \vec{n} \times \vec{w} = 0 \text{ on } \partial\Omega\}. \quad (2.67)$$

The natural boundary conditions do not need to be imposed a-priori in the FEM formulation, since they are built-in directly in a natural manner.

Transformation of the Equation

In the next step, a projection of the equation (2.65) is performed on a test field \vec{E}' , followed by a transformation using the generalized integration by parts and the Gauss theorem [54]. Firstly, the equation (2.65) is multiplied by the test field \vec{E}' and then integrated on the domain Ω

$$\int_{\Omega} \nabla \times (\nabla \times \vec{E}) \cdot \vec{E}' = \int_{\Omega} \omega^2 \mu \varepsilon \vec{E} \cdot \vec{E}', \quad (2.68)$$

where the elementary volume dV is omitted and self-understood. In the Galerkin's method, the test functions belong to the same space as the trial functions, i.e. the space of edge functions

$$\vec{E}' \in W^e. \quad (2.69)$$

In order to reduce the order of the space-derivatives by one, the following analysis formula will be used to transform the left-hand side of the equation (2.68)

$$\nabla \cdot (\vec{F} \times \vec{G}) = (\nabla \times \vec{F}) \cdot \vec{G} - (\nabla \times \vec{G}) \cdot \vec{F}. \quad (2.70)$$

Consequently, the integrand in the left-hand side of (2.68) can be re-written as

$$\nabla \times (\nabla \times \vec{E}) \cdot \vec{E}' = (\nabla \times \vec{E}) \cdot (\nabla \times \vec{E}') + \nabla \cdot ((\nabla \times \vec{E}) \times \vec{E}') \quad (2.71)$$

and the equation (2.68) becomes

$$\int_{\Omega} (\nabla \times \vec{E}) \cdot (\nabla \times \vec{E}') + \int_{\Omega} \nabla \cdot ((\nabla \times \vec{E}) \times \vec{E}') = \int_{\Omega} \omega^2 \mu \varepsilon \vec{E} \cdot \vec{E}'. \quad (2.72)$$

By applying the Gauss' theorem, the second term in the left-hand side of the above equation can be converted into a surface integral

$$\int_{\Omega} \nabla \cdot \vec{F} \, dV = \int_{\partial\Omega} \vec{F} \cdot \vec{n} \, dA, \quad (2.73)$$

resulting in the following form of the equation (2.72)

$$\int_{\Omega} (\nabla \times \underline{\vec{E}}) \cdot (\nabla \times \underline{\vec{E}}') + \int_{\partial\Omega} \vec{n} \cdot ((\nabla \times \underline{\vec{E}}) \times \underline{\vec{E}}') = \int_{\Omega} \omega^2 \mu \epsilon \underline{\vec{E}} \cdot \underline{\vec{E}}'. \quad (2.74)$$

The boundary conditions do not provide any information about the behaviour of $\nabla \times \underline{\vec{E}}$ on the boundaries. Therefore, the second integral in the left-hand side of equation (2.74) cannot be evaluated. However, using the cyclic permutation property

$$\vec{n} \cdot ((\nabla \times \underline{\vec{E}}) \times \underline{\vec{E}}') = (\nabla \times \underline{\vec{E}}) \cdot (\underline{\vec{E}}' \times \vec{n}), \quad (2.75)$$

the second term can be eliminated if the tangential component of the test field $\underline{\vec{E}}'$ vanishes on the boundaries. For this purpose, the test functions $\underline{\vec{E}}'$ are chosen to fulfill this condition too. Finally, the weak FEM formulation of the eigenmode problem is as follows: for all $\underline{\vec{E}}' \in W^0$, find $\underline{\vec{E}} \in W^0$ and $\omega \in \mathbb{R}$ such that

$$\int_{\Omega} (\nabla \times \underline{\vec{E}}) \cdot (\nabla \times \underline{\vec{E}}') = \omega^2 \int_{\Omega} \mu \epsilon \underline{\vec{E}} \cdot \underline{\vec{E}}'. \quad (2.76)$$

2.4.4 Matrix Assembly

At this point, the discretized form of the unknown vector field $\underline{\vec{E}}$ is included into the weak formulation (2.76) and the test function $\underline{\vec{E}}'$ is chosen to be a basis function of the edge-element function space

$$\underline{\vec{E}}' = \vec{w}_i^e. \quad (2.77)$$

Subsequently, this leads to

$$\int_{\Omega} \left(\nabla \times \left(\sum_{j=1}^E e_j \vec{w}_j^e \right) \right) \cdot (\nabla \times \vec{w}_i^e) = \omega^2 \int_{\Omega} \mu \epsilon \left(\sum_{j=1}^E e_j \vec{w}_j^e \right) \cdot \vec{w}_i^e, \quad i = 1 \dots E. \quad (2.78)$$

The coefficients e_j are independent of the point of space and therefore, they can be taken out of the integral on Ω

$$\sum_{j=1}^E e_j \int_{\Omega} (\nabla \times \vec{w}_i^e) \cdot (\nabla \times \vec{w}_j^e) = \omega^2 \sum_{j=1}^E e_j \int_{\Omega} \mu \varepsilon \vec{w}_i^e \cdot \vec{w}_j^e, \quad i = 1 \dots E. \quad (2.79)$$

Finally, when this equation is written for all the values of $i = 1 \dots E$, it represents a system of equations of the form

$$\mathbf{A} \mathbf{e} = \omega^2 \mathbf{B} \mathbf{e} \quad (2.80)$$

with the matrix coefficients

$$A_{ij} = \int_{\Omega} (\nabla \times \vec{w}_i^e) \cdot (\nabla \times \vec{w}_j^e) \quad (2.81)$$

and

$$B_{ij} = \int_{\Omega} \mu \varepsilon \vec{w}_i^e \cdot \vec{w}_j^e. \quad (2.82)$$

The resulting problem (2.80) is referred to as the generalized eigenvalue problem, which has motivated this work and its solution will be explained in section 4.3 on page 69. The actual computation of the integrals in the expressions of the matrix coefficients is performed by writing the integral on the domain as a sum of integrals on each individual element t

$$A_{ij} = \sum_{t=1}^T \int_t (\nabla \times \vec{w}_i^e) \cdot (\nabla \times \vec{w}_j^e). \quad (2.83)$$

As the expressions of the edge functions on a particular tetrahedron are analytically known, the above integrals can be easily calculated, either analytically or by numerical integration. It should be pointed out that although the sum extends over all the tetrahedra in the mesh, only a few elements will make a nonzero contribution to A_{ij} . More precisely, only those tetrahedra, which contain the both nodes i and j , will cause a nonzero contribution. On the other tetrahedra, \vec{w}_i^e or \vec{w}_j^e will be zero due to the compact support of the edge functions. Therefore, the integrals on the tetrahedra will be also zero.

It can be shown that the obtained linear system of equations has the same form as in the FIT. Particularly,

$$\mathbf{A} = \mathbf{C}^T \mathbf{M}_{\mu^{-1}} \mathbf{C} \quad (2.84)$$

and

$$\mathbf{B} = \mathbf{M}_{\epsilon}, \quad (2.85)$$

in which the discrete curl matrix \mathbf{C} is exactly the same as in the case of FIT for a given mesh. The difference between the two methods lies in the material matrices \mathbf{M}_{ϵ} and $\mathbf{M}_{\mu^{-1}}$, which can be diagonal in the case of FIT on Cartesian meshes. In the FEM they are always non-diagonal and their elements are given with

$$(\mathbf{M}_{\epsilon})_{ij} = \int_{\Omega} \mu \epsilon \vec{w}_i^e \cdot (\nabla \times \vec{w}_j^e) \quad (2.86)$$

and

$$(\mathbf{M}_{\mu^{-1}})_{ij} = \int_{\Omega} \vec{w}_i^f \cdot (\nabla \times \vec{w}_j^f), \quad (2.87)$$

where \vec{w}_i^f is the face basis function allocated on the face i .

3 Eigenvalue Extraction from Time-Domain Computations

In this chapter, a fast approach for an accurate eigenfrequency extraction is addressed, taken into consideration the evaluated electric field computations in Time Domain (TD) of a superconducting resonant structure. Upon broadband excitation of the cavity, the electric field intensity is recorded at different detection probes inside the cavity. Thereafter, Fourier analysis of the recorded signals is performed and by means of fitting techniques with the theoretical cavity response model (in support of the applied excitation) the requested eigenfrequencies are extracted by finding the optimal model parameters in the least squares sense.

The chapter proceeds as follows. Due to the fact that the desired eigenfrequencies are calculated with the help of the Fourier analysis, the first section of this chapter reviews the fundamental basis of the Fourier transform. Additionally, digital signal processing techniques are also applied to the data obtained by the fast time-domain calculations and therefore, a detailed overview of the used techniques is given in sections 3.4 and 3.3. Section 3.5 presents the proposed time-domain approach for high-precision eigenfrequency extraction given the available electric field computations. Here, the fundamental modeling of the analyzed structure is described and the used signal-processing techniques are discussed, followed by a description of the functionality extension. Namely, the last section of this chapter addresses an extension of the approach for an accurate eigenfrequency extraction, taken into consideration the evaluated electric field computations in time domain of a superconducting resonant structure.

3.1 Fourier Analysis

The real-world signals are usually continuous. However, when these signals are to be generated, simulated, or analyzed by computers, they are approximated by samples, where the sampling process results in discrete-time signals. Additionally, the signals can be represented either in time or frequency domain. The frequency-domain representation is developed using the Fourier series and the Fourier transform [75]. The Fourier theory originated from the approximation theory, where a time function is represented by series of weighted basis functions with known

forms. The Fourier representation provides an insight into the frequency contents of the signal and hence, the signals are usually characterized by the shape and the width of their frequency spectrum.

3.1.1 Fourier Series of Functions with Periodicity $2p$

One of the most essential and useful tools for mathematical analysis of all kinds of wave forms is the Fourier series, named after the French mathematical physicist Jean Baptiste Joseph Fourier (1768-1830). Besides for the solution of the partial differential equations with boundary conditions, the Fourier analysis is ubiquitous in almost all fields of physical sciences [75, 43]. In 1822, Fourier in his work on heat flow made a remarkable assertion that every function $f(t)$ with a period $2p$ ($f(t + 2p) = f(t)$) can be represented by a trigonometric infinite series of the form

$$f(t) = \sum_{n=0}^{\infty} (a_n \cos \omega_n t + b_n \sin \omega_n t), \quad (3.1)$$

where

$$a_0 = \frac{1}{2p} \int_{-p}^p f(t) dt, \quad (3.2)$$

$$a_n = \frac{1}{p} \int_{-p}^p f(t) \cos \omega_n t dt, \quad n = 1, 2, \dots, \quad (3.3)$$

$$b_n = \frac{1}{p} \int_{-p}^p f(t) \sin \omega_n t dt, \quad n = 1, 2, \dots \quad (3.4)$$

An infinite series of this form is called a Fourier series and with very little restrictions on the function, this is indeed the case. The coefficients a_n and b_n are known as the Euler formulas for the Fourier coefficients, or simply as the Fourier coefficients. In essence, the Fourier series decomposes the periodic function into cosine and sine waves. From the procedure, it can be observed that:

- The first term $\frac{1}{2} a_0$ describes the average value of $f(t)$ over a period $2p$.
- The term $a_n \cos \omega_n t$ characterizes the cosine wave with amplitude a_n , and n is the number of complete cosine waves in one period $2p$.
- The term $b_n \sin \omega_n t$ characterizes the sine wave with amplitude b_n . One period of $2p$ contains n complete sine waves.

- Practically, a_n and b_n are expected to decrease as n increases.

3.1.2 The Fourier Transform

The Fourier transform is a generalization of the Fourier series [75], which provides representations, in terms of a superposition of sinusoidal waves, for functions defined over an infinite interval. Similar as the Laplace transform, the Fourier transform is a member of a class of representations known as integral transforms. Except of being useful in solving differential equations, the Fourier transform has become a stepping stone in diverse applications. For example, it allows a look at the wave functions either in the coordinate space or in the momentum space. In the information theory, the Fourier transform enables to examine a wave form from the perspective of both the time and the frequency domain.

The Fourier series is very useful to represent periodic functions. However, some functions of interest, such as a single unrepeated pulse of force or voltage, are non-periodic over an infinite range. In such a case, it could be still imagined that the functions are periodic with the period approaching the infinity and the Fourier series becomes the Fourier integral. To extend the concept of Fourier series to non-periodic functions, first a function $f(t)$ (3.1), which repeats itself after an interval of $2p$, is considered. The angular frequency is defined as

$$\omega_n = 2\pi f_n = 2\pi \frac{n}{2p} = \frac{n\pi}{p} \text{ and } \Delta\omega = \omega_{n+1} - \omega_n = \frac{\pi}{p}. \quad (3.5)$$

From equation (3.5) it could be seen that as p increases, the discrete spectrum becomes more and more dense. It will approach a continuous spectrum ω_n ($\Delta\omega \rightarrow 0$) as $p \rightarrow \infty$ and the Fourier series appears to be an integral. This is indeed the case, if $f(t)$ is absolutely integrable over the infinite range.

The Fourier series of a function repeating itself in the interval of $2p$, can also be written in the complex form

$$f(t) = \sum_{n=-\infty}^{\infty} c_n e^{i\omega_n t}, \quad c_n = \frac{1}{2p} \int_{-p}^p f(t) e^{-i\omega_n t} dt. \quad (3.6)$$

Allowing a period $p \rightarrow \infty$, the Fourier integral can be derived. Given that the time-domain function $f(t)$ is piecewise continuous and differentiable function as well

as absolutely integrable (that is $\int_{-\infty}^{\infty} |f(t)| dt$ is finite), the process of transforming it into the same function in frequency domain $\widehat{f}(\omega)$ is expressed as,

$$\mathcal{F}\{f(t)\} = \int_{-\infty}^{\infty} f(t) e^{-i\omega t} dt = \widehat{f}(\omega). \quad (3.7)$$

The coefficient function $\widehat{f}(\omega)$ with an angular frequency $\omega = 2\pi f$ is known as the Fourier transform of $f(t)$ [60]. The complex function $\widehat{f}(\omega)$ can be expressed by a real and an imaginary part, or in the form of an amplitude and a phase

$$\widehat{f}(\omega) = \widehat{f}_{re}(\omega) + i \widehat{f}_{im}(\omega) = A(\omega) e^{iP(\omega)}, \quad (3.8)$$

where $\widehat{f}_{re}(\omega)$ is the absorption part and $\widehat{f}_{im}(\omega)$ is the dispersion part. The amplitude spectrum is given by

$$|A(\omega)| = \sqrt{(\widehat{f}_{re}(\omega))^2 + (\widehat{f}_{im}(\omega))^2}, \quad (3.9)$$

and the phase spectrum by

$$P(\omega) = \arctan(\widehat{f}_{re}(\omega) / \widehat{f}_{im}(\omega)). \quad (3.10)$$

The process of getting back from $\widehat{f}(\omega)$ to $f(t)$ is known as an inverse Fourier transform

$$\mathcal{F}^{-1}\{\widehat{f}(\omega)\} = \frac{1}{2\pi} \int_{-\infty}^{\infty} \widehat{f}(\omega) e^{i\omega t} d\omega = f(t). \quad (3.11)$$

The multiplicative factor $\frac{1}{2\pi}$ can vary, dependently on the conventions.

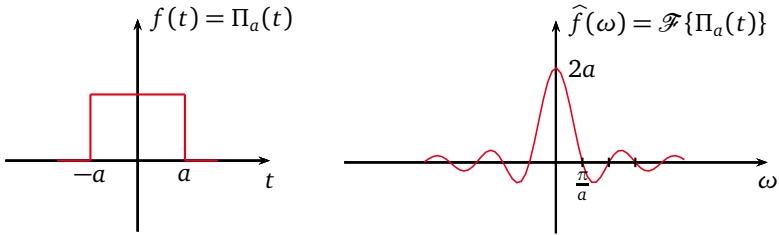
3.1.3 Transform Pairs

A short table of Fourier transforms is given in table A.1 on page 121 [75].

Rectangular Pulse Function

The rectangular function (also called box or top-hat function) is defined as

$$\Pi_a(t) = \begin{cases} 1 & -a \leq t \leq a, \\ 0 & \text{otherwise.} \end{cases} \quad (3.12)$$



(a) Rectangular function

(b) Fourier transform of a rectangular function

Figure 3.1.: Fourier transform pair of a rectangular pulse function. (a) Rectangular pulse function. (b) Fourier transform of a rectangular pulse function. It should be noted that $\hat{f}(0) = 2a$ and the zeros of $\hat{f}(\omega)$ are at $\omega = \pi/a, 2\pi/a, 3\pi/a$, and so on.

The rectangular pulse function can be expressed as a summation of Heaviside step functions

$$\Pi_a(t) = u(t + a) - u(t - a). \quad (3.13)$$

Here, $u(t)$ is a Heaviside step function defined as

$$u(t) = \begin{cases} 1 & t > 0, \\ 0 & t < 0. \end{cases} \quad (3.14)$$

The Fourier transform of the rectangular pulse function is given by

$$\begin{aligned} \mathcal{F}\{\Pi_a(t)\} &= \int_{-\infty}^{\infty} \Pi_a(t) e^{-i\omega t} dt = \int_{-a}^a e^{-i\omega t} dt = \\ &= \frac{e^{-i\omega t}}{-i\omega} \Big|_{-a}^a = \frac{e^{-i\omega a} - e^{i\omega a}}{-i\omega} = \frac{2 \sin \omega a}{\omega} = \hat{f}(\omega). \end{aligned} \quad (3.15)$$

In terms of a cardinal sine function defined as $\text{sinc}(x) = \frac{\sin x}{x}$, it can be obtained that

$$\mathcal{F}\{f(t)\} = 2a \text{sinc}(a\omega). \quad (3.16)$$

This Fourier transform pair is shown in figure 3.1.

Gaussian Function

If a Gaussian function is defined as

$$f(t) = e^{-at^2}, \quad (3.17)$$

its Fourier transform is given by

$$\mathcal{F}\{e^{-at^2}\} = \int_{-\infty}^{\infty} e^{-at^2} e^{-i\omega t} dt = \int_{-\infty}^{\infty} e^{-at^2 - i\omega t} dt = \widehat{f}(\omega). \quad (3.18)$$

Completing the square of the exponential

$$\alpha t^2 + i\omega t = \left(\sqrt{\alpha} t + \frac{i\omega}{2\sqrt{\alpha}}\right)^2 + \frac{\omega^2}{4\alpha}, \quad (3.19)$$

it follows

$$\begin{aligned} \int_{-\infty}^{\infty} \exp\left\{-\left[\left(\sqrt{\alpha} t + \frac{i\omega}{2\sqrt{\alpha}}\right)^2 + \frac{\omega^2}{4\alpha}\right]\right\} dt \\ = \exp\left(-\frac{\omega^2}{4\alpha}\right) \int_{-\infty}^{\infty} \exp\left\{-\left(\sqrt{\alpha} t + \frac{i\omega}{2\sqrt{\alpha}}\right)^2\right\} dt. \end{aligned} \quad (3.20)$$

Applying the following substitution

$$u = \sqrt{\alpha} t + \frac{i\omega}{2\sqrt{\alpha}}, \quad du = \sqrt{\alpha} dt \quad (3.21)$$

the Fourier transform can be written as

$$\widehat{f}(\omega) = \exp\left(-\frac{\omega^2}{4\alpha}\right) \frac{1}{\sqrt{\alpha}} \int_{-\infty}^{\infty} e^{-u^2} du. \quad (3.22)$$

In view of the fact that

$$\int_{-\infty}^{\infty} e^{-u^2} du = \sqrt{\pi}, \quad (3.23)$$

it follows

$$\widehat{f}(\omega) = \sqrt{\frac{\pi}{\alpha}} \exp\left(-\frac{\omega^2}{4\alpha}\right). \quad (3.24)$$

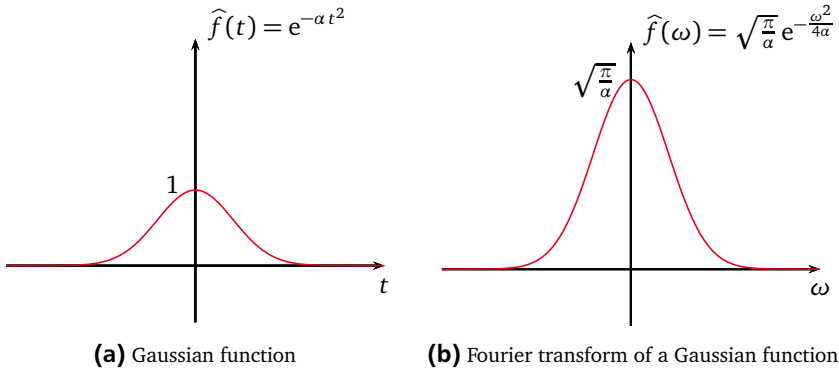


Figure 3.2.: Fourier transform pair of a Gaussian function. (a) Gaussian function ($\alpha = 1$). (b) Fourier transform of a Gaussian function. The result is another Gaussian function.

It is interesting to note that $\hat{f}(\omega)$ is also a Gaussian function with a peak at the origin. In case of $f(t)$ being sharply peaked (large α), then $\hat{f}(\omega)$ is flattened, and vice versa. This is a general feature in the theory of Fourier transforms. The Fourier transform pair of a Gaussian function is shown in figure 3.2.

3.1.4 Properties of the Fourier Transform

There are several important properties for the Fourier transform [75, 22], which will be used throughout this work and therefore, discussed in the following.

Symmetry Property

The symmetry property of the Fourier transform can help to avoid many complicated mathematical manipulations and it is defined as

$$\text{if } \mathcal{F}\{f(t)\} = \hat{f}(\omega), \text{ then } \mathcal{F}\{\hat{f}(t)\} = 2\pi f(-\omega). \quad (3.25)$$

Linearity Property

If $\mathcal{F}\{f(t)\} = \hat{f}(\omega)$ and $\mathcal{F}\{g(t)\} = \hat{g}(\omega)$, then

$$\begin{aligned}\mathcal{F}\{af(t) + bg(t)\} &= \int_{-\infty}^{\infty} [af(t) + bg(t)] e^{-i\omega t} dt \\ &= a \int_{-\infty}^{\infty} f(t) e^{-i\omega t} dt + b \int_{-\infty}^{\infty} g(t) e^{-i\omega t} dt \\ &= a \mathcal{F}\{f(t)\} + b \mathcal{F}\{g(t)\} = a \hat{f}(\omega) + b \hat{g}(\omega).\end{aligned}\tag{3.26}$$

Similarly,

$$\begin{aligned}\mathcal{F}^{-1}\{a \hat{f}(\omega) + b \hat{g}(\omega)\} &= a \mathcal{F}^{-1}\{\hat{f}(\omega)\} + b \mathcal{F}^{-1}\{\hat{g}(\omega)\} \\ &= af(t) + bg(t).\end{aligned}\tag{3.27}$$

Time Shifting

In case that the time is shifted by a , in the Fourier transform

$$\mathcal{F}\{f(t - a)\} = \int_{-\infty}^{\infty} f(t - a) e^{-i\omega t} dt,\tag{3.28}$$

after substituting $t - a = x$, $dt = dx$, $t = x + a$, it can be obtained

$$\begin{aligned}\mathcal{F}\{f(t - a)\} &= \int_{-\infty}^{\infty} f(x) e^{-i\omega(x+a)} dx \\ &= e^{-i\omega a} \int_{-\infty}^{\infty} f(x) e^{-i\omega x} dx = e^{-i\omega a} \hat{f}(\omega).\end{aligned}\tag{3.29}$$

It should be pointed out that a time delay will only change the phase of the Fourier transform and not its magnitude. For example,

$$\sin \omega_0 t = \cos\left(\omega_0 t - \frac{\pi}{2}\right) = \cos \omega_0\left(t - \frac{\pi}{2 \omega_0}\right).\tag{3.30}$$

Thus, if $f(t) = \cos \omega_0 t$, then $\sin \omega_0 t = f(t - a)$ with $a = \frac{\pi}{2} \frac{1}{\omega_0}$. Therefore,

$$\begin{aligned}
 \mathcal{F}\{A \sin \omega_0 t\} &= e^{-i\omega \frac{\pi}{2} \frac{1}{\omega_0}} \mathcal{F}\{A \cos \omega_0 t\} \\
 &= e^{-i\omega \frac{\pi}{2} \frac{1}{\omega_0}} [A\pi \delta(\omega - \omega_0) + A\pi \delta(\omega + \omega_0)] \\
 &= e^{-i\frac{\pi}{2}} A\pi \delta(\omega - \omega_0) + e^{i\frac{\pi}{2}} A\pi \delta(\omega + \omega_0) \\
 &= -iA\pi \delta(\omega - \omega_0) + iA\pi \delta(\omega + \omega_0).
 \end{aligned} \tag{3.31}$$

Frequency Shifting

Assuming that the frequency in $\widehat{f}(\omega)$ is shifted by a constant a , its inverse is multiplied by a factor of e^{iat} . Given that

$$\mathcal{F}^{-1}\{\widehat{f}(\omega - a)\} = \frac{1}{2\pi} \int_{-\infty}^{\infty} \widehat{f}(\omega - a) e^{i\omega t} d\omega \tag{3.32}$$

and by substituting $\varpi = \omega - a$, it follows

$$\mathcal{F}^{-1}\{\widehat{f}(\omega - a)\} = \frac{1}{2\pi} \int_{-\infty}^{\infty} \widehat{f}(\varpi) e^{i(\varpi+a)t} d\varpi = e^{iat} f(t) \tag{3.33}$$

or

$$\widehat{f}(\omega - a) = \mathcal{F}\{e^{iat} f(t)\}. \tag{3.34}$$

To illustrate the effect of frequency shifting, the case when $f(t)$ is multiplied by $\cos \omega_0 t$ is considered. Since $\cos \omega_0 t = \frac{1}{2}(e^{i\omega_0 t} + e^{-i\omega_0 t})$, one can write

$$f(t) \cos \omega_0 t = \frac{1}{2} e^{i\omega_0 t} f(t) + \frac{1}{2} e^{-i\omega_0 t} f(t) \tag{3.35}$$

and accordingly,

$$\begin{aligned}
 \mathcal{F}\{f(t) \cos \omega_0 t\} &= \frac{1}{2} \mathcal{F}\{e^{i\omega_0 t} f(t)\} + \frac{1}{2} \mathcal{F}\{e^{-i\omega_0 t} f(t)\} \\
 &= \frac{1}{2} \widehat{f}(\omega - \omega_0) + \frac{1}{2} \widehat{f}(\omega + \omega_0).
 \end{aligned} \tag{3.36}$$

This process is known as modulation. In other words, when $f(t)$ is modulated by $\cos \omega_0 t$, its frequency is symmetrically shifted up and down by ω_0 .

3.1.5 Convolution

Mathematical Operation of Convolution

The convolution $c(t)$ of two functions $f(t)$ and $g(t)$ is usually written as $f(t) * g(t)$ and is defined as

$$c(t) = \int_{-\infty}^{\infty} f(\tau) g(t - \tau) d\tau = f(t) * g(t). \quad (3.37)$$

The mathematical operation of the convolution consists of the following steps [75, 22]:

- Take the mirror image of $g(\tau)$ to create $g(-\tau)$.
- Shift $g(-\tau)$ by an amount t to get $g(t - \tau)$. In case that t is positive, the shift is to the right, otherwise, it is to the left.
- Multiply the shifted function $g(t - \tau)$ by $f(\tau)$.
- The area under the product of $f(\tau)$ and $g(t - \tau)$ is the value of the convolution at t .

Time Convolution Theorem

The time convolution theorem is defined as

$$\mathcal{F}\{f(t) * g(t)\} = \widehat{f}(\omega) \widehat{g}(\omega). \quad (3.38)$$

By definition,

$$\mathcal{F}\{f(t) * g(t)\} = \int_{-\infty}^{\infty} \left[\int_{-\infty}^{\infty} f(\tau) g(t - \tau) d\tau \right] e^{-i\omega t} dt. \quad (3.39)$$

Interchanging the τ and t , the integration results in

$$\mathcal{F}\{f(t) * g(t)\} = \int_{-\infty}^{\infty} f(\tau) \left[\int_{-\infty}^{\infty} g(t - \tau) e^{-i\omega t} dt \right] d\tau. \quad (3.40)$$

With the following substitution $t - \tau = x$, $t = x + \tau$, $dt = dx$, it can be obtained

$$\begin{aligned} \int_{-\infty}^{\infty} g(t - \tau) e^{-i\omega t} dt &= \int_{-\infty}^{\infty} g(x) e^{-i\omega(x+\tau)} dx \\ &= e^{-i\omega\tau} \int_{-\infty}^{\infty} g(x) e^{-i\omega x} dx = e^{-i\omega\tau} \widehat{g}(\omega). \end{aligned} \quad (3.41)$$

Therefore,

$$\begin{aligned} \mathcal{F}\{f(t) * g(t)\} &= \int_{-\infty}^{\infty} f(\tau) e^{-i\omega\tau} \widehat{g}(\omega) d\tau = \widehat{g}(\omega) \int_{-\infty}^{\infty} f(\tau) e^{-i\omega\tau} d\tau \\ &= \widehat{g}(\omega) \widehat{f}(\omega). \end{aligned} \quad (3.42)$$

Frequency Convolution Theorem

The frequency convolution theorem is given with

$$\mathcal{F}^{-1}\{\widehat{f}(\omega) * \widehat{g}(\omega)\} = 2\pi f(t)g(t). \quad (3.43)$$

The proof of this theorem is also straightforward. By definition,

$$\begin{aligned} \mathcal{F}^{-1}\{\widehat{f}(\omega) * \widehat{g}(\omega)\} &= \frac{1}{2\pi} \int_{-\infty}^{\infty} \left[\int_{-\infty}^{\infty} \widehat{f}(\varpi) \widehat{g}(\omega - \varpi) d\varpi \right] e^{i\omega t} d\omega \\ &= \frac{1}{2\pi} \int_{-\infty}^{\infty} \widehat{f}(\varpi) \left[\int_{-\infty}^{\infty} \widehat{g}(\omega - \varpi) e^{i\omega t} d\omega \right] d\varpi. \end{aligned} \quad (3.44)$$

If $\omega - \varpi = \Omega$, $\omega = \Omega + \varpi$, and $d\omega = d\Omega$, then

$$\begin{aligned} \mathcal{F}^{-1}\{\widehat{f}(\omega) * \widehat{g}(\omega)\} &= \frac{1}{2\pi} \int_{-\infty}^{\infty} \widehat{f}(\varpi) e^{i\varpi t} d\varpi \int_{-\infty}^{\infty} \widehat{g}(\Omega) e^{i\Omega t} d\Omega \\ &= 2\pi f(t)g(t). \end{aligned} \quad (3.45)$$

Clearly, this theorem can also be written as

$$\mathcal{F}\{f(t)g(t)\} = \frac{1}{2\pi} (\widehat{f}(\omega) * \widehat{g}(\omega)). \quad (3.46)$$

3.1.6 The Discrete Fourier Transform

A continuous signal $x(t)$ is defined as a real or complex function of the time t , which is an independent continuous variable. However, the measured signals in the practice are limited in time. More precisely, discrete-time signals arise from either a discrete-signal source or from the sampling of the continuous signals at the discrete times nT_s , where T_s is the sampling frequency and n is a positive integer. The discrete-time signals $x(nT_s)$ are therefore, real or complex functions of a discrete-time variable. The discrete-time signals can also be analyzed or decomposed into a series of sines and cosines.

On the other hand, the signals can also be described by their frequency spectrum, which defines the frequency content of the signal. Here, the Fourier transform is useful in many applications in the engineering. The Fourier transform of the discrete signals is called the Discrete Fourier Transform (DFT) [22, 43, 60] and is defined as

$$X(n\Delta f) = \frac{1}{N} \sum_{k=0}^{N-1} x(kT_s) e^{-j2\pi n \Delta f k T_s} = \frac{1}{N} \sum_{k=0}^{N-1} x(kT_s) e^{-j2\pi nk/N}, \quad (3.47)$$

where $x(n)$ is a discrete signal with length equal to N . This representation is reversible and no information can be lost. The DFT dominates most signal processing strategies, expedites the interpretation of the signals, enlarges the characterization of the systems, and improves the efficiency of the algorithms [69].

Another form of the DFT is the Fast Fourier Transform (FFT) that plays an important role in the simulation of the systems. The FFT is defined in a similar way to the DFT. However, it involves signals of length N that is a power of 2, which means that the FFT can be implemented by employing time-efficient algorithms. When using the FFT to study the frequency-domain characteristics of a signal, there are two limits: 1) the detectability of a small signal in the presence of a larger one; 2) the frequency resolution, which distinguishes two different frequencies.

3.2 Spectral Leakage

In reality, the signals are limited in time and nothing can be known about the signal apart from the measurement interval. For example, if the measurement of an infinite continuous train of sinusoidal wave is of interest, at some point of time the measurement is completed in order to do further analyses. The limit on the time is also posed by the limitations of the measurement system, e.g. buffer size besides other factors. Some expectations have to be made about the signal outside

of the measured interval. The Fourier transform implicitly accounts that the signal substantially repeats itself after the measurement interval. Most of the signals will have discontinuities at the end points of the measurement time. Namely, the FFT assumes that the signal repeats itself and therefore, it will assume discontinuities that are not really there. Figure 3.3 illustrates the scenario in which a continuous train of sinusoidal signal is observed over a finite interval of time (“measured signal”). Here, a sinusoid of 10Hz frequency (10 cycles in 1 second) is sampled with a sampling frequency of 120Hz, see figure 3.3a. In figure 3.3b, the signal for less than 0.45 seconds is observed. As discussed, the FFT assumes the signal to be continuous and it does this by placement of the measured signal repetitively near each other, see figure 3.3c. Observing the discontinuities in the assumed signal, they are manifestations of the measurement time relative to the frequency of the actual signal. If the measurement time is an integral multiple of the rate of the actual signal (i.e. the inverse of the frequency of the signal), then no discontinuities will be observed in the assumed signal. In figure 3.3b, the measurement time is purposefully made to be a non-integral multiple of the actual signal rate. Since sharp discontinuities have broad frequency spectra, these will cause that the frequency spectrum of the signal is spread out. This is called a spectral leakage. As an example, the Fourier transform pair of a finite cosine wave $f(t)$ is to be calculated [75, 22]

$$f(t) = \begin{cases} \cos \omega_0 t & |t| < a, \\ 0 & |t| > a. \end{cases} \quad (3.48)$$

Since

$$\Pi_a(t) = \begin{cases} 1 & |t| < a, \\ 0 & |t| > a, \end{cases} \quad (3.49)$$

the $f(t)$ can be written as

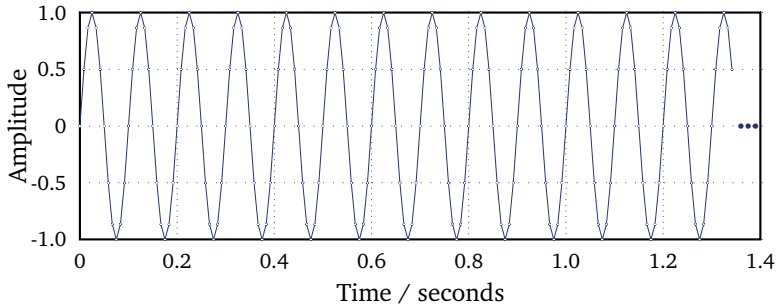
$$f(t) = \cos \omega_0 t \cdot \Pi_a(t). \quad (3.50)$$

The following Fourier pairs will help in the calculation of the Fourier transform of the finite wave train (3.48)

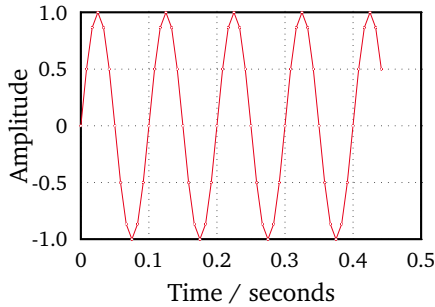
$$\mathcal{F}\{\cos \omega_0 t\} = \pi \delta(\omega + \omega_0) + \pi \delta(\omega - \omega_0) \quad (3.51)$$

and

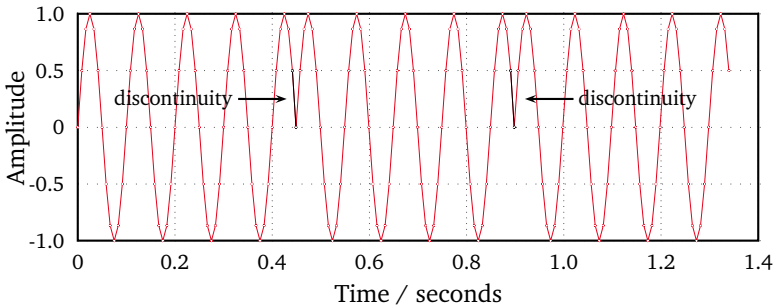
$$\mathcal{F}\{\Pi_a(t)\} = \frac{2 \sin a \omega}{\omega}. \quad (3.52)$$



(a) Actual signal input



(b) Measured interval



(c) Signal assumed by FFT

Figure 3.3.: (a) Actual sinusoid of 10 Hz frequency is sampled with a sampling frequency of 120 Hz. (b) Measured signal for less than 0.45 seconds. (c) The FFT assumes the signal to be continuous by placement of the measured signal repetitively near each other.

According to the convolution theorem, it follows

$$\begin{aligned}
 \mathcal{F}\{f(t)\} &= \frac{1}{2\pi} \mathcal{F}\{\cos \omega_0 t\} * \mathcal{F}\{\Pi_a(t)\} \\
 &= \frac{1}{2\pi} [\pi \delta(\omega + \omega_0) + \pi \delta(\omega - \omega_0)] * \frac{2 \sin a \omega}{\omega} \\
 &= \int_{-\infty}^{\infty} [\delta(\omega' + \omega_0) + \delta(\omega' - \omega_0)] \frac{\sin a(\omega - \omega')}{(\omega - \omega')} d\omega' \\
 &= \frac{\sin a(\omega + \omega_0)}{\omega + \omega_0} + \frac{\sin a(\omega - \omega_0)}{\omega - \omega_0}.
 \end{aligned} \tag{3.53}$$

At the end, it can be noticed that the spectrum is convolved with a cardinal sine function, which leads to a spectral leakage.

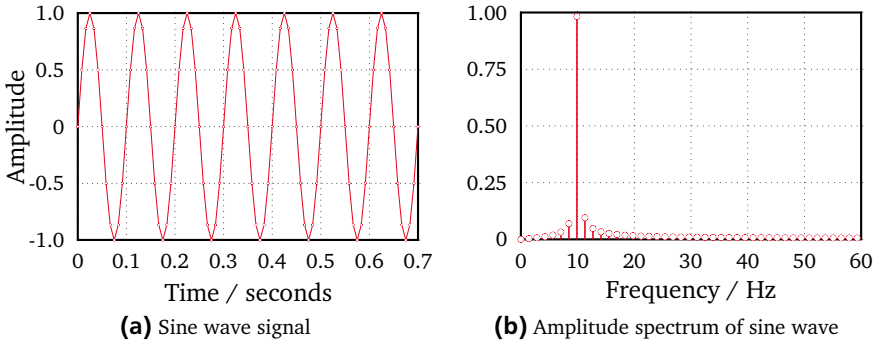


Figure 3.4.: (a) Sinusoidal signal of 10 Hz frequency, which has been measured for 0.7 seconds and sampled with a sampling frequency of 120 Hz. (b) Amplitude spectrum of the sine wave from (a).

In order to visualize the concept of the spectral leakage, the sinusoidal signal in figure 3.4a is observed for 0.7 seconds (7 cycles in total) and afterward, the FFT of the observed signal is performed. Figure 3.4b illustrates the frequency spectrum of the measured signal. Essentially, the frequency spectrum contains a distinct peak at 10 Hz and some spectral leakage because of the limited observation interval. Here, the observation time interval contained an integral number of sinewave cycles, i.e. exactly 7 cycles of the sinusoid in the Time Domain (TD). For the next illustration the measurement time interval is adjusted in such a way that the number of cycles in the observation window is no longer an integer. In figure 3.5a, the signal

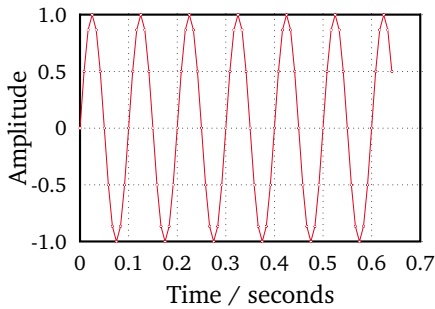
is shrunk and observed for 0.649 seconds, which implies that there are 6.49 cycles and the resulting signal does not end at zero amplitude for $t = 0.649$ seconds. This scenario gives rise to glitches in the signal assumed by the FFT, which constructs a periodic signal from the observed signal. Obviously, more spectral leakage can be observed here when compared to the frequency spectrum in figure 3.4b. The spectral leakage is not due to the FFT, but due to the finite observation time. It gives rise to two problems : 1) the spectral component of the desired signal no longer contains the complete energy. It also contains the energy of the adjacent components and the noise and thereby, it reduces the signal to noise ratio; 2) the spectral leakage from a larger signal component may significantly overshadow other smaller signals, making them difficult to identify or detect.

The effects of spectral leakage may be reduced if the observed signal does not enclose any discontinuity at the end of the measurement time. This scenario rarely occurs in any real application. Another scenario in which the spectral leakage can be reduced is by having a signal that gradually reduces to zero at the ends of the measurement time. All the windows, like Hamming, Hanning, Bartlett, and so on, essentially attempt to do this. Such signal would have no discontinuity when is periodically repeated and will not deteriorate from spectral leakages. Consequently, the windowing techniques are used to lessen the effects of spectral leakage and therefore, the restriction of having a finite measurement interval.

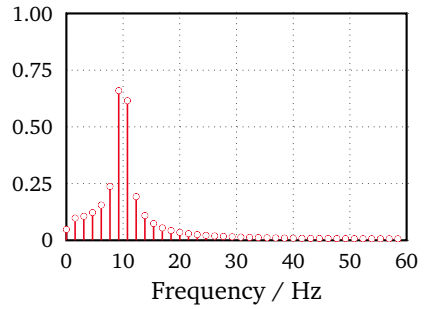
3.3 Windowing

In effect, the process of measuring a signal for a finite time is equivalent to multiplying the signal by a rectangular function of unit amplitude, which lasts for the duration of the measurement time. This way, the signal is measured during a finite measurement time or window, and the rectangular function is called a rectangular window. The effects of spectral leakage can be reduced by decreasing the discontinuities at the end points of the measurement interval. This leads to the idea of multiplying the signal within the measurement time by some function that smoothly reduces the signal to zero at the end points. The process of multiplying the signal data by a function that smoothly approaches to zero at the both ends is referred to as a windowing and the multiplying function is termed as a window function [22, 4, 5]. The effects of a window function can be easily evaluated, i.e. the frequency spectrum of the signal is convolved with the frequency spectrum of the window function.

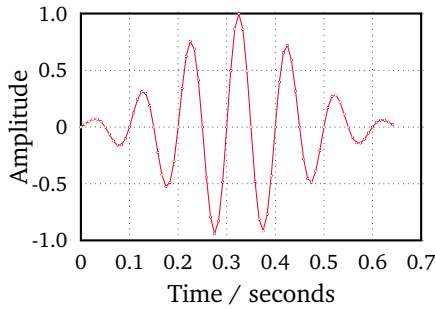
In the special case of the rectangular window, the window function is 1 in the interval and 0 outside the interval. Its Fourier transform is known as the sinc function, or more formally the Dirichlet kernel. Figure 3.5 illustrates the effect of



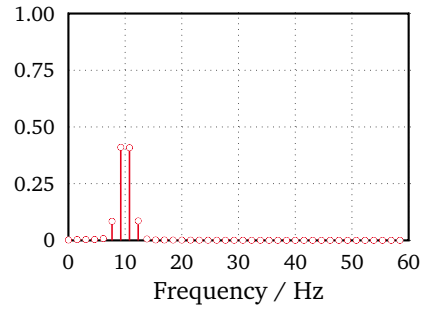
(a) Non-periodic sine wave signal



(b) Amplitude spectrum of a sine wave with leakage



(c) Windowed sine wave signal



(d) Amplitude spectrum of a sine wave showing no leakage

Figure 3.5.: Comparison of a non-periodic sine wave and its amplitude spectrum with leakage to the windowed sine wave and its amplitude spectrum showing no leakage.

applying a Gaussian window to a non-periodic sine tone. Observing the figure 3.5c, it is evident that when a Gaussian window is applied, the leakage present in the amplitude spectrum is reduced (see figure 3.5d). The resulting spectrum is a sharp narrow peak and it should be noticed that it does not have exactly the same shape as the FFT of the original periodic sine wave in figure 3.4b. However, the frequency errors resulting from the spectral leakage are corrected. Finally, the windowing procedure diminishes the effects of spectral leakage in order to better represent the frequency spectrum of the data.

3.4 Parametric Fitting

The Curve Fitting Toolbox from MATLAB [50] provides functions in order to fit curves and surfaces to data. The toolbox performs exploratory data analyses, pre-processes and post-processes data, compares candidate models, and removes outliers. In addition, regression analysis can be conducted, using the provided library of linear and nonlinear models or specifying own custom equations. The library provides optimized solver parameters and starting conditions to improve the quality of the fits. After creating a fit, variety of post-processing methods for plotting, interpolation, and extrapolation can be applied as well as the confidence intervals can be estimated. The process of fitting requires a model that relates the response data to the predictor data using one or more parameters, where as a result the “true” unknown parameters of the model that fit to the data are estimated [25].

3.4.1 Parametric Fit with Library Models

The parametric fit involves finding coefficients (parameters) for one or more models that fit to the data. The data is assumed to be statistical and is divided into deterministic and random component [50]. The deterministic component is given by a parametric model and the random component is often described as error associated with the data (random variations in the data that follow a specific probability distribution, mostly Gaussian). More detailed, the parametric model is a function of the independent (predictor) variable and one or more coefficients having a physical significance.

As explained in section 3.3, the theory dictates the model for determining the eigenfrequencies. Thus, according to figure 3.5d, where the Gaussian peaks describe the eigenmode spectrum, it is obvious that the model should be Gaussian. Therefore, the model to use in the fit is given by

$$Y = a e^{-\frac{(x-b)^2}{c^2}}, \quad (3.54)$$

where the coefficients a , b , and c are estimated by the fit. The toolbox library contains the desired parametric equation (3.54) and at the same time it calculates the optimal default coefficient starting points for the Gaussian model, based on the current data set corresponding to a widened Dirac pulse. Moreover, the library model uses an analytic Jacobian and offers quick convergence [50].

3.4.2 Custom Parametric Fitting

Although the Curve Fitting Toolbox from MATLAB has a wide diversity of curve functions coupled with optimal start points for their coefficients, not all of the desired parametric equations are contained in it. In consequence, the fit of a sinusoidal Gaussian modulated signal needs a custom model, given with the following custom equation that is nonlinear in the parameters

$$Y = a \sin(2\pi b x - \varphi) e^{-\frac{(x-d)^2}{2c^2}}. \quad (3.55)$$

The Curve Fitting Toolbox uses the nonlinear least-squares formulation to fit a nonlinear model to data. Further, Gaussians, ratios of polynomials, and power functions are all nonlinear, defined as equations that might be nonlinear in the coefficients, or a combination of linear and nonlinear in the coefficients. For the custom models, the toolbox chooses unconstrained and random default starting points on the interval $[0, 1]$ and hence, suitable start points for the custom models have to be found. Considering that the custom equation fit uses the nonlinear least-squares fitting procedure, as a result the fit could be less efficient and usually slower than the linear least-squares fitting.

3.4.3 Nonlinear Least Squares

The nonlinear models are given in matrix form by the formula

$$y = f(X, \beta) + \varepsilon, \quad (3.56)$$

where y denotes a vector of responses, f stands for a function of β and X , β is a vector of parameters, X represents a design matrix for the model, and ε is a vector of errors. The fitting process itself uses the method of nonlinear least squares [56, 46], which minimizes the summed squares of the residuals given by

$$S = \sum_{i=1}^n r_i^2 = \sum_{i=1}^n (y_i - \hat{y}_i)^2. \quad (3.57)$$

The residual r_i for the i -th data point is defined as the difference between the observed response value y_i and the fitted response value \hat{y}_i . The number of data points included in the fit is given with n . In case of nonlinear models, the parameters cannot be estimated using simple matrix techniques and these models

are particularly sensitive to the starting points. This leads to a difficult fit and the start points are adjusted because heuristic approaches or random values give the start points for the nonlinear models. Therefore, at the beginning initial reasonable starting value for each parameter is provided. Then, the iterative approach follows some steps until the fit reaches the specified convergence criteria. After a fitted curve for the current set of parameters is produced, an adjustment of the parameters and a determination whether the fit improves or not are done in the next step. The fitted response value \hat{y} is given by $\hat{y} = f(X, \beta)$ and involves the calculation of the Jacobian of $f(X, \beta)$, which is defined as a matrix of partial derivatives taken with respect to the parameters. At the end, the direction and the magnitude of the adjustment of the parameters depends on the long-established and widely-used Levenberg-Marquardt fitting algorithm proposed in [45, 49, 53].

3.5 Time-Domain Approach for Eigenfrequency Extraction

This section provides a brief overview of a precise time-domain approach for eigenfrequency extraction, which is applicable for diverse cavity structures under the assumption of accessible time-domain field responses. In a two-step process, the modeling and the simulation of a specific cavity structure is initially done and afterward, a post-processing of the acquired time-domain responses is conducted. A descriptive sketch of the proposed time-domain approach is given in algorithm 1.

3.5.1 Field Simulation in Time Domain

The cavity of interest is modeled in CST Microwave Studio[®] (CST MWS) [2] and a tiny exciting antenna (as used in a physical model) is put properly such that the modes within a specific frequency range would be excited. Intentionally, the excitation signal applied at the antenna input has a broad bandwidth. A Gaussian-modulated sinusoidal signal is chosen, which certainly covers the range of eigenfrequencies being sought. The time-domain simulation with hexahedral discretization mesh is carried out with the transient solver from CST MWS and it records the electric field intensity at specific field-detection probes placed at various positions inside the cavity. Later, the acquired time-domain signals are used for further post-processing in MATLAB [3], based on fitting techniques with a proposed model of the cavity response, as follows below.

3.5.2 Post-processing of the Time-Domain Computations

In view of the fact that this thesis deals with cavities having superconducting walls, the response of a cavity could stay for a long time as the power losses in the walls are negligible. Theoretically, the response of an ideal-conducting cavity is a Dirac impulse sequence in frequency domain. Nevertheless, due to the limited time interval as well as the finite conductivity and the inserted antenna, the amplitude spectrum of the signal does not contain Dirac delta pulses, but it consists of pulses with finite width. This leads to the idea of artificial windowing by multiplying the original signal within the measurement time interval by a Gaussian function that smoothly reduces the signal to zero at the end points of the measurement time.

As soon as the limitations that come from the finite simulation time or the reduced frequency resolution are overcome, the step from the recorded time-domain to the frequency-domain response is computed using the FFT. The very classical approach in finding eigenfrequencies is to look for local maxima of the frequency spectrum. Consequently, local Gaussian pulses within the spectrum should be located properly. Because the spectrum is only available on discrete sample points with a certain resolution, the characteristic peak value may not be entirely located on such a point, implying that the local maximum is not always the frequency that is sought.

In this direction, the parametric fitting is involved as essential technique for precise determination of the eigenfrequencies and reducing the amount of data required for a given resolution. Relying on the above discussion, a custom Gaussian model is used within the MATLAB Curve Fitting Toolbox, which suits to the specific curve fitting needs. However, following this way there is a restriction to a limited number of samples that can be used, same as the number of samples, which constitute the local Gaussian pulse. Therefore, besides the low values for the Goodness of the Fitting (GoF), the accuracy of the eventual eigenfrequency cannot be high. Additionally, with this approach only the amplitude information of the signal is used, while the phase is completely neglected.

These disadvantages lead to extending the approach in a sense where the phase information of the signal can be also included in a form that is suitable for implementation. Namely, after an initial fit of a local Gaussian pulse in frequency domain, this pulse is selected with a windowing function and an Inverse Fast Fourier Transform (IFFT) is performed. From signal-processing theory it is known that shifting in frequency domain means modulation in TD. So, a Gaussian-modulated sinusoidal signal is expected in time domain and the frequency of the modulation is exactly the frequency that is sought. Consequently, the resulting signal in time domain is fitted with a custom Gaussian-modulated model of the cavity response

and again by finding the optimal model parameters in the least squares sense the true eigenfrequency is determined.

- Require:** a given time-domain signal for the electric field intensity in $P(x, y, z)$
{post-processing and frequency extraction in MATLAB}
- 1: window the signal for the electric field intensity with a Gaussian function
 - 2: perform an Fast Fourier Transform (FFT) of the windowed signal for the electric field intensity
 - 3: calculate the amplitude spectrum from the Fourier data
 - 4: **for all** Gaussian pulses in the amplitude spectrum **do**
 - 5: locate a Gaussian pulse
 - 6: fit the located Gaussian pulse with a Gaussian model and store the GoF1 {Goodness of the Fitting (GoF)}
 - 7: **if** GoF1 > 0 **then**
 - 8: window the Gaussian pulse with a Gaussian function
 - 9: **for all** samples not in the Gaussian pulse **do**
 - 10: set the Fourier data to 0
 - 11: **end for**
 - 12: perform an Inverse Fast Fourier Transform (IFFT) to the shifted Gaussian pulse
 - 13: fit the Gaussian-modulated pulse with a custom Gaussian-modulated model and store the GoF2
 - 14: **if** GoF2 ≈ 100 **then**
 - 15: extract the eigenfrequency from the fitting parameters
 - 16: **end if**
 - 17: **end if**
 - 18: **end for**

Algorithm 1: Sketch of the time-domain approach for an accurate extraction of eigenfrequencies by post-processing the signals of the electric field intensity. The proposed approach uses the advantage that one single time-domain simulation can provide the whole response of an electromagnetic system in a wide frequency band.

The main advantage comparing the proposed approach with the classical approach for finding the peaks is that within this approach the phase information of the signal is additionally used and a parametric fit with all of the data available in the time-domain representation is applied. A more detailed explanation of the approach can be found in [12]. Additionally, the critical implementation points and details are covered, as well as discussed within this thesis in section 5.1.

3.6 Extension of the Time-Domain Approach for Eigenfrequency Extraction

This section addresses an extension of the approach for an accurate eigenfrequency extraction, taken into consideration the evaluated electric field computations in time domain of a superconducting resonant structure. Upon broadband excitation of the cavity, the electric field intensity is recorded at different detection probes inside the cavity. Thereafter, Fourier analysis of multiple recorded signals is performed and by means of fitting techniques with the theoretical response model (in support of the applied excitation) the requested eigenfrequencies are extracted by finding the optimal model parameters in the least squares sense.

In more details, a possible extension to the proposed approach is to take into account post-processing of more than one acquired time-domain response for the analyzed superconducting cavity. Namely, all (or user selected) acquired field computations could be imported in the MATLAB program for further post-processing. After employing an FFT of each signal, a local Gaussian pulse is located within the summed amplitude spectrum using the described technique in [12]. The information for the determined indices of a local Gaussian pulse is then used for the separate fits, where the procedure described above is done for each original response. Finally, the values for the coefficients representing the goodness of the fit are compared and the eigenfrequency determined from the best fit is chosen. In this way, the probability is increased, first, that all of the modes are properly extracted and second, that the resonant frequencies calculated with highest accuracy are selected. At the end, with the additional computational burden the underlying approach is improved in terms of robustness and accuracy. A part of this contribution was published in [13, 14].



4 Eigenvalue Determination in Frequency Domain

In this chapter, a fast approach for an accurate eigenfrequency determination, based on a numerical computation of electromagnetic fields for a superconducting cavity and further employing the Lanczos method for the eigenvalue determination, will be addressed. The major challenges posed by this work will be: first, the ability of the approach to tackle the large-scale eigenvalue problem and second, the capability to extract many, i.e. order of thousands, eigenfrequencies for the considered problem. The first section of this chapter will examine one of the most important classes of methods available for computing eigenvalues and eigenvectors of large matrices. These techniques are based on orthogonal projection methods onto Krylov subspaces, i.e. subspaces spanned by the iterates of the simple power method. What may present to be a trivial expansion of a very slow algorithm, finally shows to be one of the most successful methods for extracting eigen pairs of large matrices, especially in the Hermitian case. Here, the Lanczos algorithm with its variations will be reviewed. In this section, some of the results derived for the generalized eigenvalue problem will be also summarized. Lastly, the Lanczos method with polynomial filtering will be addressed. The filtering methods can be beneficial tools for speeding up the convergence of the standard algorithms for computing eigen pairs. They have had a great success in the past as an aid to accelerate the subspace iteration.

4.1 Basic Lanczos Algorithm

As already stated in the introductory words of the thesis, the main aim of the thesis coincides with solving the electromagnetic problem for a superconducting cavity, which enclosures excited electromagnetic fields. Supposing that the Finite Integration Technique (FIT) will be utilized for the numerical electromagnetic solution, a standard large-scale eigenvalue problem will arise at the end. A detailed steps for the numerical solution using the FIT can be found in section 2.3 on page 15. Afterwards, the following step is to compute the eigenvalues located in a specified interval of a large real symmetric matrix, along with their associated eigenvectors. The interval, which is also referred to as a window, can consist of a subset of the

largest or smallest eigenvalues, in which case the requested eigenvalues are in one of the two ends of the spectrum.

In this direction, an important class of techniques known as Krylov subspace methods extracts approximations from a subspace of the form

$$K_m(\mathbf{A}, \vec{v}) \equiv \text{span}\{\vec{v}, \mathbf{A}\vec{v}, \mathbf{A}^2\vec{v}, \dots, \mathbf{A}^{m-1}\vec{v}\}, \quad (4.1)$$

referred to as a Krylov subspace. The dimension of the subspace increases by one at each step of the approximation process. A few well-known Krylov subspace methods are: the Hermitian Lanczos and the Arnoldi method as well as their variations. The basic Lanczos algorithm was introduced in [42] and since then is known as Lanczos recursion or tridiagonalization, which is used to obtain real scalars λ and the corresponding real-valued vectors $\vec{x} \neq 0$ for a given real $n \times n$ symmetric matrix \mathbf{A} , such that

$$\mathbf{A}\vec{x} = \lambda\vec{x}. \quad (4.2)$$

The main idea of the Lanczos procedure is to replace the eigenvalue problem of the given matrix \mathbf{A} by an eigenvalue problem of a tridiagonal Lanczos matrix \mathbf{T} . This can be achieved by using a three-term recurrence formula. The Lanczos procedure is an orthogonal projection technique onto a Krylov subspace $K_m(\mathbf{A}, \vec{v})$ and can be viewed as a simplification of the Arnoldi method for the particular case when the matrix is Hermitian. A descriptive sketch of the Lanczos algorithm is given in algorithm 2, where \mathbf{A} is an $n \times n$ symmetric matrix. It reduces the matrix \mathbf{A} to a tridiagonal form by means of a three-term recurrence formula. Given an unit-norm initial vector \vec{v}_1 , typically generated randomly, and taking $\beta_1 = 0$, the following recurrence

$$\beta_{j+1}\vec{v}_{j+1} = \mathbf{A}\vec{v}_j - \alpha_j\vec{v}_j - \beta_j\vec{v}_{j-1}, \quad (4.3)$$

where $\alpha_j = \vec{v}_j^* (\mathbf{A}\vec{v}_j - \beta_j\vec{v}_{j-1})$ and $\beta_{j+1} = \|\mathbf{A}\vec{v}_j - \alpha_j\vec{v}_j - \beta_j\vec{v}_{j-1}\|$, generates an orthonormal set of Lanczos vectors, $\mathbf{V} \equiv \{\vec{v}_1, \dots, \vec{v}_j\}$, and a real symmetric tridiagonal matrix \mathbf{T} with diagonal entries $\{\alpha_i\}_{i=1, \dots, j}$ and subdiagonal (superdiagonal) entries $\{\beta_{i+1}\}_{i=1, \dots, j-1}$ defined as

$$\mathbf{T} = \begin{bmatrix} \alpha_1 & \beta_2 & & & & \\ \beta_2 & \alpha_2 & \beta_3 & & & \\ & \beta_3 & \alpha_3 & \ddots & & \\ & & \ddots & \ddots & \beta_j & \\ & & & \beta_j & \alpha_j & \end{bmatrix}. \quad (4.4)$$

```

1:  $\vec{v}_0 \leftarrow 0$ 
2:  $\beta_1 \leftarrow 0$ 
3: for all  $j = 1, 2, \dots$  do
4:    $\vec{v}_{j+1} \leftarrow \mathbf{A} \vec{v}_j - \beta_j \vec{v}_{j-1}$ 
5:    $\alpha_j \leftarrow \langle \vec{v}_j, \vec{v}_{j+1} \rangle$ 
6:   {calculate the Ritz pairs}
7:   {check convergence every tenth iteration}
8:    $\vec{v}_{j+1} \leftarrow \vec{v}_{j+1} - \alpha_j \vec{v}_j$ 
9:   {apply reorthogonalization}
10:   $\beta_{j+1} \leftarrow \|\vec{v}_{j+1}\|$ 
11:  if  $\beta_{j+1} == 0$  then
12:    break
13:  end if
14:   $\vec{v}_{j+1} \leftarrow \vec{v}_{j+1} / \beta_{j+1}$ 
15: end for
16: {compute the Ritz values  $\theta_j$  of  $\mathbf{T}$  and the corresponding Ritz vectors  $\vec{y}_j$ }
17: {compute the approximate eigenvectors  $\mathbf{V} \vec{y}_j$ }

```

Algorithm 2: Basic Lanczos algorithm for the solution of the standard eigenvalue problem 4.2.

If (θ_j, \vec{y}_j) is an eigen-pair of \mathbf{T} , then the Ritz pair $(\theta_j, \mathbf{V} \vec{y}_j)$ will approximate a sought pair of (eigenvalue, eigenvector) for the original problem. Specifically, the extreme eigenvalues are often approximated first. The Lanczos algorithm quickly yields good approximations to extreme eigenvalues of \mathbf{A} while the convergence is often much slower for the interior part of the spectrum. The vectors $\alpha_j \vec{v}_j$ and $\beta_j \vec{v}_{j-1}$ are the orthogonal projections of the vector $\mathbf{A} \vec{v}_j$ onto the last two generated Lanczos vectors \vec{v}_j and \vec{v}_{j-1} , respectively. Thus, the Lanczos process can be seen as an implementation of the modified Gram-Schmidt process, where in every Lanczos iteration the newest Lanczos vector \vec{v}_{j+1} is determined by orthogonalizing the vector $\mathbf{A} \vec{v}_j$ with respect to \vec{v}_j and \vec{v}_{j-1} . Additionally, it can be shown that the vector \vec{v}_{j+1} is zero, and that the following relation holds

$$\mathbf{A}\mathbf{V} - \mathbf{V}\mathbf{T} = \mathbf{0}. \quad (4.5)$$

To conclude, the Lanczos recursion computes a highly-structured (in fact tridiagonal) real symmetric matrix, which can be viewed as computationally optimal matrix and is orthogonally similar to \mathbf{A} . Therefore, the matrices \mathbf{A} and \mathbf{T} must have the

same eigenvalues and moreover, any Ritz vector $\mathbf{V} \vec{y}_j$ obtained from an eigenvector \vec{y}_j of \mathbf{T} is an approximation to a corresponding eigenvector of \mathbf{A} .

There are however numerical problems if only a simple straightforward implementation of this recursion is realized. In general such an implementation yields Lanczos matrices, which have extra eigenvalues in addition to the good eigenvalues being approximations to the eigenvalues of \mathbf{A} . These spurious eigenvalues are result of the losses in the orthogonality of the Lanczos vectors, which in turn are caused by the combination of the roundoff errors resulting from the finite computer arithmetic and the convergence of the eigenvalues of the Lanczos matrix to the eigenvalues of the original matrix \mathbf{A} . A remedy to this problem is to reorthogonalize the vectors when needed. Various reorthogonalization schemes have been proposed in the literature to correct the loss of orthogonality of the Lanczos vectors. Within this thesis, the Lanczos method and its variations, which have been implemented, use the simplest for of reorthogonalization. That is the full reorthogonalization [68], whereby the orthogonality of the current Lanczos vector \vec{v}_j against all previous vectors $\vec{v}_1, \dots, \vec{v}_{j-1}$ is reinstated at each step j . Only for matrices having more than ten million degrees of freedom, the implementation exploits a partial reorthogonalization [71, 66], implying that the reorthogonalization is done only at specific iteration steps.

The convergence of the algorithm is checked in line 7 of algorithm 2. With a given tolerance ϵ , the desired eigenvalues are deemed to have converged at the j iteration if the number of sought eigenvalues of \mathbf{T}_j is the same as the number of eigenvalues of \mathbf{T}_{j-1} and the error of the sought eigenvalues, measured in the relative and average sense, is below the tolerance ϵ .

4.1.1 Lanczos Algorithm with Shift-and-Invert

Along the line of the requirements, the eigenvalue solvers must deal with a variety of issues that are arising in the eigenvalue analysis, i.e. ever-increasing size of matrices and very wide requested frequency range of interest. When the window is well inside the interval containing the spectrum, this is often referred to as an interior eigenvalue problem and the eigenvalues are called interior eigenvalues. To overcome these issues, it is naturally desirable to access the spectrum of the matrix in consecutive parts by utilizing a proper spectral transformation. The motivation of the spectral transformation is to modify the spectral distribution in order to find the eigenvalues more efficiently. Specifically, if the interest is in the eigenvalues around a certain shift σ , shift-and-invert consists of using a Lanczos projection-type method to compute the eigenvalues of the matrix $(\mathbf{A} - \sigma \mathbf{I})^{-1}$. The obtained eigenvalues of this matrix, $\theta_j = (\lambda_j - \sigma)^{-1}$, become the dominant eigenvalues for

those λ_j close to σ and as a result they are easy to compute with the projection method. Finally, the sought eigenvalues are calculated in the form of a transformed eigenvalue

$$\lambda_j = \sigma + 1/\theta_j, \quad (4.6)$$

where σ is the appropriately chosen shift. This transformation enables one to find closely spaced eigenvalues in the neighborhood of σ in a well-separated form. The computational code based on this approach selects a shift dynamically and performs a factorization of the matrix $\mathbf{A} - \sigma \mathbf{I}$.

However, there are a number of situations when the shift-and-invert transformation will be either inappropriate, or too slow to be of feasible significance. For example, it is known that the electromagnetic problems, which are solved based on a hexahedral mesh, will tend to give matrices that are very expensive to factor due to both the computational and the memory requirements. Also, in the situation when a very large number of eigenvalues is to be computed, the number of factorizations to be performed, i.e. the number of shifts necessary to obtain all wanted eigenvalues, can be quite high. Since the cost of each factorization is expensive, the approach will lose its application. Therefore, the focus of this thesis highly leads to combining two significant parts: the Lanczos algorithm on the one hand and the polynomial filtering on the other. Hereby, the emphasis is on the eigen-space rather than the individual eigenvectors. A detailed description of this procedure is given in the next section.

4.2 Lanczos Algorithm with Polynomial Filtering

In this section, a technique that is commonly referred to as polynomial acceleration or filtering technique will be presented. This technique exploits polynomial iterations of the form $\rho(\mathbf{A}) \vec{v}_j$, where ρ is a polynomial being determined from the knowledge on the distribution of the sought eigenvalues of \mathbf{A} . The main goal of the polynomial filtering is to enhance the Lanczos projection scheme by processing the vectors \vec{v}_j , such that their components in the unwanted parts of the spectrum are relatively reduced to those in the wanted parts.

4.2.1 Filtering Technique

For the computation of interior eigen pairs, the Lanczos algorithm with polynomial filtering replaces the matrix-vector product $\mathbf{A} \vec{v}_j$ in the standard Lanczos algorithm by $\rho(\mathbf{A}) \vec{v}_j$, where \mathbf{A} is real symmetric matrix and ρ is a polynomial. The algorithm is sketched in algorithm 3. It should be noted that \mathbf{A} and $\rho(\mathbf{A})$ share the

same eigenvectors, and the matrix $\rho(\mathbf{A})$ has eigenvalues $\rho(\lambda_1), \dots, \rho(\lambda_n)$, where $\lambda_1, \dots, \lambda_n$ are the eigenvalues of \mathbf{A} .

- 1: {determine a polynomial filter $\rho(\lambda)$ with γ such that $\rho(\lambda) \geq \gamma, \lambda \in [\xi, \eta]$ }
- 2: $\vec{v}_0 \leftarrow \mathbf{0}$
- 3: $\beta_1 \leftarrow 0$
- 4: **for all** $j = 1, 2, \dots$ **do**
- 5: $\vec{v}_{j+1} \leftarrow \rho(\mathbf{A}) \vec{v}_j - \beta_j \vec{v}_{j-1}$
- 6: $\alpha_j \leftarrow \langle \vec{v}_j, \vec{v}_{j+1} \rangle$
- 7: {calculate the Ritz pairs}
- 8: {check convergence every tenth iteration}
- 9: $\vec{v}_{j+1} \leftarrow \vec{v}_{j+1} - \alpha_j \vec{v}_j$
- 10: {apply reorthogonalization}
- 11: $\beta_{j+1} \leftarrow \|\vec{v}_{j+1}\|$
- 12: **if** $\beta_{j+1} == 0$ **then**
- 13: **break**
- 14: **end if**
- 15: $\vec{v}_{j+1} \leftarrow \vec{v}_{j+1} / \beta_{j+1}$
- 16: **end for**
- 17: {compute the Ritz values θ_j of \mathbf{T} and the corresponding Ritz vectors \vec{y}_j }
- 18: {compute the approximate eigenvalues $\lambda_j = \langle \vec{y}_j, \mathbf{A} \vec{y}_j \rangle$ }
- 19: {reject all λ_j, \vec{y}_j pairs such that $\lambda_j \notin [\xi, \eta]$ }

Algorithm 3: Lanczos algorithm with polynomial filtering for the solution of the standard eigenvalue problem 4.2. The polynomial filter $\rho(\lambda)$ is expanded in the proper scaled and shifted basis of the Chebyshev polynomials.

A fundamental problem lies in computing an appropriate polynomial ρ in order to approximate a step function that covers the interval of the desired eigenvalues $[\xi, \eta]$. If the polynomial $\rho(\lambda)$ is chosen such that $\rho([\xi, \eta])$ is in an edge region of the spectrum, the eigenvalues of the matrix $\rho(\mathbf{A})$ in $\rho([\xi, \eta])$ will be approximated first. Afterward, the corresponding eigenvectors can be used to extract the eigenvalues of the matrix \mathbf{A} in $[\xi, \eta]$. More precisely, a polynomial, which approximates a step function to cover the interval of the desired eigenvalues $[\xi, \eta]$ can be used. However, a high-degree polynomial approximation to a discontinuous step function will exhibit parasitic oscillations. Therefore, a two-stage process [66, 67] will be adapted. First, a smooth function $\varphi(\lambda)$ similar to the step function in shape is selected and then, a polynomial approximation $\rho(\lambda)$ to this function is applied in the least squares sense. In this work, a middle-pass filter $\varphi(\lambda)$ for the calculation of the interior eigenvalues is considered.

In order to obtain the polynomial approximation $\rho(\lambda)$ to the base filter $\varphi(\lambda)$, a filtered conjugate residual polynomial algorithm [67] will be applied. Here, the functions are expanded in the proper scaled and shifted basis of the Chebyshev polynomials. Thus, all inner product operations as well as the adding and the scaling operations of two expanded polynomials can be easily performed with the expansion coefficients [67]. As a consequence of the 3-term recurrence of the Chebyshev polynomials, the polynomial multiplication by λ can be also easily implemented. The details are omitted and can be found in [66, 67]. Due to the fact that the procedure is performed in a polynomial space, for the standard eigenvalue problem the matrix will never be invoked and therefore, the resulting computing costs will be negligible. For the generalized eigenvalue problem, a solution of subsequent linear system of equations is necessary.

4.3 B-Lanczos Algorithm

Another numerical method that is employed within this work for the solution of the electromagnetic problem for a superconducting cavity is the Finite Element Method (FEM). Supposing that the FEM will be utilized for the numerical electromagnetic solution, a generalized large-scale eigenvalue problem will arise at the end. A detailed steps for the numerical solution using the finite element method can be found in section 2.4 on page 29. Afterward, the following step is to compute extreme and interior eigenvalues of the generalized eigenvalue problem, along with their associated eigenvectors. When addressing a generalized eigenvalue problem,

$$\mathbf{A}\vec{x} = \lambda \mathbf{B}\vec{x}, \quad (4.7)$$

where $\mathbf{A} \in \mathbb{R}^{n \times n}$ and $\mathbf{B} \in \mathbb{R}^{n \times n}$ are symmetric matrices, and \mathbf{B} is positive definite, the symmetry is lost because the algorithm has to work with the matrix $\mathbf{B}^{-1}\mathbf{A}$ or similar expressions such as $(\mathbf{A} - \sigma \mathbf{B})^{-1}\mathbf{B}$ in the case of the shift-and-invert spectral transformation (see section 4.3.1). However, in the case of symmetric positive-definite matrix pairs, the symmetry can be recovered by replacing the standard Hermitian inner product, $\langle \vec{x}, \vec{y} \rangle = \vec{y}^* \vec{x}$, by the B -inner product, $\langle \vec{x}, \vec{y} \rangle_B = \vec{y}^* \mathbf{B} \vec{x}$ [68, 15]. It can be shown that the operator matrix $(\mathbf{B}^{-1}\mathbf{A})$ or $(\mathbf{A} - \sigma \mathbf{B})^{-1}\mathbf{B}$ is self-adjoint with respect to this inner product. When the Lanczos method is applied to the operator $\mathbf{B}^{-1}\mathbf{A}$ for the generalized eigenvalue problem (similarly for $(\mathbf{A} - \sigma \mathbf{B})^{-1}\mathbf{B}$), the Lanczos recursion in (4.3) can be rewritten for a randomly-generated starting vector \vec{v}_1 with $\|\vec{v}_1\|_B = 1$ as

$$\beta_{j+1} \mathbf{B} \vec{v}_{j+1} = \mathbf{A} \vec{v}_j - \alpha_j \mathbf{B} \vec{v}_j - \beta_j \mathbf{B} \vec{v}_{j-1}, \quad (4.8)$$

where

$$\alpha_j \equiv \vec{v}_j^* (\mathbf{A} \vec{v}_j - \beta_j \mathbf{B} \vec{v}_{j-1}) \quad (4.9)$$

and

$$\beta_{j+1} \equiv \left\| \mathbf{B}^{-1} \mathbf{A} \vec{v}_j - \alpha_j \vec{v}_j - \beta_j \vec{v}_{j-1} \right\|_B. \quad (4.10)$$

In this case, the recursion also leads to a tridiagonal reduction of the problem, but the Lanczos vectors are B -orthonormal instead of orthonormal, i.e. $\mathbf{V}^* \mathbf{B} \mathbf{V} = \mathbf{I}$ and for all j , $\left\| \vec{v}_j \right\|_B = \sqrt{\langle \vec{v}_j, \vec{v}_j \rangle_B} = 1$. In the context of algorithm 2, this can be accomplished by doing B -orthogonalization and replacing the 2-norm with a B -norm. A descriptive sketch of the B -Lanczos algorithm without deflation is given in algorithm 4.

- 1: $\vec{v}_0 \leftarrow 0$
- 2: $\beta_1 \leftarrow 0$
- 3: **for all** $j = 1, 2, \dots$ **do**
- 4: $\vec{v}_{j+1} \leftarrow \mathbf{B}^{-1} \mathbf{A} \vec{v}_j - \beta_j \vec{v}_{j-1}$
- 5: $\alpha_j \leftarrow \langle \vec{v}_j, \vec{v}_{j+1} \rangle_B$
- 6: {calculate the Ritz pairs and check convergence every tenth iteration}
- 7: $\vec{v}_{j+1} \leftarrow \vec{v}_{j+1} - \alpha_j \vec{v}_j$
- 8: {apply reorthogonalization}
- 9: $\beta_{j+1} = \left\| \vec{v}_{j+1} \right\|_B$
- 10: **if** $\beta_{j+1} == 0$ **then**
- 11: **break**
- 12: **end if**
- 13: $\vec{v}_{j+1} \leftarrow \vec{v}_{j+1} / \beta_{j+1}$
- 14: **end for**
- 15: {compute the Ritz values θ_j of \mathbf{T} and the corresponding Ritz vectors \vec{y}_j }
- 16: {compute the approximate eigenvectors $\mathbf{V} \vec{y}_j$ }

Algorithm 4: B -Lanczos algorithm without deflation for the solution of the generalized eigenvalue problem 4.7.

4.3.1 B -Lanczos Algorithm with Shift-and-Invert

Although the Finite Integration Technique (FIT) matrices are very big and very expensive to factor due to the computational and the memory requirements, the matrices from the Finite Element Method (FEM) based on curvilinear tetrahedrons are not big. More precisely, by using the FEM implementation introduced in [7],

the matrices with million Degrees of Freedom (DoF) already give very precise results. Therefore, in the situation when a very large number of eigenvalues is to be computed, the number of factorizations to be performed, i.e. the number of shifts necessary to obtain all wanted eigenvalues, is acceptable, since the factorization of the FEM matrices is not computationally demanding. Consequently, an additional interest of this thesis is to employ the B-Lanczos algorithm with shift-and-invert for the eigenvalue determination.

Along the line of the project requirements, the eigenvalue solvers must deal with a variety of issues arising in the eigenvalue analysis, i.e. ever-increasing size of matrices and wide interior frequency range of interest. To overcome these issues, it is naturally desirable to access the spectrum of the matrix in consecutive parts by utilizing a proper spectral transformation. Applying a spectral transformation to the original problem (4.7), such that the eigenvalues near a specified shift σ are calculated first, one gets

$$(\mathbf{A} - \sigma \mathbf{B})^{-1} \mathbf{B} \vec{x} = \theta \vec{x}, \quad (4.11)$$

where the matrix $(\mathbf{A} - \sigma \mathbf{B})^{-1}$ is never explicitly formed. Each block calculation contains 100 eigenvalues and provides information for the successive target value σ . The first time when the B-Lanczos method with shift-and-invert requires an operator multiplication, the solution of linear systems is obtained with the Lower Upper (LU) decomposition followed by the forward-backward substitution. Once the LU decomposition itself is computed, this procedure is repeatedly applied to solve the multiple system of equations with different right-hand side vectors [15].



5 Implementation Details

In this chapter, the implementation details for the approaches, which are proposed in section 3 and 4, will be explained. The critical implementation points and details will be covered as well as discussed within this chapter. Next, in order to verify the applicability of the used approaches, the numerical results, obtained with the time- and the frequency-domain methods, will be compared with the analytical solutions. Specifically, the numerical results will be examined for the analytically resolvable cavities, i.e. the rectangular, the cylindrical, and the spherical cavity. Additionally, the robustness of the both approaches will be investigated here. The chapter is organized as follows: First, the section 5.1 summarizes the above mentioned goals for the case when the time-domain approach is exploited for the eigenvalue calculation. Followed by that, the section 5.2 re-summarizes the same points, but now for the frequency-domain approach.

5.1 Time-Domain Approach

As already stated in the introductory words of the chapter, this section provides a detailed overview of the implementation details for the precise time-domain approach for eigenfrequency extraction, which is applicable for diverse cavity structures under the assumption of accessible time-domain field responses. In a two-step process, the modeling and the transient simulation of a specific cavity structure is initially done and afterward, a post-processing of the acquired time-domain responses is conducted in MATLAB [3]. For that reason, the sections 5.1.1-5.1.4 of this chapter will be concerned with the implementation details for the post-processing of the time-domain responses. Additionally, the accuracy of the time-domain approach for eigenfrequency extraction will be tested for analytically resolvable problems and the results will be stated in the section 5.1.5 of this chapter. Due to verification purposes, rectangular, cylindrical, and spherical resonant structures will be analyzed, whose exact solutions can be analytically evaluated. At the end of this section, the robustness of the proposed time-domain approach will be also examined.

In the simulation studies, it was experienced that for the time-domain field computations, a single personal computer is suited for problems with a moderate number of mesh cells (say, up to several 10^6 mesh cells). To be precise, a computer

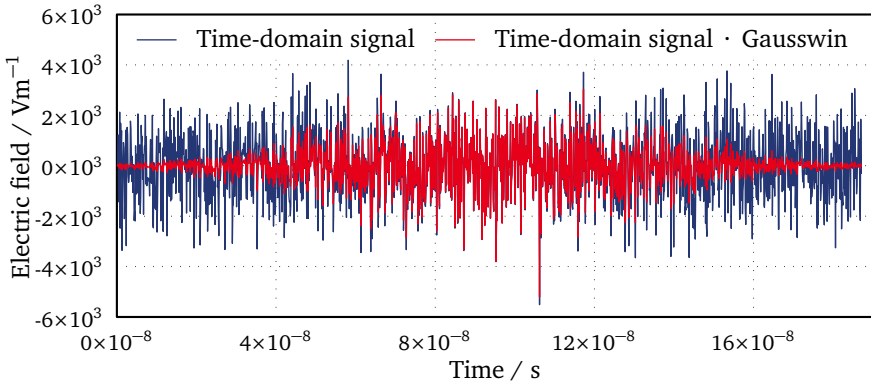


Figure 5.1.: Time-domain response that is acquired from the transient solver in CST Microwave Studio[®] (CST MWS) and its Gaussian windowing. The responses represent the electric field intensity of a superconducting cavity [12].

with a single core Pentium 3 GHz processor and 6 GB Read Access Memory (RAM) memory was used. The same computer configuration was also exploited for the time-domain method for eigenvalue extraction.

5.1.1 Limitations from the Finite Simulation Time

In view of the fact that this thesis deals with cavities having superconducting walls, the time-domain response of a cavity could stay for a long time as the power losses in the walls are negligible. Theoretically, the response of an ideal-conducting cavity is a Dirac impulse sequence in Frequency Domain (FD), i.e. a summation of sinusoidal signals with the associated eigenfrequencies in Time Domain (TD). Nevertheless, due to the limited simulated time interval as well as the finite conductivity and the inserted antenna, the amplitude spectrum of the signal does not contain Dirac delta pulses, but it consists of pulses with finite width (see figure 5.2). That is, the finite simulation time is equivalent to multiplication of the cavity response with a rectangular windowing function of duration $T = N \Delta t$, where Δt denotes the time step, and N is the total number of time samples. Accordingly, the rectangular windowing causes a convolution of the true spectrum with a $\sin f/f$ function in frequency domain [48].

Important issues coming from the limitation in time are the discontinuities at the edges of the measurement time [48]. Given that sharp discontinuities have broad frequency spectra, these will lead to a higher side lobes level and each spectral line

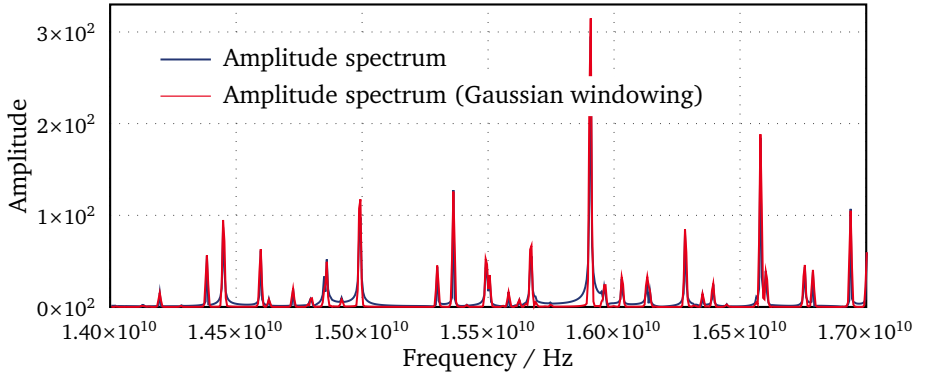


Figure 5.2.: Amplitude spectrum of a time-domain response and a Gaussian windowed time-domain response of a superconducting cavity. Only a part of the amplitude spectrum is illustrated on this figure. As expected, the amplitude spectrum of the Gaussian windowed time-domain response consists of Gaussian pulses that are located on the positions where the eigenfrequencies are [12].

of the frequency spectrum will be spread out in the same way. In other words, the spreading means that the signal energy, which should be concentrated only at one eigenfrequency, leaks instead into other frequencies, the so-called spectral leakage. Consequently, the whole spectrum is distorted and some weak impulses, i.e. eigenfrequencies, can be masked by the resulting convolution with neighboring strong pulses. This leads to the idea of multiplying the original signal within the measurement time by a Gaussian function (cf. figure 5.1) that smoothly reduces the signal to zero at the end points of the measurement time: therefore, avoiding discontinuities overall. The Gaussian windowing function contains the same number of samples N as the original signal. The coefficients of the N -point Gaussian window are computed from the following equation

$$w(n) = e^{-\frac{1}{2}\left(\frac{n}{\sigma N/2}\right)^2}, \quad (5.1)$$

where $-\frac{N}{2} \leq n \leq \frac{N}{2}$ and $\sigma = 0.4$. Since the Fourier transformation of a Gaussian function in TD is also a Gaussian function in frequency domain, then the multiplication with this window leads to a convolution of the spectrum with a Gaussian function. As a result, in case of an ideal cavity, whose spectrum theoretically is constituted of Dirac impulses located at the eigenfrequencies, Gaussian pulses would be expected instead (see figure 5.2).

5.1.2 Fast Fourier Transformation

As soon as the limitations that come from a finite simulation time or reduced frequency resolution are overcome, the step from the recorded time-domain response to the frequency-domain response is computed using the Fast Fourier Transform (FFT), which yields the eigenmode spectrum as a result (cf. figure 5.2).

The very classical approach in finding eigenfrequencies is to look for local maxima of the frequency spectrum. However, this way is not efficient when the interest is in precise determination of the resonant frequencies and has few drawbacks. Firstly, the spectrum is discrete with a certain resolution and the characteristic peak value may not be entirely located on a sample point. The eigenfrequency could be a value that is somewhere in the range between two samples given with the frequency resolution for certain discrete-frequency values (bins), implying that the local maximum is not always the frequency that is sought. Secondly, a more serious focus should be placed that the neighboring modes contribute a certain amount to the total response at the resonance of the mode being analyzed and affect slightly the resonant frequency. To deal with these problems, refined modal extraction methods based on signal processing techniques have been developed.

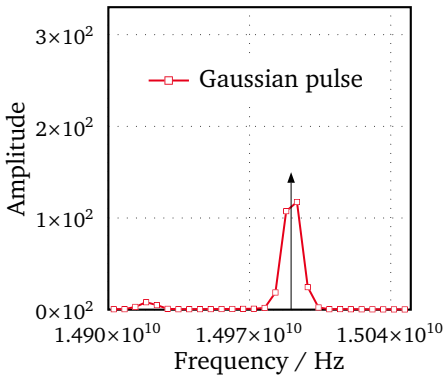


Figure 5.3: Operating signal during the process of eigenfrequency extraction, an isolated Gaussian pulse within the eigenmode spectrum. The Gaussian pulse is constituted of several frequency samples and it is located using the described technique from section 5.1.3. In an ideal case, the Gaussian pulse should be replaced with a Dirac pulse [12].

5.1.3 Technique for Locating a Gaussian Pulse

For further analysis, local Gaussian pulses (see figure 5.3) within the spectrum should be located properly. The location process is divided into several steps. Primarily, a local Gaussian pulse is found as a set of samples with a local maximum. Thereafter, supplementary check is conducted if some other samples might be

added to the right-most/left-most side of the current Gaussian pulse. Namely, if the average amplitude of the succeeding right/left outer triple of samples is less than the average amplitude of the right-most/left-most triple of samples, the outer triple of samples is added appropriately to the right/left part of the Gaussian pulse. After that, the empirical rule for the current located Gaussian pulse, which is constituted from n pairs of frequency and amplitude samples $(f_1, a_{f_1}), (f_2, a_{f_2}), \dots, (f_n, a_{f_n})$, is applied. For this purpose, the standard deviation σ_f for the pulse is estimated and four standard deviations are accounted for the resulting pulse with an appropriate start from the mean value μ_f for the Gaussian pulse. The standard deviation is estimated using the following equation

$$\sigma_f = \sqrt{\frac{\sum_{i=1}^n a_{f_i} (f_i - \mu_f)^2}{\sum_{i=1}^n a_{f_i}}}, \quad (5.2)$$

where a_{f_i} and f_i denote the amplitude and the frequency value for the i -th observed sample, respectively. In the above equation, μ_f is obtained with

$$\mu_f = \frac{\sum_{i=1}^n a_{f_i} f_i}{\sum_{i=1}^n a_{f_i}}. \quad (5.3)$$

At the end, the distance from the both ends of the Gaussian pulse to its maximum is equally adjusted. Concluding with this last step, a final Gaussian pulse is located. Once a local Gaussian pulse is determined, the standard deviation σ_f and the average μ_f for this pulse are calculated for further post-processing analysis.

5.1.4 Fitting Models

By invoking the acquired knowledge of the eigenmode spectrum of the cavity, the fitting model should be nonlinear in the parameters, i.e. a Gaussian nonlinear model should be used to obtain the parameters. In this direction, the parametric fitting is involved as an essential technique for precise determination of eigenfrequencies and reducing the amount of data required for a given resolution. Relying on the above discussion, a Gaussian model is created within the MATLAB Curve Fitting Toolbox, which suits to the specific curve fitting needs, as shown below

$$\text{gauss} = a'_f e^{-\frac{(f-f')^2}{2\sigma_f'^2}}. \quad (5.4)$$

Here, the parameter a'_f represents the maximum value of the curve, f' is the frequency where the peak occurs, and σ'_f controls the width of the Gaussian pulse. The model uses the method of nonlinear least squares together with the trust-region fitting algorithm.

Next, all of the local Gaussian pulses are fitted by employing the Gaussian model and in each fit the values for the found parameters f' and σ'_f are saved. The parameter f' will be used as an initial reasonable start value of the parameters in the further fit, whereas the parameter σ'_f will be included to increase the numerical robustness. Additionally, it should be pointed out that the values of the parameter f' are good candidates for the eigenfrequencies, since they give the position of the maximum value of each Gaussian pulse.

However, following this way there is a restriction to a limited number of samples that can be used, i.e. same as the number of samples, which constitute the local Gaussian pulse. The limitation in the samples causes that the coefficient, which represents the goodness of the fitting, is very low. That means that the accuracy of the eventual eigenfrequency cannot be high. Additionally, with this approach the phase information available from the FFT is completely neglected and only the amplitude information of the signal is used, which is not sufficient for a precise extraction.

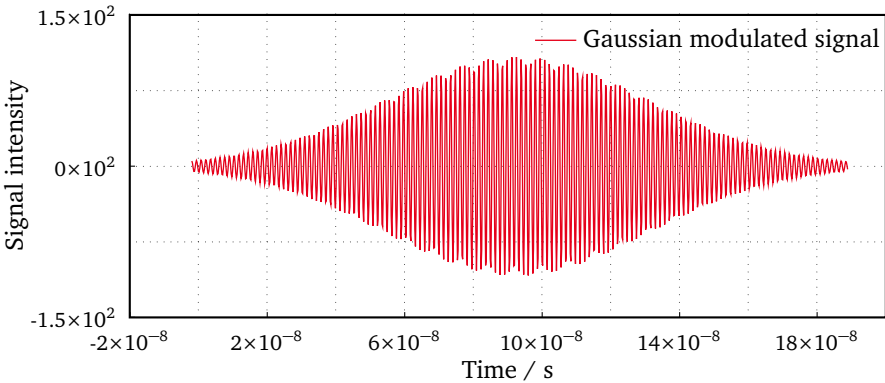


Figure 5.4.: Operating signal during the process of eigenfrequency extraction, Gaussian modulated signal. The signal is obtained when the Inverse Fast Fourier Transform (IFFT) is performed on a shifted Gaussian pulse in frequency domain [12].

These disadvantages lead to extending the approach, in a sense where the phase information of the signal can be also included in a form that is suitable for implementation. Namely, after fitting a local Gaussian pulse in frequency domain the

values of the parameters and the coefficients for the goodness of the fit are obtained. If the goodness of the fit for some Gaussian pulse is not positive, then this pulse is not taken into consideration, which is most probably noise. Otherwise, the local Gaussian pulse is selected. In other words, the samples from the Fourier data that do not belong to the chosen Gaussian pulse are set to zero and the Gaussian pulse is windowed with Gaussian windowing function. Afterward, a step from the frequency-domain data into Time Domain (TD) is performed using the Inverse Fast Fourier Transform (IFFT). From signal processing is known that shifting in frequency domain means modulation in time domain. So, the Gaussian-modulated sinusoidal signal is expected in time domain with the total number of time-domain samples n , same as the number of input samples N (cf. figure 5.4). The frequency of the modulation is exactly the frequency that is sought. Consequently, the resulting signal in TD is fitted with a custom Gaussian modulated model of the cavity response, given with the following equation

$$\text{gaussmodul} = a'_t \sin(2\pi f' t - \varphi') e^{-\frac{(t-t')^2}{2\sigma_t'^2}}, \quad (5.5)$$

where the value for the coefficient a'_t is set to be the maximum value from the Gaussian-modulated sinusoidal signal. Again by finding the optimal model parameters in the least squares sense, the “true” eigenfrequency could be determined with the help of the modulation frequency f' . Therefore, in order to fit with a sinusoidal Gaussian modulated signal, a custom model has been created, which implements the method of nonlinear least squares and uses the Levenberg-Marquardt fitting algorithm.

Parameter	Start point	Lower bound	Upper bound
t'	μ_t	$0.9 * \mu_t$	$1.1 * \mu_t$
f'	μ_f	$\mu_f - \sigma_f$	$\mu_f + \sigma_f$
σ'_t	σ_t	$0.8 * \sigma_t$	$T = t_N$

Table 5.1.: In order the convergence of the fit with the custom Gaussian modulated model (5.5) to be ensured, initial values, lower, and upper bounds for the parameters t' , f' , and σ'_t should be precalculated. This table summarizes the initial values and the bounds that have been used for the above mentioned parameters.

For the most library models, the Curve Fitting Toolbox from MATLAB calculates optimal coefficient starting points. However, when custom models are used, the

toolbox chooses only random starting points between zero and one. Therefore, suitable values as well as bounds for the f' , t' , and σ'_t parameters from the Gaussian modulated model should be precalculated in order the convergence of the fit to be ensured. This work carried out the fitting process with the parameter settings according to table 5.1. The start value for the parameter t' is calculated using a similar estimator like in (5.3). Now, the difference lies in that the response from the IFFT is in time domain and instead of f' , the t' parameter will be present in the estimator

$$\mu_t = \frac{\sum_{i=1}^n a_{t_i} t_i}{\sum_{i=1}^n a_{t_i}}. \quad (5.6)$$

In addition, the parameter t' is bounded as $\mu_t \pm 10\%$. The initial value for the parameter f' is the estimated value from (5.3) and additionally, the lower and upper bounds for this parameter are adjusted with the help of the calculated value in (5.2). That is, the lower and the upper bounds are set as $\mu_f - \sigma_f$ and $\mu_f + \sigma_f$, respectively. In order to select an adequate value of the start point for the parameter σ'_t , an appropriate transformation has been done. Namely, the located Gaussian pulse in FD is shifted to zero and then the IFFT is performed. The purpose of this transformation is to obtain a Gaussian pulse in time domain with its amplitude values \hat{a}_i , but not being modulated. Afterward, the mean value of this pulse $\hat{\mu}_t$ is estimated by using (5.6) and at the same time the obtained value is used in the following equation to approximate the start value for σ'_t

$$\sigma'_t = \sqrt{\frac{\sum_{i=1}^n \hat{a}_i (t_i - \hat{\mu}_t)^2}{\sum_{i=1}^n \hat{a}_i}}. \quad (5.7)$$

The main advantage comparing the proposed approach with the classical one for finding the peaks, is that here the phase information obtained from the FFT is used and a parametric fitting with all of the data available in the time-domain representation is applied. Although, the fitting based only on the amplitude information of the signal results in poor fit, now using the phase information of the signal, very good value for the goodness of the fit can be reached. In this way, as shown in section 5.1.5, a very high accuracy in the eigenfrequency extraction from time-domain computations is gained.

5.1.5 Accuracy of the Time-Domain Approach

The accuracy of the time-domain approach for eigenfrequency extraction is tested for both analytically and non-analytically resolvable problems. Additionally, the proper functionality of the method has been checked during the implementation process. In the numerical tests, several resonators are considered. Namely, due to verification purposes, rectangular, cylindrical, and spherical resonant structures are analyzed, whose exact solution can be analytically evaluated. Firstly, the eigenvalues of the above mentioned resonators are computed from their analytical expressions and following this way, a logarithmic relative error is calculated as

$$\text{relative error} = \log_{10} \frac{|f_{\text{analytical}} - f_{\text{numerical}}|}{f_{\text{analytical}}}, \quad (5.8)$$

by considering the first computed mode eigenfrequency.

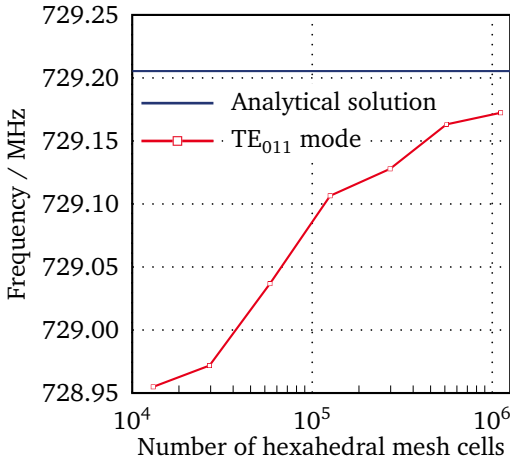


Figure 5.5: Convergence of the resonance frequency for the TE₀₁₁ mode of the rectangular microwave cavity with dimensions $a = 20$ cm, $b = 10$ e cm, and $c = 10 \pi$ cm. The rectangular cavity has been discretized with several hexahedral meshes and the numerical solution is compared to the analytical one.

Rectangular, Cylindrical, and Spherical cavity

As a first experiment, a rectangular cavity with perfectly conducting walls, containing a perfect vacuum, is considered. The degeneracy is broken by making the side lengths different, i.e. rectangular resonator with dimensions $a = 20$ cm, $b = 10$ e cm, and $c = 10 \pi$ cm. The resonance frequency of the rectangular microwave cavity for the TE₀₁₁ mode (the mode with the lowest cutoff frequency for

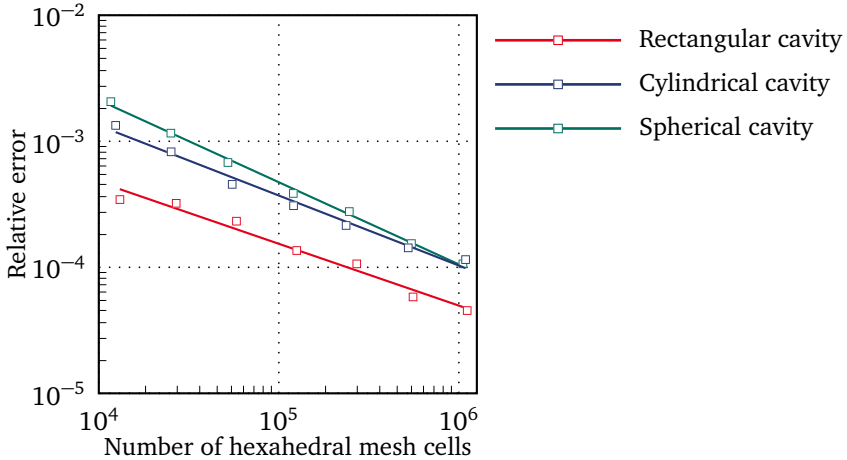


Figure 5.6.: Relative deviation of the numerically obtained values \hat{f} for the lowest eigenfrequency to the analytical result f as a function of the hexahedral mesh cells for a rectangular, cylindrical, and spherical resonator [12].

a rectangular waveguide where $c > b > a$) is found by imposing the boundary conditions on the electromagnetic field expressions in which all of the field components vary sinusoidally at a single frequency [64]. Figure 5.5 illustrates the convergence of the resonance frequency for the TE_{011} mode of the rectangular microwave cavity. Here, the rectangular cavity has been discretized with several hexahedral meshes and the numerical solution is compared to the analytical one.

In addition, the fundamental mode in a cylindrical cavity [65] with radius $R = 20$ cm and length $L = 10\pi$ cm is calculated, too. The cylindrical cavity also has perfectly conducting walls and it is filled with a perfect vacuum. For the analyzed cylindrical cavity, since the L does not fulfill $L > 2.03R$, the TM_{010} mode constitutes the fundamental oscillation. The mode of interest has azimuthal symmetry and the electric field has no longitudinal variation ($\delta E / \delta z = 0$).

Lastly, the first TM_{101} mode of a superconducting spherical resonator with a radius $R = 1$ m is computed from the analytical expressions given in [31] and by employing the root finding algorithm of transcendental equations, which is simply explained in [64].

Specifically, for the time-domain field simulations several different discretization meshes have been used and the convergence study based on the calculation of the

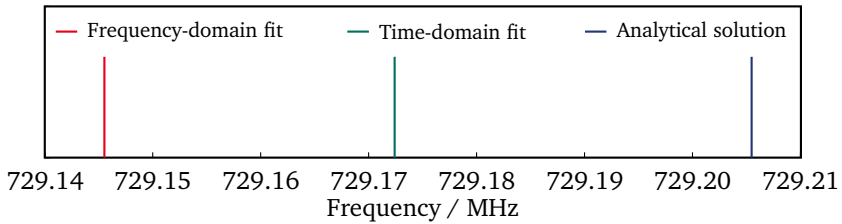


Figure 5.7.: Comparison of the different approaches for calculating the resonance frequency for the TE_{011} mode of the rectangular microwave cavity with dimensions $a = 20$ cm, $b = 10$ e cm, and $c = 10\pi$ cm. The rectangular cavity has been discretized with 1,109,862 hexahedral mesh cells. Here, the analytically calculated eigenfrequency has been compared with the time-domain approach for eigenfrequency extraction, when fitting in time or in frequency domain is used.

relative error, given with (5.8), is shown in figure 5.6. As the number of discretization mesh cells increases, the difference between the analytical and the numerical solutions becomes smaller and absolute error in order of 10^{-4} is present. So, fast convergence is observable and it should be emphasized. Moreover, as suggested by the convergence study, a good accordance of the numerical with the analytical results is evident.

In the next part, the precision of the eigenfrequencies found with a parametric fit in frequency domain and in time domain is compared to the analytical solution for the rectangular cavity. Namely, the resonance frequency for the TE_{011} mode of the rectangular microwave cavity has been analytically calculated and compared in figure 5.7 with the time-domain approach for eigenfrequency extraction, when fitting in time or in frequency domain has been used. On the abscissa is given the frequency in MHz together with the results that are obtained from the different approaches. The first approach for an eigenfrequency calculation, at the left, is the time-domain approach using fitting in frequency domain. Next, the time-domain approach is also demonstrated, but instead fitting in frequency domain now the first mode is calculated using a parametric fit in time domain. At the right of the figure, the analytically calculated frequency for the first mode is shown. As already mentioned above, the eigenfrequencies, which are calculated using the parametric fitting in frequency domain are less accurate than the eigenfrequencies determined with the help of a parametric fit in time domain (cf. figure 5.7). Considering these results for the TE_{011} mode, as well as for all other calculated eigenfrequencies, it can be concluded that using the proposed approach with fitting in frequency

domain can lead to inaccuracy and slightly shifting of the value for the preferable eigenfrequency. Subsequently, the error can be critical for some applications and it should be avoided. At the same time, better agreement between the values for the eigenfrequency found with the proposed time-domain approach using a parametric fit in time domain and the analytical solution is evidently illustrated with the same figure.

5.1.6 Robustness of the Time-Domain Approach

As suggested by the convergence study, shown in figure 5.6, a good agreement of the numerical with the analytical results is evident. The same can be observed in figure 5.8, where the numerically calculated results for a spherical cavity within the specified frequency range are presented and compared to the analytical solution. The radius of the analyzed sphere is $R = 1$ m. On the abscissa the frequencies in an a priori selected frequency band are given, i.e. from 150 up to 450 MHz. The ordinate shows the eigenfrequencies obtained with the time-domain approach using different hexahedral meshes together with the analytical solution. The total time for the transient simulation was set to $3.5 \cdot 10^{-5}$ s, which results in frequency resolution of 30 kHz. Additionally, two post-processing scenarios with one and two probes have been taken into consideration.

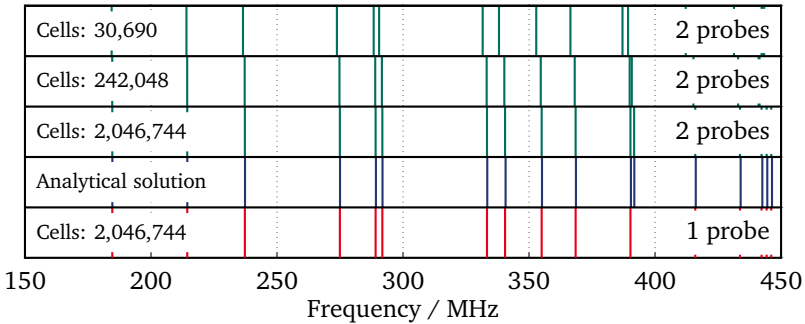


Figure 5.8.: Convergence study showing a comparison between the eigenfrequencies calculated with the proposed time-domain approach (red and green color) and the analytically obtained eigenfrequencies (blue color). The analyzed structure within this study is the spherical cavity with a radius $R = 1$ m. For the time-domain approach three different hexahedral discretization meshes have been used and two post-processing scenarios with one and two probes have been taken into consideration. One frequency around 400 MHz is missing when using only one probe.

The results indicate surely that the number of eigenfrequencies found with the proposed time-domain approach, in the case of two probes being post-processed, coincides with the analytical solutions, i.e. no additional frequency is added or no frequency is missed. In addition, such check was conducted for all of the calculated eigenfrequencies, implying that the serial program implementation has proven to work in a robust and stable fashion under a wide range of circumstances. Nevertheless, observing the same figure, it is obvious that one probe in this case is not enough for robust extraction of all desired eigenfrequencies. Therefore, with the proposed extension of the time-domain approach, as explained in section 3.6, the robustness of the underlying approach is significantly improved. Concerning the accuracy of the obtained data, figure 5.8 suggests slightly shifting of the frequencies in case of coarse meshes. According to figure 5.6, this behavior is expected.

5.2 Frequency-Domain Approach

In this section, a complete overview of the implementation details for the frequency-domain approach is provided. The proposed approach is based on a Finite Integration Technique (FIT) or a higher order Finite Element Method (FEM) computation of the electromagnetic fields for a superconducting cavity. Further, it employs the Lanczos method for the eigenvalue determination. As a result, the method consists of several steps. First, the related geometries are modeled and meshed in CST Microwave Studio[®] (CST MWS) [2]. Afterwards, the corresponding mesh information is passed to the Computational Electromagnetics 3D (CEM3D) solver [7] in order to generate the sparse matrices, which are used as input for the Lanczos eigenvalue solvers. The details for these two steps are presented in section 5.2.1 of this chapter. At the end, the algebraic eigenvalue problems are solved with the help of the Lanczos eigenvalue solvers and their details towards a numerical solution are explained in 5.2.2. It should be noted that the accuracy of the frequency-domain method for eigenfrequency determination is also tested for analytically resolvable problems and the results are discussed in section 5.2.3. In order to verify the approach and to test the implemented code, a spherical cavity is analyzed, whose exact solutions can be analytically evaluated. Moreover, the robustness of the proposed frequency-domain approach is examined in section 5.2.4 of this chapter.

The simulation studies were performed on a computer with a 64 bit architecture, 64 GB of RAM memory, and two quad-core Intel Xeon X5472 processors, clocked at 3 GHz.

5.2.1 Numerical Setup

Within this thesis, the excited electromagnetic fields inside closed resonators are considered, under the assumption of perfectly electric conducting walls. For this purpose, in all simulations the related geometries are first modeled and meshed in CST Microwave Studio[®] (CST MWS) and the corresponding mesh related information is passed to the CEM3D eigenmode solver [7] in order to generate the sparse matrices used as input for the Lanczos eigenvalue solvers. Here, the CEM3D eigenmode solver, developed by W. Ackermann, is used for the matrix pencil generation as well as for the accurate determination of the eigenfrequencies for a given structure. The program is built on the top of the Portable, Extensible Toolkit for Scientific Computation (PETSc) library [10] and it has the capability to run on a distributed memory machine with multiprocessors in parallel.

It is also worth mentioning that the CEM3D program solves the electromagnetic problem either with the Finite Integration Technique (FIT) or with a higher order Finite Element Method (FEM). Respectively, the outcome is either a standard or a generalized eigenvalue problem, derived from the Maxwell's equations for a loss-free and source-free bounded domain with perfectly electric conducting walls on its surface. In case that the FEM has been exploited, then the result is a generalized eigenvalue problem for given real symmetric sparse matrix pencils \mathbf{A} and \mathbf{B} . The user is referred to section 2.4 for more details. On the other side, the FIT leads to a standard eigenvalue problem for a given real symmetric sparse matrix \mathbf{A} . The appropriate derivations when using the FIT can be found in section 2.3. The CEM3D solver implements the Jacobi-Davidson method and determines the eigenvalues of the generalized eigenvalue formulation.

5.2.2 Lanczos Eigenvalue Solvers

Prior to comparing the numerically obtained results by the frequency-domain method with the analytical ones, an additional useful information about the Lanczos solvers settings will be presented. The dedicated Lanczos solvers are implemented in C/C++ and based on the commonly used libraries: Intel Math Kernel Library (MKL) 10.2 / Basic Linear Algebra Subprograms (BLAS) and Linear Algebra Package (LAPACK) for the linear algebra operations and the solution of tridiagonal eigenvalue problem [37], SuperLU [47], and PETSc [10]. The main challenges for the implementation can be itemized as high computational and memory consumptions for the solution of the linear system of equations, supplementary algebraic operations as well as compute- and communication-intensive portions of the codes for the calculation of thousands of (interior) eigenfrequencies. Thus, the implementa-

tion is parallel and exploits all parallelism from a multithreaded and multiprocess implementation of the used libraries [15].

Since the FIT and the FEM matrices are ever-increasing large and sparse matrices, it was essential that the nonzero entries are stored in the most economical manner that minimizes the amount of storage, i.e. the default matrix representation within the PETSc library (Compressed Sparse Row (CSR)) is used. At this point, it should be pointed out that the parallel vectors and the sparse matrices can be easily and efficiently assembled through the mechanisms provided by PETSc. The library enables parallel computing by employing the Message Passing Interface (MPI) standard for all message-passing communication. Analogously, this facilitates computational engineering analyses of unprecedented complexity to be performed. Furthermore, PETSc enables a great deal of runtime control for the user without any additional coding cost. The runtime options include control over the choice of solvers and problem parameters as well as the generation of performance logs.

The Lanczos solvers can be used for the solution of the problems formulated in either the standard or the generalized form. In case of the standard eigenvalue problem $\mathbf{A}\vec{x} = \lambda\vec{x}$, see sections 4.1 and 4.2, the repeated computations of matrix-vector products $\mathbf{A}\vec{x}$ are the only large-scale linear operations. Additionally, three vectors for the three-term recurrence formula are saved, at least if no form of reorthogonalization is used. However, for bigger matrices the implementation exploits partial reorthogonalization [71], which is favored over the full reorthogonalization [68], implying that the reorthogonalization is done only at specific iteration steps.

Similarly to the B-Lanczos eigenvalue solver, the B-Lanczos Shift-and-Invert (SI) solver implements a Lanczos method for the solution of the generalized eigenvalue problem by means of a spectral transformation. In case of the generalized eigenvalue problem (see section 4.3), the repeated computations of matrix-vector products are not the only large-scale operations. More importantly, the B-Lanczos solver requires a solution of a linear system of equations for the positive-definite matrix \mathbf{B} . When extreme eigenvalues are sought, at each B-Lanczos iteration step, an iterative Conjugate Gradient (CG) method (implemented in PETSc) along with Jacobi preconditioner are used for the solution of the resulting linear system of equations. However, for the interior eigenvalue determination, the B-Lanczos solver with spectral transformation requires a solution of an indefinite system of linear equations at every step. Typically, a straight-forward factorization yields factors, which are denser. Therefore, an Lower Upper (LU) factorization followed by the forward-backward substitution was performed using the SuperLU direct solver with reordering the rows and columns of the given matrix, such that sparse factors can

be obtained. Once the LU decomposition itself is computed, this procedure is repeatedly applied to solve the multiple system of equations with different right-hand side vectors.

5.2.3 Accuracy of the Frequency-Domain Approach

The accuracy of the frequency-domain approach for eigenfrequency determination is tested for both analytically and non-analytically resolvable electromagnetic problems. In the following, it is aimed to verification of the frequency-domain approach. Hence, spherical resonant structure is analyzed, whose exact solution can be analytically evaluated. Firstly, the eigenvalues of the above mentioned spherical resonator are computed from their analytical expressions and following this way, a logarithmic relative error is calculated as in (5.8). The first two worst computed degenerated mode eigenfrequencies are considered.

Spherical cavity

According to the above, as a first experiment a spherical cavity with perfectly conducting walls, containing a perfect vacuum, is considered. The radius of the sphere is $R = 1$ m and the maximum error for the modes TM_{101} and TM_{102} is computed from the analytical expressions given in [31] and by employing the root finding algorithm of transcendental equations, which is simply explained in [64].

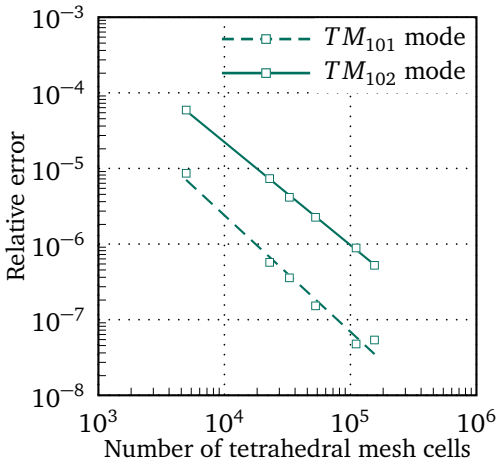


Figure 5.9: Relative deviation (©2014 IEEE) of the analytically obtained values f to the numerical results \hat{f} as a function of the number of tetrahedral mesh cells for a spherical resonator with radius $R = 1$ m. The first two worst computed degenerated mode eigenfrequencies are considered for the spherical cavity [15].

Specifically, for the frequency-domain calculations several different discretization meshes have been used and the convergence study based on the calculation

of a relative error, given with (5.8), is shown in figure 5.9. The desired eigenfrequencies have been calculated by employing the B-Lanczos Shift-and-Invert (SI) solver. As expected, with the increase of the mesh cells, the difference between the analytical and the numerical solutions becomes smaller and relative error in order of 10^{-6} is present. Figure 5.9 clearly demonstrates a fast convergence of 4th order, which can only be obtained with non-planar elements.

5.2.4 Robustness of the Frequency-Domain Approach

In this section the robustness of the frequency-domain approach is examined. Figure 5.10 compares the analytical solution to the numerically calculated results for a spherical cavity within an a priori selected frequency band, i.e. from 120 up to 280 MHz. The cavity has the same characteristics as the one from the previous section. Here, the ordinate shows the eigenfrequencies obtained with the

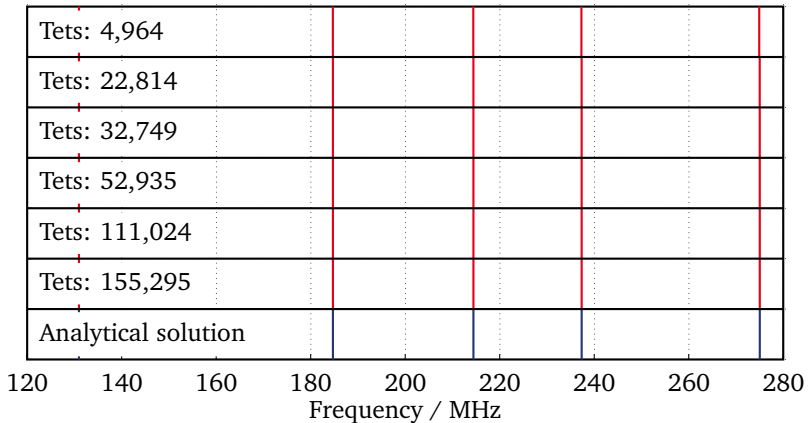



Figure 5.10: Convergence study (©2014 IEEE) showing a comparison between the eigenfrequencies calculated with the proposed frequency-domain approach (red color) and the analytically obtained eigenfrequencies (blue color). The analyzed structure within this study is the spherical cavity from section 5.2.3. For the frequency-domain approach six different tetrahedral discretization meshes have been used [15].

frequency-domain approach using different tetrahedral meshes together with the analytical solution. The results indicate that the number of eigenfrequencies found



with the proposed frequency-domain approach coincides with the reference data. In addition, a good accordance of the numerical with the analytical results is clearly demonstrated with figure 5.9 and figure 5.10, implying that the parallel program implementation has proven to work in a robust and stable fashion. Concerning the accuracy of the obtained data, slightly shifting of the frequencies in case of coarse meshes is probable.

6 Simulation Results

In this chapter, the billiard and the Dirac billiard application example will be examined. The numerical simulations will be performed with the developed codes for the time- and the frequency-domain approaches, which are optimized for the calculation of thousands of eigenfrequencies according to the descriptions in chapter 3 and 4. In addition to the need to ensure a high precision of the calculated eigenfrequencies, the numerical results will be compared side by side with the reference data available from other eigenmode solvers. Here, the simulations have demonstrated high accuracy of the techniques and good agreement with the reference data. Furthermore, the obtained results show that the proposed approaches are competitive in terms of computational time and memory consumptions with other solvers for eigenvalue determination. Finally, all of the results reveal that the suggested techniques based either on fast time-domain field calculations or on direct solutions of large (generalized) eigenvalue formulations can be used for precise extraction of many eigenfrequencies.

Section 6.1 investigates the simulation scenarios together with the obtained comparison results for the billiard cavity. Here, the time- and the frequency-domain approaches have been employed for the calculation of thousand of eigenfrequencies and their results are demonstrated in terms of an accuracy, robustness as well as computational time and memory consumptions. Similar analyses have been carried out for the Dirac billiard cavity and the results are stated in section 6.2. Finally, in order to verify and validate the applicability of the used approaches, the numerical results will be compared with the measurements.

6.1 Application Example: Billiard Cavity

The field of quantum chaos encompasses the study of the manifestations of classical chaos in the properties of the corresponding quantum or more generally, wave-dynamical system (nuclei, atoms, quantum dots, and electromagnetic or acoustic resonators). Prototypes are billiards of arbitrary shape. In its interior a point-like particle moves freely and is reflected specularly at the boundaries. Depending on the shape its properties could exhibit chaotic dynamics. Within this work, quantum billiards are investigated with its statistical eigenvalue properties, which reveal the periodic orbits in the quantum spectra and give the quantum chaotic scattering [26]. Specifically, a microwave resonator with chaotic characteristics is simulated,

see figure 6.1, and the investigations comprise efficient and robust computation of eigenfrequencies that are needed for its level-spacing analysis [27]. Accordingly, the eigenfrequency level-spacing analysis for the determination of the statistical properties requires many (in order of thousands) eigenfrequencies to be calculated and the accurate determination of the eigenfrequencies has a crucial significance. Moreover, considering that the problem is to compute a large number of eigenfrequencies along with their associated eigenvectors, they can be often located in different ranges, i.e. left-most, right-most, or interior portions of the spectrum could be sought.

The requirements for chaotic characteristics are met, for example, by using a superconducting resonator with the shape of a desymmetrized three-dimensional stadium billiard (cf. figure 6.1). The billiard consists of two quarter cylinders with radii $r_1 = 200.0\text{mm}$ and $r_2 = 141.4\text{mm}$, which are rotated with respect to each other by 90° . The billiard is made of niobium that becomes superconducting at temperatures below 9.2K and its classical dynamics are chaotic. In this work, the focus is on the case $r_1 = \sqrt{2}r_2$ since this geometry was studied in the microwave experiments [27, 62], where the ratio is chosen to be irrational in order to avoid non-generic quantum effects due to the classical orbits of measure zero. Specifically, the Institute for Nuclear Physics at Technical University (TU) of Darmstadt studied the classical and the quantum mechanics of a three-dimensional stadium billiard and the spectral properties of a microwave resonator with this shape were investigated experimentally.

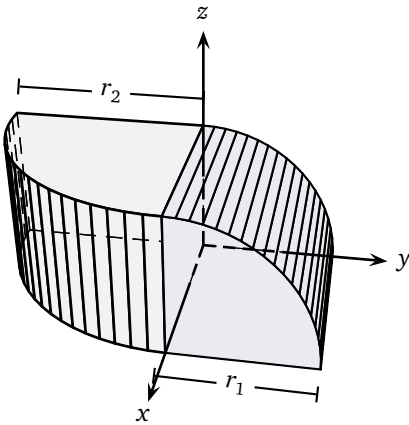


Figure 6.1: Desymmetrized version of the three-dimensional generalized stadium billiard, consisted of two quarter cylinders with radii $r_1 = 200.0\text{mm}$ and $r_2 = 141.4\text{mm}$. The cylinders are rotated with respect to each other by 90° . The billiard is made of niobium that becomes superconducting at temperatures below 9.2K and its classical dynamics are chaotic.

The numerical results for the billiard cavity will be obtained with the time-domain approach as well as the Lanczos solvers for eigenfrequency computation.

For the time-domain field computations, a single personal computer was suited for problems with a moderate number of mesh cells (say, up to several 10^6 cells). More precisely, a computer with 2 quad-core Intel Xeon 3 GHz processors and 64 GB Read Access Memory (RAM) memory was used, unless otherwise stated. The same computer configuration was also exploited for the time- and frequency-domain approaches for eigenvalue computations. On the other hand, a more powerful computer was necessarily used to enable the handling of meshes with more than ten millions of mesh cells. Hence, the larger-scale CST simulations were performed on a modern Graphics Processing Unit (GPU) computer, e.g. 2.00 GHz (quadcore) processor, 32 GB of RAM memory, and 4 nVIDIA Quadro GPUs.

6.1.1 Field Simulation in Time Domain

In this section the fundamental modeling of the analyzed structure will be briefly presented. The cavity of interest is modeled in CST Microwave Studio® (CST MWS) as a free space. A small brick is also modeled as a free space and placed at the top of the cavity. The dimensions of the brick are 50 mm × 50 mm × 50 mm and they are significantly smaller than the dimensions of the cavity. Inside of the brick a small tiny exciting antenna (made of perfect electric conductor) with length of 40 mm, as used in a physical model, is put properly in a way that the modes within a specific frequency range would be excited. The excitation port is modeled as a discrete s-parameter port, which is connected via the antenna to the cavity. Intentionally, the excitation signal applied at the antenna input has a broad bandwidth, i.e. a Gaussian-modulated sinusoidal signal is chosen, which certainly covers the range of eigenfrequencies being sought. The chosen port separation of 10 mm is small compared to the other dimensions of the cavity in order to reduce the port influence on the solution. The background material is modeled as perfect electric conductor whereas the computational domain is terminated by an electric boundary condition. Due to the non-symmetric domain, symmetry planes could not be applied in the calculation, thus there is no reduction of the overall volume to a half or quarter and analogously, no reduction of the computational effort. However, the field simulation with a hexahedral discretization mesh in Time Domain (TD) is carried out with the transient solver from CST MWS, which uses a high degree of parallelization provided with the modern GPUs. Consequently, this feature dramatically accelerates the simulations. During the field simulation, the transient solver detects and records the electric field intensity at specific field detection probes, placed at various positions inside the cavity. Later, the acquired time-domain signals are used for further post-processing in MATLAB, based on fitting techniques with a proposed model of the cavity response, as explained in section 3.5.2. For

stopping the simulation, no check for the accuracy is specified. The simulation is stopped when the specified maximum solver duration is reached. In the following, the procedure for defining the total simulation time is explained.

Manifestation of a spectral distortion occurs as a result of a reduced spectral resolution, which is given with

$$\Delta f = 1/T. \quad (6.1)$$

Namely, this is an important issue and the minimum separation needed between two frequency components must be determined, so that they can be resolved. Relying on the theory for superconducting cavities, the connection between the number of eigenfrequencies n_{freq} and the frequency f GHz is given with the equation

$$n_{freq} = \left(\frac{f}{\alpha}\right)^3, \quad (6.2)$$

where $\alpha = 0.7560$ GHz. So, if the interest is in the calculation of given number of eigenfrequencies, the frequency f can be easily determined and vice versa, if the frequency is known then the number of eigenfrequencies up to that frequency can be computed. The difference between two frequency components is given as reciprocal of the first derivative of n_{freq} for the highest frequency f . In the time-domain approach, the frequency resolution Δf is chosen good enough such that the sought frequency data can be recovered. To be precise, the frequency resolution is selected to be hundred times less than the distance between the two closest eigenfrequencies. This way, about hundred samples between two closest frequency components are available and once the sought frequency resolution Δf is determined, the simulation time is calculated from (6.1). As a result, a large number of simulation time samples might be needed for a reliable characterization of the resonance frequencies of the structure, given that better frequency resolution unescapably requires a longer simulation time. In spite of this, the modern GPUs feature a large number of processing cores and the simulation is speeded up significantly in comparison with a simulation running on a single Central Processing Unit (CPU).

Example. Let's assume that the eigenfrequencies up to 6 GHz are sought. According to (6.2), here are 500 eigenfrequencies to be calculated. The difference between the two closest frequency components is given as reciprocal of the first derivative for $f = 6$ GHz. That is

$$\frac{1}{n'_{freq}} = \frac{\alpha^3}{3f^2} = \frac{1}{250} \text{ GHz} = 4 \text{ MHz}. \quad (6.3)$$

This means that the simulation time of $T = 3.5 \times 10^{-5}$ s (or frequency resolution of $\Delta f = 28.57$ kHz) yields about 140 samples between the two closest frequency components. Consequently, this frequency resolution is good enough to recover the sought frequency data.

6.1.2 Accuracy of the Time- and the Frequency-Domain Approach

Besides the analytically resolvable resonators, the relative error is also measured for the chaotic billiard resonator, which has a clustered eigenvalue distribution [27]. A clustered distribution containing too close eigenfrequencies might cause difficulties in the eigenfrequency extraction. An analytical solution for the billiard cavity is not available and in order to verify the obtained results extremely accurate reference data from Computational Electromagnetics 3D (CEM3D) eigenmode solver are used. Here, CEM3D eigenmode solver is a parallel program [7] for the accurate calculations of eigenfrequencies for a given structure. The billiard structure is modeled and discretized with almost 6 million of curvilinear tetrahedrons in CST MWS and the corresponding mesh is imported to the solver in order to compute the requested eigenfrequency for the analyzed structure. The CEM3D solver employs a Finite Element Method (FEM) formulation by means of higher order curvilinear elements followed by the Jacobi-Davidson method to solve the generalized eigenvalue problem. For this scenario, a target frequency of 2.37 GHz was specified and afterwards, the solver was run in parallel to calculate the sought mode. Within several comparative studies (see section 6.1.4), the CEM3D solver is also used for the generation of the mass and the stiffness matrices of the generalized eigenvalue problem. Then, the Lanczos, Arnoldi, and Krylov-Schur numerical methods are used for the solution of the eigenvalue problem itself.

Relying on an extremely accurate reference solution obtained from CEM3D with almost six million of tetrahedral mesh cells, a logarithmic relative error is calculated for the time- and the frequency-domain approaches as

$$\text{relative error} = \log_{10} \frac{|f_{\text{numerical}} - f_{\text{reference}}|}{f_{\text{reference}}}, \quad (6.4)$$

by considering one computed eigenfrequency, cf. figure 6.2. In particular, for the time-domain field simulations several different hexahedral discretization meshes have been used, while the frequency-domain approach based on the FEM has used a tetrahedral spatial discretization. As the number of discretization mesh cells increases, the convergence study suggests a good accordance of the numerical solutions to the reference data and relative error in order of 10^{-4} for the time-domain

and 10^{-6} for the frequency-domain method is present. Additionally, the figure demonstrates different convergence properties of the methods, i.e. the frequency-domain method, employing a tetrahedral mesh with curvilinear elements for the discretization of the computational domain, indicates higher order convergence and consequently, requires less number of computational grids to obtain the same accuracy [14].

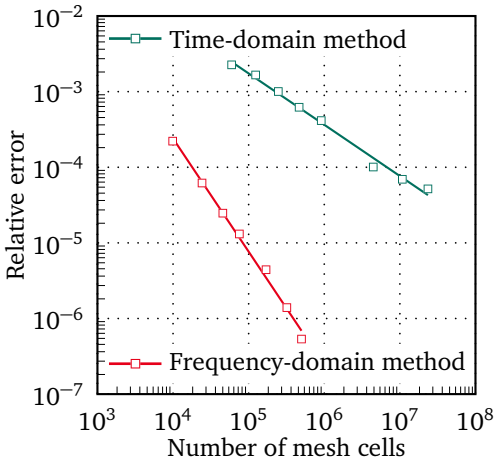
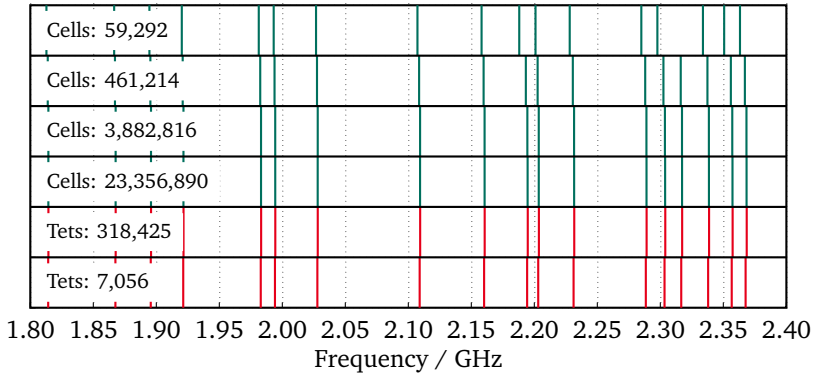


Figure 6.2: Relative deviation (©2013 IEEE) of the numerically obtained values \hat{f} to the reference results f as a function of the mesh cells for a billiard resonator. The mode oscillating at 2.37GHz is determined. The time-domain approach is based on the FIT with hexahedral mesh, whereas the frequency-domain approach takes advantage of the FEM with higher order curvilinear elements [14].

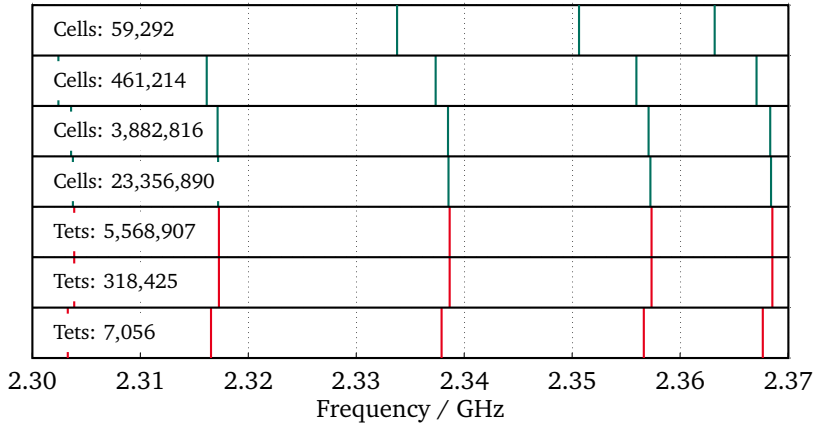
6.1.3 Robustness of the Time- and the Frequency-Domain Approach

In figure 6.3a, a part of the results for the billiard cavity that are found with the time- and the frequency-domain approach using the B-Lanczos solver with shift-and-invert are compared. On the abscissa are given the frequencies in an a priori selected frequency band, i.e. from 1.8 up to 2.4GHz. The ordinate shows the eigenfrequencies obtained with the time-domain approach using four different discretization meshes, and the data calculated using a field simulation in Frequency Domain (FD) with two different tetrahedral meshes. The total time for the transient simulations has been adjusted to 3.5×10^{-5} s, which results in a frequency resolution of 28.57 kHz that is good enough to recover the sought frequency data.

Concerning the accuracy of the obtained data, slightly shifting of the frequencies can be observed in case of coarse meshes. As the number of mesh cells increases, a good agreement with the reference data is clearly observed. For this purpose, a part of figure 6.3a is enlarged and shown in figure 6.3b. Furthermore, in figure 6.3b an additional row is added representing extremely accurate reference



(a) Frequencies in an a priori selected frequency band, i.e. from 1.8 up to 2.4 GHz



(b) Frequencies in an a priori selected frequency band, i.e. from 2.30 up to 2.37 GHz

Figure 6.3.: Convergence study showing a comparison between the eigenfrequencies calculated with the proposed time-domain approach (green color) and the eigenfrequencies obtained with the B-Lanczos shift-and-invert eigenmode solver (red color). For the time-domain approach four different hexahedral discretization meshes are used. At the same time, the frequency-domain solver exploited three different tetrahedral discretization meshes.

data for the eigenvalues in the range $[2.30, 2.37]$ GHz. Unfortunately, for this shape of resonator an analytical solution for the electromagnetic problem is not

available and in order to verify the obtained results, the reference data from the CEM3D eigenmode solver are used. Therefore, the structures are modeled and meshed with almost 6 million of curvilinear tetrahedrons and the corresponding meshes are imported to the CEM3D eigenvalue solver in order to compute the requested eigenfrequencies for the analyzed structure. These results were also used in the previous section for the calculation of the logarithmic relative error for the mode oscillating at 2.37 GHz. According to figure 6.3b, in case of fine meshes a good agreement of the time-domain results with the frequency-domain data can be obtained.

The results in figure 6.3a and 6.3b indicate that when fine mesh is used the number of eigenfrequencies found with the both approaches is exactly the same, i.e. no additional frequency is added or no frequency is missed. In addition, such check was also conducted for around 900 calculated eigenfrequencies, where the theoretical connection for the number of eigenfrequencies up to a specific frequency given with (6.2) is used. The results are presented in figure 6.4 showing the frequency over the mode index for the theoretical (blue dots) and the calculated connection (red dots). The curves agree well, which means that the proposed approaches lead to a robust eigenfrequency extraction.

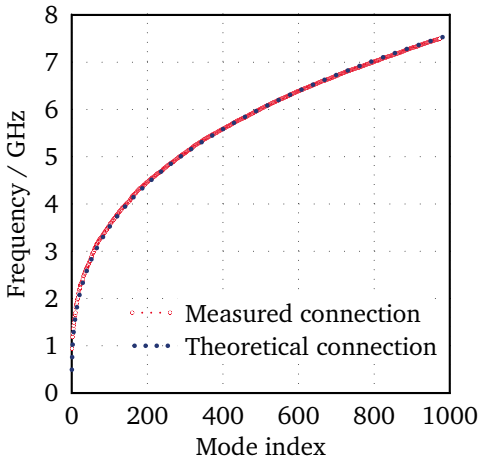


Figure 6.4: Theoretical and measured connection between the number of modes and the frequency. The theoretical connection has been calculated using the equation (6.2). For the measured connection, about 900 eigenfrequencies up to 7 GHz have been extracted for the billiard cavity structure by employing the time-domain approach.

Post-processing of Several Field Probes

In figure 6.5, a part of the results found with the time-domain approach is compared to the reference data calculated with the CEM3D eigenvalue solver. On the abscissa are given the frequencies in an a priori selected frequency band,

i.e. from 1.5 up to 2.0GHz. The ordinate shows the eigenfrequencies obtained from the time-domain approach with 57,096 hexahedra next to the reference data calculated using a field simulation in FD with tetrahedral mesh containing 122,690 tetrahedrons. The total time for the transient simulation was set to 3.5e-05 s, which results in a frequency resolution of 30 kHz. Two post-processing scenarios with one and two probes have been taken into consideration [14].

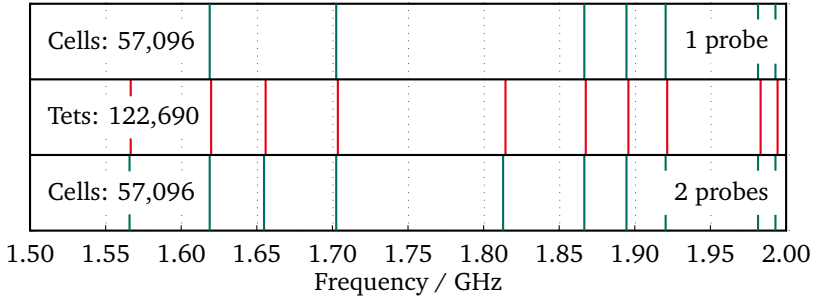


Figure 6.5.: Convergence study (©2013 IEEE) showing a comparison between the eigenfrequencies calculated with the proposed time-domain approach (green color) and the reference eigenfrequencies obtained with the CEM3D eigenmode solver based on higher order curvilinear elements (red color). For the time-domain approach a hexahedral discretization mesh is used. At the same time, the reference data are obtained using a tetrahedral discretization mesh [14].

Figure 6.5 clearly indicates that in the case of two probes being post-processed the number of eigenfrequencies found with the proposed time-domain approach coincides with the reference data, i.e. no additional frequency is added or no frequency is missed. Evidently, one probe in this case is not enough for robust extraction of all the desired eigenfrequencies. Concerning the accuracy of the obtained data, slightly shifting of the frequencies can be observed because of the different convergence properties for the applied methods (cf. figure 6.2).

6.1.4 Performance Analysis

The frequency-domain approach, described in section 4.3, is applied in agreement with the requirements of thousands of precisely calculated eigenfrequencies for the billiard cavity structure. An example mesh for this cavity configuration has 187,984 tetrahedral elements, resulting in matrices **A** and **B** with $n = 1,163,238$ Degrees of Freedom (DoF) and $\text{nnz} = 49,495,452$ nonzero elements. The sparsity

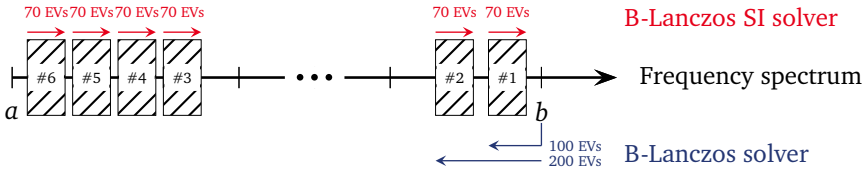


Figure 6.6.: Graphical representation of the different requested eigen ranges with their dimension. $[a, b]$ presents the full eigen range. Six distinct scenarios are illustrated.

Simulation	#3	#4	#5	#6
Time (hours)	9.26	6.82	7.19	7.21

Table 6.1.: Time consumption for the determination of 70 eigenfrequencies for the billiard cavity. The simulations #3 - #6 are demonstrated, where the B-Lanczos solver with shift-and-invert was exploited for the eigenvalue calculation.

information of the matrices is $\frac{nnz}{n} = 42.55$ and the full eigen range is $[0, 3.64 \text{e}+4]$. Subsequently, model runs were performed for six simulation scenarios, denoted with #1, #2, to #6 and in each of the scenarios different eigen ranges with dimension of 70 eigenfrequencies were requested (see figure 6.6).

The performance analysis of the B-Lanczos and the B-Lanczos Shift-and-Invert (SI) eigenvalue solvers were conducted in terms of memory, CPU time, and number of iterations. The specified accuracy of the solvers was set to 10^{-12} and the same was reached. In the simulations #1 and #2, both of the B-Lanczos implementations were used to calculate the sought eigenfrequencies. For the other simulations only the B-Lanczos SI was used, since the eigen ranges were quite inside in the eigen-spectrum.

Figure 6.7 compares the B-Lanczos iterations and the memory consumptions of the B-Lanczos solver to the iterations and the consumptions of the B-Lanczos SI solver, whereas figure 6.8 and table 6.1 show the time consumptions for the different simulations and methods. Here, the total CPU time is given as a sum of the Central Processing Unit (CPU) time that was used for solving linear system of equations, matrix-vector products, reorthogonalization, and other time (e.g. time needed to calculate the eigenvectors, to read the input matrices, etc.). Evidently, the largest part of the computational time is required for the solution of system of linear equations.

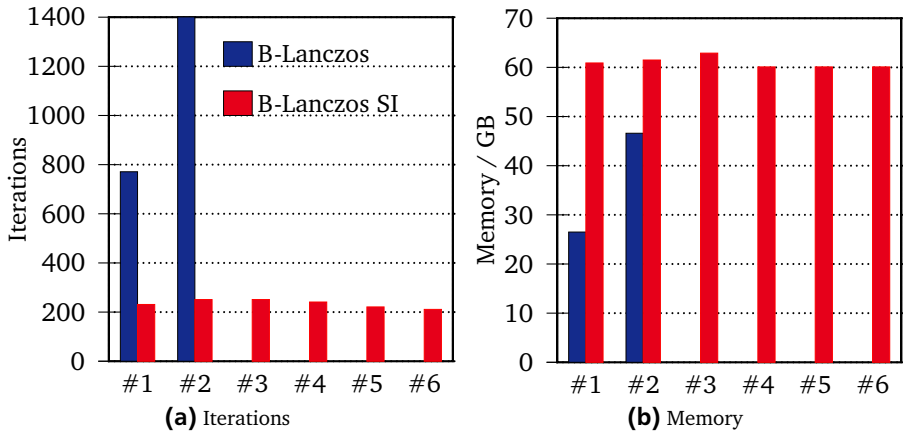
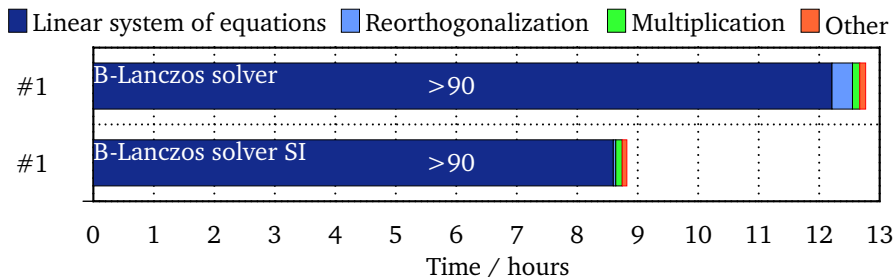


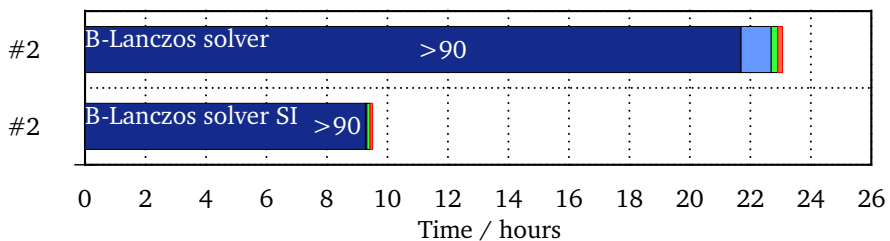
Figure 6.7.: Number of iterations and memory consumptions for the determination of 70 eigenfrequencies for the billiard cavity. The results are shown for six different simulations, where for the first two, the B-Lanczos solver is compared to the B-Lanczos solver with shift-and-invert.

As suggested by the charts, the commonly used performance parameters for the B-Lanczos SI solver indicate a similar behavior in all the simulations. On a contrary, the CPU time and the memory resources, utilized by the B-Lanczos solver, grow linearly as the eigen range is shifted more inside. Therefore, the B-Lanczos solver has limited application when interior eigenvalues are sought. Besides the regions with closely spaced eigenvalues, the convergence of the B-Lanczos solver with shift-and-invert is very fast, because of its good separation properties. Consequently, the number of necessary iterations, as well as, the CPU time resources until eigenvalue convergence is rather smaller when compared to the B-Lanczos solver. Additionally, figure 6.9 plots the convergence error of the B-Lanczos and the B-Lanczos SI solver during the simulation #1, i.e. the error is plotted at the every 10-th iteration step. It should be mentioned that the B-Lanczos solver has to calculate additional 30 largest eigenfrequencies in order the requested 70 eigenfrequencies to be reached. This causes almost 800 B-Lanczos iterations. On another side, the B-Lanczos shift-and-invert solver leads to convergence in less than 300 iterations and hence, it can be fully recommended in case of enough available computational resources.

Moreover, the performance of the B-Lanczos shift-and-invert solver was tested for FEM matrices having different degrees of freedom when 100 eigenfrequencies are sought. The numerical results performed so far tend to show that the resulting



(a) Time consumption for the simulation #1



(b) Time consumption for the simulation #2

Figure 6.8.: Time consumption for the determination of 70 eigenfrequencies for the billiard cavity. Simulations #1 and #2 are demonstrated and the B-Lanczos solver is compared to the B-Lanczos solver with shift-and-invert. The total CPU time is given as sum of the CPU time that was used for solving the linear system of equations, the matrix-vector products, the reorthogonalization, and the other time.

algorithm scales nonlinearly with the system size. These results are presented in the next section and at the same time they are compared with the time-domain approach as well as other eigenvalue solvers.

6.1.5 Comparison with Other Eigenvalue Solvers

In the present work, the effort is focused on the time-domain computations for electromagnetic problems as well as the frequency-domain approaches. When the FEM is formulated in FD, employing a tetrahedral mesh with curvilinear elements [6] to discretize the problem, one ends up with the numerical solution of the generalized large-scale eigenvalue problem. Hereby, numerical methods, as Arnoldi,

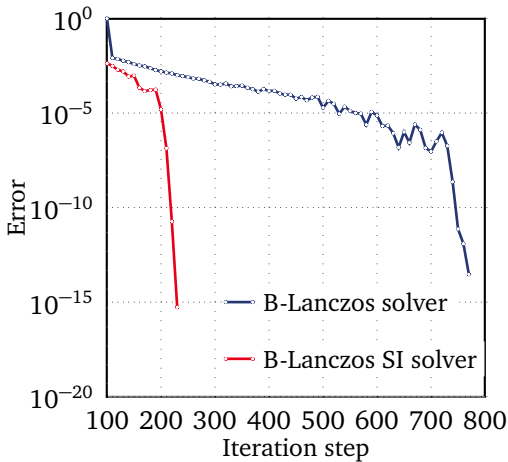


Figure 6.9: Convergence rate of the B-Lanczos and the B-Lanczos with shift-and-invert solver for the eigencomputations in simulation #1. The matrix pencils have 1,163,238 DoF and the error is plotted at the every 10-th iteration step. The convergence of the B-Lanczos solver with shift-and-invert is very fast. The B-Lanczos solver calculates additional 30 large-most eigenfrequencies in order the requested 70 eigenfrequencies to be reached.

Lanczos, and Krylov-Schur method, are applied to the computation of the desired eigenfrequencies.

In order to compare the computational speed as well the memory consumption issues of the time-domain approach and the Lanczos solvers, the recent versions of Matlab, Scalable Library for Eigenvalue Problem Computations (SLEPc), and CEM3D are chosen. The results are plotted in figure 6.10. Each simulation computes the largest 100 eigenvalues of a billiard cavity with an accuracy of 10^{-12} . The computer resources limit the availability of the results, which are extractable with the different eigenvalue solvers. The eigenvalues in MATLAB are obtained employing the Arnoldi's method implementation, while in SLEPc the Krylov-Schur method was used in combination with Jacobi preconditioner of the Conjugate Gradient (CG) method and the Generalized Minimal RESidual method (GMRES). Also, two different setups for the SLEPc simulations with CG method are analyzed, where the difference is in the dimension of the subspace, 200 or 500 B-Lanczos vectors were selected. Dependent on the user's input, the SLEPc library gives largely different outcomes.

As depicted in figure 6.10, the iterative solvers, which are part of the frequency-domain methods, need long simulation time, but less memory, as to be expected. Here, the B-Lanczos solver next to SLEPc can be considered as one group. On another side, the B-Lanczos solver with shift-and-invert and Matlab are clearly separated from the other solvers in time consuming sense. Therefore, the B-Lanczos solver with shift-and-invert or Matlab can be recommended in a case

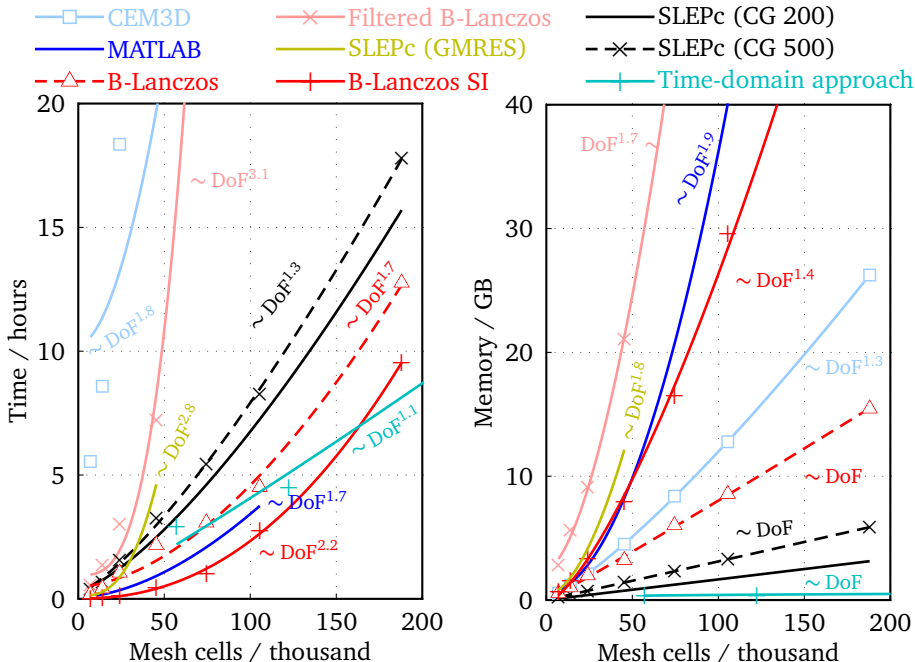


Figure 6.10.: Computational time (left) and memory consumptions (right) of selected eigenvalue solvers for the determination of 100 large-most eigenvalues (©2013 IEEE). Different number of curvilinear tetrahedral and hexahedral discretization meshes for the billiard cavity are used within the frequency- and the time-domain methods, respectively [14].

that enough computational resources are provided. However, it should be noted that these solvers require more memory than the other solvers. Especially, CEM3D, SLEPc with Conjugate Gradient (CG), and the B-Lanczos solver have a very good characteristic from memory usage point of view, where a linear behavior is observed [14, 15].

When compared to all other methods, the memory usage of the time-domain method remains low even with a dramatical rise of the problem size, making this method as a proper choice when the computational resources are limited. According to figure 6.2, if a higher accuracy is desired, i.e. relative error less than 10^{-3} , the time-domain approach would require a higher mesh resolution, which can finally result in a longer simulation time compared to the frequency-domain approach. In

such situations, the advantages of a high degree of parallelization provided with the GPUs can be used to accelerate the simulations considerably [14].

6.1.6 Scalability

As explained in section 5.2.2, the Lanczos solvers are built on the top of the Portable, Extensible Toolkit for Scientific Computation (PETSc) library and they have the capability to run on a distributed memory machine with multiprocessors in parallel. With the intention of obtaining insights in the developed code (scalability and performance), the scalability characteristics of the Lanczos solver with polynomial filtering are briefly examined within this section. For this purpose, the eigenvalue calculations of the billiard cavity are used.

Strong Scaling

The performance measurements have been conducted for the calculation of 615 smallest eigenvalues of the billiard cavity, which has been discretized with hexahedral meshes having 3, 407, 398 and 6, 632, 645 elements. The employed Lanczos solver with polynomial filtering covers at least 615 iteration steps in order to calculate the sought eigenfrequencies. The work definition for the numerical tests includes the parallel portion of the code, the communication as well as the serial part of the program. Precisely, the serial part is limited to the startup, the initialization, and finally, the process of writing the results. In order to quantify how much of the computational time for the different problems is reduced with the increase of the resources, strong scaling tests are performed. Typically, a program shows good scalability if, partitioned over more and more processors, it demonstrates perfect or near perfect speedup.

The computations are performed on the TEMFCL1000 and the TEMFCL2000 computer cluster, owned by the Computational Electromagnetics Laboratory (TEMF) at TU Darmstadt. According to the characteristics summarized in table. 6.2, the cluster TEMFCL1000 has 60 nodes, each node has 2 Intel(R) Xeon(R) processors clocked at 2 GHz, and each processor possesses 4 cores. The nodes are connected with a gigabit ethernet network and each node has 16 GB of available working memory. During the simulations, the numerical tests have been performed on up to 200 cores and the hyper-threading option on the computer cluster has been switched off. Taking the simulation on 48 cores as a reference data from which the strong scalability is judged, figures 6.11a and 6.11b present the speedup and the efficiency curves obtained on the TEMFCL1000 cluster for the two tested problems.

On the other side, the cluster TEMFCL2000 is more powerful (see table. 6.2) and has 172 nodes, where each node has 2 Intel Xeon X5650 processors with 12

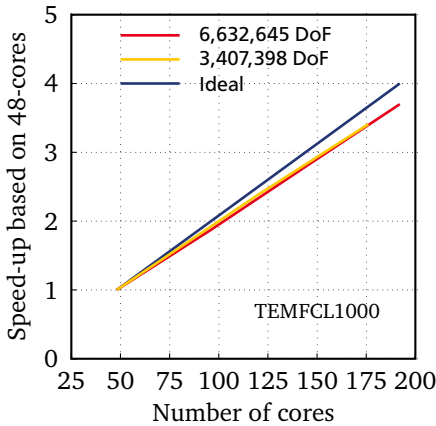
	TEMFCL1000	TEMFCL2000
System	Windows Server 2008 R2 HPC	Windows Server 2008 R2 HPC
Size	60 nodes	172 nodes
Node	8 cores 16 GB of RAM memory	12 cores 24 GB of RAM memory
Core	Intel(R) Xeon(R) E5335 2.0 GHz	Intel Xeon X5650 3.0 GHz
Network	DDR-Infiniband-Lanes	QDR-Infiniband-Lanes

Table 6.2.: Characteristics for the computer clusters TEMFCL1000 and TEMFCL2000, which are owned by the Computational Electromagnetics Laboratory (TEMF) at the Technical University (TU) of Darmstadt.

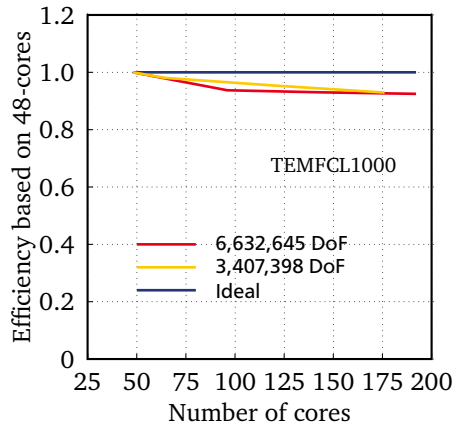
cores. The available working memory for each node is 24GB and the nodes are connected with an infiniband (QDR), gigabit ethernet, and IPMI-network. During the simulations, the hyper-threading was also switched off on this cluster. Here, the test for the fine grid is repeated and 96 cores are used as the baseline from which the strong scalability is judged. These results are demonstrated in figures 6.11c and 6.11d.

As expected, the problems have a good scalability because of the low communication-to-computation ratio. For the TEMFCL1000 cluster, the coarse and the fine grid does not saturate up to the accounted number of 200 cores and the parallel efficiency, defined in [34], stays at 90%. Additionally, this is observed for the TEMFCL2000 cluster as well, where the overall increased node communication produces only lower deviations from the ideal speedup, as the communication-to-computation ratio remains low. Due to the sufficient memory on a single core, the usage of more processors explains the superlinear speedup and efficiency that can be noticed here (see figures 6.11c and 6.11d).

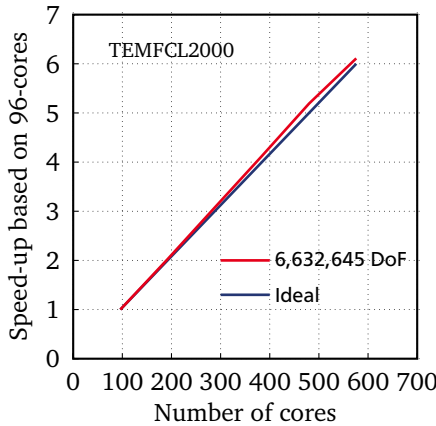
A general conclusion for the strong code scalability can be drawn based on the results for the above analyzed tests, where the comparison with the ideal speedup shows only minor differences. Finally, the code attains a good scalability on the typical high-performance clusters and it can be reached up to the six hundred accounted cores. As depicted in figure 6.11c, the speedup does not noticeably decrease from the optimal, meaning that this problem scales up to minimum 600 cores.



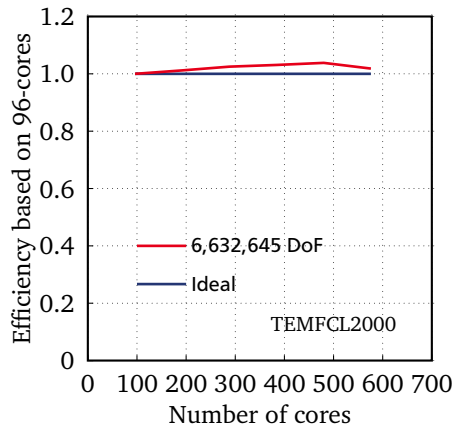
(a) TEMFCL1000 speedup



(b) TEMFCL1000 efficiency



(c) TEMFCL2000 speedup



(d) TEMFCL2000 efficiency

Figure 6.11.: Strong scaling tests: Parallel speedup and efficiency conducted for the calculation of the smallest 615 eigen pairs of a billiard cavity being discretized with 3,407,398 and 6,632,645 hexahedral elements. Within the analyses, the eigen pairs are determined with the filtered Lanczos solver and the tests are performed on the computer cluster TEMFCL1000 as well as on the TEMFCL2000, owned by the Computational Electromagnetics Laboratory (TEMF) at TU Darmstadt. During the simulations, the hyper-threading technology was not employed.

Weak Scaling

Splitting the given problems over more and more processors yields to a certain point when there is not enough work for each processor to operate efficiently. Therefore, a series of increasingly larger problems are solved on correspondingly growing numbers of processors and the so-called weak scaling [34] is examined in this section. For this reason, the problem size and the number of processors grow in such a way that the amount of data per processor is kept constant. Analogously, the speed in operations per second of each processor also stays constant. Again the performance measurements are conducted for the Lanczos solver with polynomial filtering, where 100 iteration steps are executed for each problem size. Namely, the billiard cavity was discretized with 832, 486, 2, 273, 965, 3, 407, 398, 6, 632, 645, and 11, 554, 666 hexahedral elements. The results are shown in figure 6.12. Here, the used cluster is the TEMFCL1000 and as expected, the code scales good, meaning that the parallel execution time is nearly constant as the problem size and the number of processors grow.

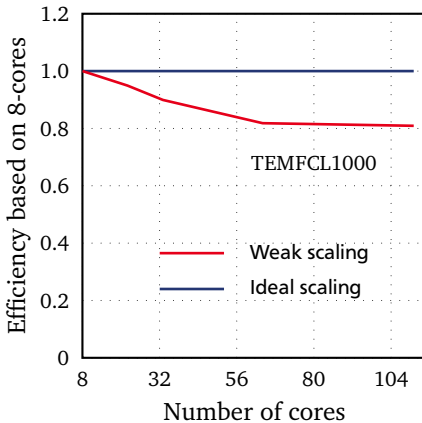


Figure 6.12: Weak scaling tests: Parallel efficiency conducted for 100 iteration steps of the Lanczos solver with polynomial filtering. The problem size and the number of processors are kept in such a way that the amount of data per processor stays constant. The tests are performed on the computer cluster TEMFCL1000, without employing the hyper-threading technology.

6.1.7 Level-Spacing Analysis

In this section the statistical properties of the three-dimensional stadium billiard are investigated. For this purpose, thousands of eigenfrequencies needed for its level-spacing analysis are numerically computed. A more close description of the level spacings is demonstrated in figure 6.13. In particular, a level spacing is defined as a difference between each two consecutive eigenfrequencies and afterward, with the obtained values the statistical distribution of the level spacings is cal-

culated. Accordingly, the eigenfrequency level-spacing analysis requires thousands of eigenfrequencies to be calculated for the stadium billiard and the accuracy of the eigenfrequencies has a crucial significance.

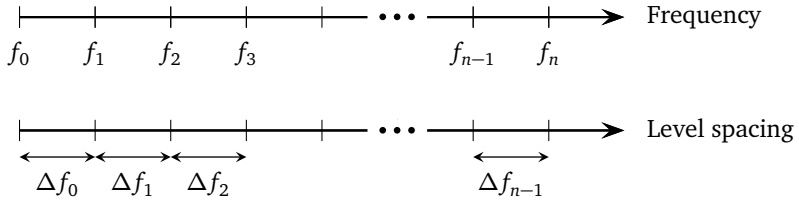


Figure 6.13.: Illustrative description of the level spacings. A level spacing Δf_n is defined as difference between each consecutive eigenfrequencies f_n .

As already mentioned in the introduction of the thesis, the goal of this work is also to compare the numerically calculated spectral properties with the measured ones. Therefore, the measurement data of the three-dimensional stadium billiard are kindly provided for comparison reasons by the Institute for Nuclear Physics at TU Darmstadt. In addition, the experimental investigations have been published in [27, 29].

For the numerical simulations, the time-domain approach and the frequency-domain approach using the Lanczos solver with polynomial filtering are exploited. In the simulation studies, it is experienced that for the time-domain field computations as well as for the Lanczos eigenvalue solver with polynomial filtering, a powerful personal computer is suited for problems with up to several millions of mesh cells. To be precise, the computer possesses 256 GB of RAM memory and two quad-core Intel Xeon E5-2643 processors, clocked at 3.3 GHz.

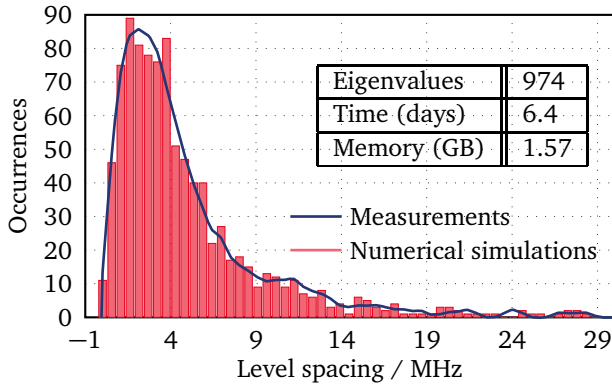
Using the time-domain approach, about 974 eigenfrequencies f_n are calculated for the billiard cavity structure up to 7.5 GHz. At this point, the billiard is discretized with a hexahedral mesh having 3,634,917 elements and the advantage that one single time-domain simulation can provide the whole response of an electromagnetic system in a wide frequency band is used. On the other side, 2,292 eigen pairs are calculated with the filtered Lanczos solver, where the structure is discretized with a hexahedral mesh having 3,379,770 elements. Analogously, the resulting matrix from the algebraic standard eigenvalue problem has 6,632,645 DoF. Here, the Lanczos solver with polynomial filtering is set to calculate the above mentioned eigenfrequencies along with their associated eigenvectors in three different simulations.

The level-spacing analyses based on the calculated eigenfrequencies are given in figure 6.14, where the computational time as well as the memory consumptions for the eigenvalue determination are also summarized. Prior to comparing the level-spacing analyses based on the eigenvalues calculated with the different numerical methods, an additional information about the computational costs is worth to be presented. That is, when compared to the frequency-domain approach, the memory usage of the time-domain method remains low even with a dramatical rise of the problem size. Consequently, the eigenvalue extraction from time-domain computations is a proper choice when the computational resources are limited. However, the frequency-domain approach shows significant reduction in the computational time, which in some applications is preferred over the burden of additional memory consumption.

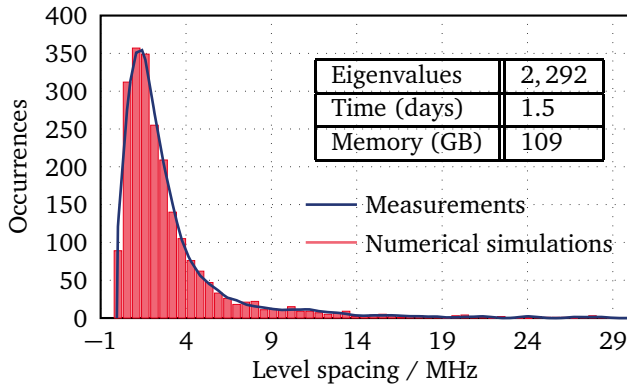
In both figures, 6.14a and 6.14b, the level spacings in MHz are given on the abscissa, whereas the ordinate shows the number of occurrences that belong to a specific frequency bin. According to these plots for the level-spacing analyses, it is obvious that smoother and better statistical properties are attained in case of more eigenvalues being determined. Additionally, the blue line in figures 6.14a and 6.14b shows the processed data, which are obtained from the measurements with antennas placed at different positions inside of the billiard cavity. In the experimental setup, the billiard has been constructed from niobium with the aim to reach superconductivity by a continuous cooling with liquid helium at low temperatures (4.2K). As a result, the cooling is naturally accompanied with a geometrical shrinkage of the cavity. Thus, the measurement data are scaled with a factor that compensates for the difference in the dimensions of the measured and the simulated structure. To compare the measurement data with the simulation results identical number of eigenvalues is used.

According to figure 6.14, it is worth mentioning that the numerically calculated histograms agree well with the corresponding curve obtained with the measurements. In addition, the robustness of the different approaches is investigated and the results indicate that the number of eigenfrequencies found with the proposed approaches coincides with the reference data. Finally, it can be concluded that the measured spectrum closely resembles those obtained by the numerical simulations.

In order to examine the convergence of the distributions for the level-spacing analysis, several hexahedral mesh cells are used to calculate around 2,300 eigenfrequencies. The results are obtained with the Lanczos solver with polynomial filtering and they are depicted in figure 6.15. From this figure, it is clearly observable that the different simulation scenarios yield the expected Wigner distribution for the level-spacing analysis [27, 29].



(a) Eigenfrequencies from the time-domain approach



(b) Eigenfrequencies from the frequency-domain approach

Figure 6.14.: Comparison of the numerically obtained level-spacing analysis with the one calculated from the measurements. (a) Eigenfrequency level-spacing analysis based on the eigenvalues, which are extracted with the time-domain approach. The billiard cavity is discretized with a hexahedral mesh having 3,634,917 mesh elements.(b) Eigenfrequency level-spacing analysis based on the eigenvalues, which are determined with the Lanczos solver with polynomial filtering. The billiard cavity is discretized with a hexahedral mesh having 3,379,770 mesh elements.

The eigenvectors corresponding to the desired eigenvalues are also determined with the frequency-domain approach. In order to examine the accuracy of their calculation, the electric field patterns for several modes of the billiard cavity are

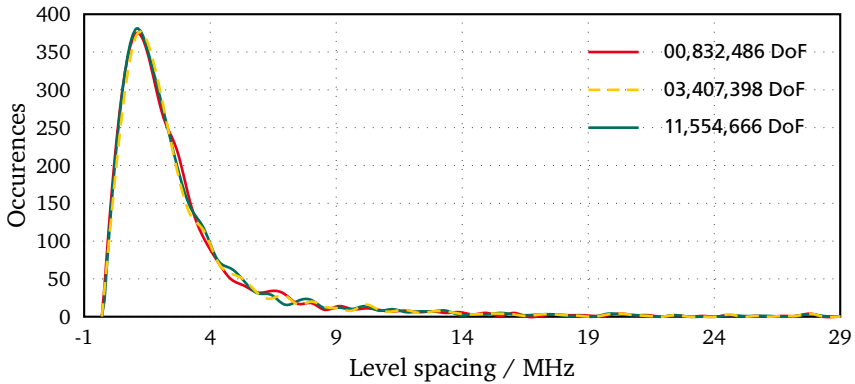


Figure 6.15.: Level-spacing analyses conducted for different hexahedral meshes. For each distribution, around 2,300 eigenfrequencies are calculated using the Lanczos solver with polynomial filtering.

compared with the patterns obtained with the CST MWS. Finally, the numerically calculated eigenvectors are in good accordance with those obtained by the numerical simulations with CST MWS, second, the parallel program implementation has proven to work in a robust, accurate, and stable fashion, and third, the proposed procedures for determining thousands of eigen pairs are applicable and complete.

6.2 Application Example: Dirac Billiard Cavity

6.2.1 Level-Density Analysis

The Institute for Nuclear Physics at TU Darmstadt has recently started with new series of experiments concerning the modelling of the properties of graphene with the help of microwave photonic crystal. Graphene is a monoatomic layer of carbon atoms arranged on a honeycomb lattice [59, 58]. In other words, the graphene is one of the crystalline forms of carbon, where the carbon atoms are arranged in a regular hexagonal pattern. Additionally, it can be described as one-atom thick layer of the layered mineral graphite. High-quality graphene is very strong, light, nearly transparent, and an excellent conductor of heat and electricity. Its interaction with other materials and with light, and its inherently two-dimensional nature, produce unique properties. Due to its peculiar electronic properties, the carbon allotrope attracted a lot of attention over the last years, which culminated in a Nobel prize

in 2010. Andre Geim and Konstantin Novoselov at the University of Manchester won the Nobel prize in physics “for groundbreaking experiments regarding the two-dimensional material, graphene”.

The conductance and the valence band of the electronic energy in graphene form conically shaped valleys that touch each other at the six corners of the hexagonal Brillouin zone [16, 17]. Close to these, the electron energy depends linearly on the quasi momentum. The linear dispersion relation implies an energy independent velocity, that is, near these points the electrons and holes behave like massless relativistic particles, described by the Dirac equation for spin-one-half particles. This results in a number of peculiar electronic properties, which have an analogue in the relativistic quantum mechanics. In the literature the touching points are referred to as Dirac points and their frequencies as Dirac frequencies.

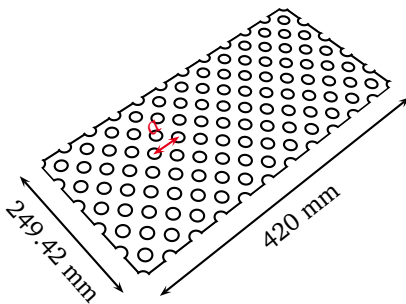


Figure 6.16: Superconducting microwave Dirac billiard cavity containing 888 metal cylinders with radius $r = 4$ mm and height $h = 3$ mm, squeezed between two metallic plates. The cavity is constructed from brass and coated with lead. The lattice constant is $a = 12$ mm and the resulting photonic crystal has a size of $249.42 \text{ mm} \times 420 \text{ mm} \times 3 \text{ mm}$.

It is worth mentioning that the band structure of the photonic crystal possesses similar properties. The photonic crystal considered in the present work is three-dimensional and composed of rows of metallic cylinders, which are arranged to form the triangular lattice, schematically shown in figure 6.16. The similarity of the band structure of a macroscopic photonic crystal with the electronic band structure of graphene, which is experimentally much more difficult to access, allows the experimental study of various relativistic phenomena. Therefore, at the Institute for Nuclear Physics, a photonic crystal composed of a total of 888 metallic cylinders, which are arranged on a triangular lattice and squeezed between two metal plates, has been constructed. The metallic cylinders have radius $r = 4$ mm and height $h = 3$ mm. The lattice constant is $a = 12$ mm and the resulting photonic crystal has a size of $249.42 \text{ mm} \times 420 \text{ mm} \times 3 \text{ mm}$. Each cylinder is screwed to the top and the bottom brass plate to ensure a proper mechanical stability and thus, reproducibility of the measurements. Both the lid and the body are leaded, in order to reach superconductivity by cooling with liquid helium at low temperatures (4.2 K).

In the experiments, the transmission and the reflection spectra are measured and the results on the detection of a Dirac point in a microwave photonic crystal are published in [16, 24]. At the frequency of the Dirac point, the spectra reveal a clear cusp structure, which is directly related to the local density of states, which tends to zero linearly with the excitation frequency in the vicinity of the Dirac point.

The purpose of this work is to compare the spectral properties of the superconducting Dirac billiard cavity, which were numerically calculated, with the measurements. For this application example, the frequency-domain approach using the filtered Lanczos solver and the B-Lanczos solver with shift-and-invert will be exploited. Specifically for this work, the spectrum of the Dirac billiard cavity is calculated from 19.0 GHz to 30.5 GHz and is compared with the measurements. Using the Lanczos solver with polynomial filtering, 1,656 eigenfrequencies up to 30.5 GHz have been calculated for the Dirac billiard cavity. At this point, the billiard has been discretized with a hexahedral mesh having 4,515,840 elements. This results in a matrix having 7,015,426 DoF. On the other side, the same number of eigenfrequencies has been calculated with the B-Lanczos solver with shift-and-invert for the Dirac billiard cavity, which has been discretized with a tetrahedral mesh having 630,348 elements. Analogously, the resulting matrices for the algebraic generalized eigenvalue problem have 2,875,770 DoF. The Lanczos solver with polynomial filtering was set to calculate the above mentioned eigenfrequencies in two simulations, while the B-Lanczos solver with shift-and-invert calculated the sought eigenfrequencies in eight simulations.

	CEM3D	Filtered Lanczos	B-Lanczos shift-and-invert
Eigenfrequencies	1,656	1,656	1,656
Time (days)	7.4	0.4	1.6
Memory (GB)	23.87	162.87	57.71
Memory/eig (MB)	698.48	201.31	295.20

Table 6.3.: Computational time and memory consumptions for the determination of 1,656 eigenfrequencies with the CEM3D solver, the Lanczos solver with polynomial filtering, and the B-Lanczos solver with shift-and-invert.

The matrices for the generalized eigenvalue formulation were also used for the CEM3D eigenmode solver. Here, the CEM3D eigenmode solver was run in parallel to calculate the sought modes. As already mentioned, the CEM3D solver employs the FEM formulation by means of higher order curvilinear elements followed by the Jacobi-Davidson method to solve the generalized eigenvalue problem. For this

scenario, several target frequencies were specified within the CEM3D solver and the required eigenfrequencies were calculated by groups of 35 eigenfrequencies in each simulation.

Prior to comparing the level-density analyses based on the eigenvalues calculated with the different approaches, an additional information about the used computational resources is presented. In the simulation studies, it was experienced that for the Lanczos solver with polynomial filtering, powerful cluster machines are suited for problems with more than 10^6 mesh cells. To be precise, 15 nodes from the computer cluster TEMFCL2000, each with two twelve-core Intel Xeon X5650 processors, clocked at 3.0 GHz, and 24 GB RAM memory, were used. For the CEM3D solver, since the problem to be solved is two times smaller, only 8 cluster nodes were exploited. On the other side, for the B-Lanczos solver with shift-and-invert, a powerful personal computer with two quad-core Intel Xeon E5-2643 processors, clocked at 3.3 GHz, and 256 GB of RAM memory has been used. The computational time as well as the memory consumptions for the eigenvalue determination are summarized in table 6.3.

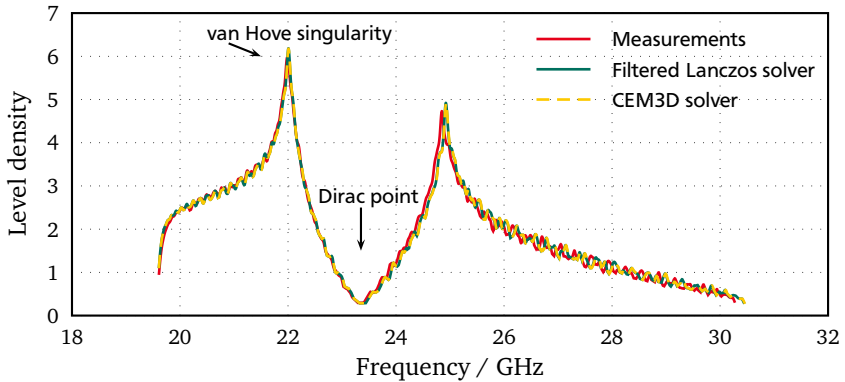


Figure 6.17.: Comparison of the spectral properties for a superconducting Dirac billiard cavity, which were measured and numerically calculated. The frequency-domain approach using the Lanczos solver with polynomial filtering has been used. As reference data, the level-density distribution computed with the CEM3D eigenmode solver has been considered.

The level-density analyses based on the calculated eigenvalues are given in figure 6.17. On the abscissa are given the frequencies in GHz and the ordinate presents the occurrences that belong to a specific frequency, or the so-called level-density analysis, obtained with the help of a Lorentz function [24]. In the con-

sidered frequency spectrum only one band with a Dirac point is shown. Below 19.0GHz there are no resonances (band gap). Also, after 30.5GHz a band gap can be noticed. As displayed in this figure, it is clear that the number of resonances in the range of 23.5GHz decreases greatly. This behavior reflects the vanishing density of states at the Dirac point.

During the measurements, the analyzed structure is cooled down at temperature of 4.2K and therefore, its dimensions are shrunk. In what follows, the measurement data are scaled with a factor that compensates for the difference in the dimensions of the measured and the simulated structure. The red line shows the reflection spectrum measured with antennas placed at different positions inside of the photonic crystal. The locations of the antennas are chosen in the center of three cylinders, forming a triangle, to minimize the disturbance of the propagating mode at the Dirac frequency. The experimental reflection spectrum has a clearly pronounced minimum around 23.5 GHz, i.e. within the frequency range where the Dirac point is expected, and shows the characteristic cusp structure. The sharp resonances at the edges of the bands are related to the so-called van Hove singularities. Evidently, the measured reflection spectrum closely resembles those obtained by the numerical simulations.

7 Summary and Outlook

In this thesis, superconducting cavities have been analyzed via an employment of different numerical approaches to calculate plenty of eigen pairs. Specifically, thousands of eigenfrequencies for the billiard and the Dirac billiard cavity have been numerically computed. Based on the acquired eigenfrequencies, the statistical analyses for the billiard and the Dirac billiard cavity have been investigated. Using the level-spacing and the level-density analysis, the relevant properties of the atoms and the graphene have been modeled, respectively.

The numerical simulations have been performed, on the one hand, via the time-domain solver that was developed and implemented especially for this thesis and on the other hand, via the frequency-domain solvers. The time-domain solver for eigenfrequency extraction uses the time-domain responses for a superconducting closed resonator and by means of signal processing techniques extracts the eigenfrequencies. The frequency-domain solvers are based on the Finite Integration Technique (FIT), the Finite Element Method (FEM) with higher order curvilinear elements, and the Lanczos method with its variations for the solution of the eigenvalue problem itself. It should be emphasized that the numerical results have been compared with the analytical solutions, the FEM simulations as well as the measurements and a reasonable agreement has been shown. The measurements of the billiard cavities have been carried out by the Institute for Nuclear Physics at the Technical University of Darmstadt and were kindly provided for comparison reasons. Beside the accuracy, the robustness of the underlying approaches was also investigated throughout this work. At the end, with the intention of obtaining insights in the performance of the codes, scalability, time, and memory consumption analyses have been conducted.

7.1 Contributions

As mentioned earlier, the major challenges posed by this work are: first, the ability of the approaches to tackle the large-scale eigenvalue problem, second, the capability to extract many, i.e. order of thousands, (interior) eigenfrequencies for the considered cavities, third, the ability to ensure high accuracy as well as robustness of the underlying approaches, and fourth, an efficient implementation. In the following, the particular achievements of this thesis will be summarized.

First, an approach for eigenfrequency extraction has been presented under the assumption that the time-domain responses for a superconducting closed resonator are available. The reader is referred to [12, 14] where parts of the time-domain approach were published. This approach uses the advantage that one single time-domain simulation can provide the whole response of an electromagnetic system in a wide frequency band, which is a strong point of this work in order to yield a fulfillment of the aforementioned project requirements. The proposed approach can be regarded as an extension of the classical approach in finding eigenfrequencies, where the idea is to look for local maxima of the frequency spectrum. However, the essential novelty of this approach lies in the capability of the approach to accurately extract plenty of eigenfrequencies with the help of digital signal processing techniques applied to the data obtained by the fast time-domain responses. For this purpose, two variations of the time-domain approach have been developed, i.e. using parametric fit in Frequency Domain (FD) and in Time Domain (TD).

A further contribution of this work includes an approach for eigenfrequency determination in FD. A part of this contribution was published in [15, 11]. With the aim to compute the electromagnetic fields for a superconducting cavity, this approach is based on the Finite Integration Technique (FIT) or the Finite Element Method (FEM) with higher order curvilinear elements. Afterward, the Lanczos method with its variations is employed for the solution of the standard or the generalized eigenvalue problem. The main novelty of this work is to apply the filtering methods, which are valuable tools for enabling the computation of interior eigenvalues and their eigenvectors as well as speeding up the convergence of the standard and the generalized Lanczos algorithm. For the calculation of the extreme eigenvalues together with the appropriate eigenvectors, the basic Lanczos implementations have been exploited.

The efficient implementation with the main focus on low computational costs provides another contribution of this work. Here, an extension to the proposed frequency-domain solvers was enabled to deal with higher mesh resolution for the considered resonators, facilitating distributed-memory architecture with Message Passing Interface (MPI) parallelization strategy such that the simulation time is kept on a lower level. Namely, the Lanczos solvers were built on the top of the Portable, Extensible Toolkit for Scientific Computation (PETSc) library, which enables distributed-memory computations.

In addition to the need to ensure high precision of the proposed approaches, the calculated eigenfrequencies are compared side by side with the reference data, which were determined either by the analytical expressions or by the measurements as well as the CEM3D eigenmode solver. Hereby, the findings show that the proposed approaches result in solutions which agree well with the reference data,

gaining high accuracy and efficiency in eigenvalue determination. Furthermore, analyses were made for the further essential features of the presented time-domain solver. That is, the difference between the time-domain approach using a parametric fit in FD and in TD was studied and it was shown that the time-domain approach with fitting in TD leads to more accurate results.

A further main aspect of this work is the robustness of the underlying techniques. Here, the robustness and the convergence of the proposed approaches have been inspected with the reference data. Moreover, the robustness of the time-domain approach has been ensured by the applied extension from [14], where more than one acquired time-domain responses for the analyzed cavity can be taken into account and post-processed.

Summing up, the time- and the frequency-domain approaches are able to accurately determine many eigenfrequencies of closed resonators and they are fast as well as memory-efficient compared to others presented in the literature. Finally, all of the results indicate that the suggested techniques can be applicable in different areas of applications, where a precise determination of plenty of eigenfrequencies takes a crucial role.

7.2 Outlook

Although the thesis provides finalized approaches for an accurate determination of plenty of eigenfrequencies, some further research aspects and improvements have not been addressed.

A further research aspect that remains unaddressed includes the more thorough analysis of the case when two or more frequencies are very close to each other. In addition, enhanced investigations on the modes excitation for the time-domain approach could be accomplished. This would allow for quantifying the possibility that all of the modes will be excited.

Additionally, there remain possible enhancements of the Lanczos solver with polynomial filtering for the case when the requested frequency range is narrow, which results in a polynomial with a high degree.

Also, as future work, possible applications of the proposed approaches could be treated and used.



A Fourier Transforms

$f(t) = \frac{1}{2\pi} \int_{-\infty}^{\infty} e^{i\omega t} \widehat{f}(\omega) d\omega$	$\widehat{f} = \int_{-\infty}^{\infty} e^{-i\omega t} f(t) dt$
$a \sin bt$	$i\pi a \delta(\omega + b) - i\pi a \delta(\omega - b)$
$a \cos bt$	$\pi a \delta(\omega + b) + \pi a \delta(\omega - b)$
$\frac{1}{t^2 + a^2} (a > 0)$	$\frac{\pi}{a} e^{-a \omega }$
$u(t) e^{-at}$	$\frac{1}{a + i\omega}$
$u(-t) e^{at}$	$\frac{1}{a - i\omega}$
$e^{-a t } (a > 0)$	$\frac{2a}{a^2 + \omega^2}$
e^{-t^2}	$\sqrt{\pi} e^{-\omega^2/4}$
$\frac{1}{2a\sqrt{\pi}} e^{-t^2/(2a)^2} (a > 0)$	$e^{-a^2\omega^2}$
$\frac{1}{\sqrt{ t }}$	$\sqrt{\frac{2\pi}{ \omega }}$
$u(t + a) - u(t - a)$	$\frac{2 \sin \omega a}{\omega}$
$\delta(t - a)$	$e^{-i\omega a}$
$f(at + b) (a > 0)$	$\frac{1}{a} e^{ib\omega/a} \widehat{f}\left(\frac{\omega}{a}\right)$
Linearity of transform and inverse: $\alpha f(t) + \beta g(t)$	$\alpha \widehat{f}(\omega) + \beta \widehat{g}(\omega)$
Transform of derivative: $f^{(n)}(t)$	$(i\omega)^n \widehat{f}(\omega)$
Transform of integral: $f(t) = \int_{-\infty}^t g(x) dx$	$\widehat{f}(\omega) = \frac{1}{i\omega} \widehat{g}(\omega)$
Convolution theorems: $f(t) * g(t) = \int_{-\infty}^{\infty} f(t - x) g(x) dx$	$\widehat{f}(\omega) \widehat{g}(\omega)$
$f(t)g(t)$	$\frac{1}{2\pi} \widehat{f}(\omega) * \widehat{g}(\omega)$

Table A.1.: Short table of Fourier transforms. u is the Heaviside step function.



List of Figures

- 1.1. Three-dimensional generalized stadium billiard, consisted of two quarter cylinders with different radii. It is made of niobium, which becomes superconducting at temperatures below 9.2 K. The picture of the billiard cavity was kindly provided by the Institute for Nuclear Physics at the Technical University (TU) of Darmstadt [27, 29, 1]. 3
- 1.2. Superconducting microwave Dirac billiard cavity containing 888 metal cylinders. It is constructed from brass and coated with lead. On the figure, the lid is shifted with respect to the billiard body. The picture of the Dirac billiard cavity is copyrighted and property of the Institute for Nuclear Physics at the Technical University of Darmstadt [28]. 4

- 2.2. Indexing of the edges and the faces. Each edge and face has the same index in x-, y-, and z- direction as well as the same starting node (point). 17
- 2.6. Update scheme of the Leapfrog method in which the magnetic grid voltages are evaluated at the whole time steps $t_m = t_0 + m \Delta t$ and the electric grid voltages at the half time steps $t_{m+1/2} = t_0 + (m + 1/2) \Delta t$. The recursion includes each of the magnetic and the electrical parameters of the last time step with length Δt 29

- 3.5. Comparison of a non-periodic sine wave and its amplitude spectrum with leakage to the windowed sine wave and its amplitude spectrum showing no leakage. 55

- 5.1. Time-domain response that is acquired from the transient solver in CST Microwave Studio® (CST MWS) and its Gaussian windowing. The responses represent the electric field intensity of a superconducting cavity [12]. 74

5.2. Amplitude spectrum of a time-domain response and a Gaussian windowed time-domain response of a superconducting cavity. Only a part of the amplitude spectrum is illustrated on this figure. As expected, the amplitude spectrum of the Gaussian windowed time-domain response consists of Gaussian pulses that are located on the positions where the eigenfrequencies are [12].	75
5.3. Operating signal during the process of eigenfrequency extraction, an isolated Gaussian pulse within the eigenmode spectrum. The Gaussian pulse is constituted of several frequency samples and it is located using the described technique from section 5.1.3. In an ideal case, the Gaussian pulse should be replaced with a Dirac pulse [12].	76
5.4. Operating signal during the process of eigenfrequency extraction, Gaussian modulated signal. The signal is obtained when the Inverse Fast Fourier Transform (IFFT) is performed on a shifted Gaussian pulse in frequency domain [12].	78
5.5. Convergence of the resonance frequency for the TE_{011} mode of the rectangular microwave cavity with dimensions $a = 20$ cm, $b = 10$ e cm, and $c = 10\pi$ cm. The rectangular cavity has been discretized with several hexahedral meshes and the numerical solution is compared to the analytical one.	81
5.6. Relative deviation of the numerically obtained values \hat{f} for the lowest eigenfrequency to the analytical result f as a function of the hexahedral mesh cells for a rectangular, cylindrical, and spherical resonator [12].	82
5.7. Comparison of the different approaches for calculating the resonance frequency for the TE_{011} mode of the rectangular microwave cavity with dimensions $a = 20$ cm, $b = 10$ e cm, and $c = 10\pi$ cm. The rectangular cavity has been discretized with 1, 109, 862 hexahedral mesh cells. Here, the analytically calculated eigenfrequency has been compared with the time-domain approach for eigenfrequency extraction, when fitting in time or in frequency domain is used. . . .	83

5.8. Convergence study showing a comparison between the eigenfrequencies calculated with the proposed time-domain approach (red and green color) and the analytically obtained eigenfrequencies (blue color). The analyzed structure within this study is the spherical cavity with a radius $R = 1$ m. For the time-domain approach three different hexahedral discretization meshes have been used and two post-processing scenarios with one and two probes have been taken into consideration. One frequency around 400 MHz is missing when using only one probe.	84
5.9. Relative deviation (©2014 IEEE) of the analytically obtained values f to the numerical results \hat{f} as a function of the number of tetrahedral mesh cells for a spherical resonator with radius $R = 1$ m. The first two worst computed degenerated mode eigenfrequencies are considered for the spherical cavity [15].	88
5.10. Convergence study (©2014 IEEE) showing a comparison between the eigenfrequencies calculated with the proposed frequency-domain approach (red color) and the analytically obtained eigenfrequencies (blue color). The analyzed structure within this study is the spherical cavity from section 5.2.3. For the frequency-domain approach six different tetrahedral discretization meshes have been used [15].	89
6.1. Desymmetrized version of the three-dimensional generalized stadium billiard, consisted of two quarter cylinders with radii $r_1 = 200.0$ mm and $r_2 = 141.4$ mm. The cylinders are rotated with respect to each other by 90° . The billiard is made of niobium that becomes superconducting at temperatures below 9.2 K and its classical dynamics are chaotic.	92
6.2. Relative deviation (©2013 IEEE) of the numerically obtained values \hat{f} to the reference results f as a function of the mesh cells for a billiard resonator. The mode oscillating at 2.37 GHz is determined. The time-domain approach is based on the FIT with hexahedral mesh, whereas the frequency-domain approach takes advantage of the FEM with higher order curvilinear elements [14].	96
6.4. Theoretical and measured connection between the number of modes and the frequency. The theoretical connection has been calculated using the equation (6.2). For the measured connection, about 900 eigenfrequencies up to 7 GHz have been extracted for the billiard cavity structure by employing the time-domain approach.	98

6.5. Convergence study (©2013 IEEE) showing a comparison between the eigenfrequencies calculated with the proposed time-domain approach (green color) and the reference eigenfrequencies obtained with the CEM3D eigenmode solver based on higher order curvilinear elements (red color). For the time-domain approach a hexahedral discretization mesh is used. At the same time, the reference data are obtained using a tetrahedral discretization mesh [14].	99
6.6. Graphical representation of the different requested eigen ranges with its dimension. $[a, b]$ presents the full eigen range. Six distinct scenarios are illustrated.	100
6.9. Convergence rate of the B-Lanczos and the B-Lanczos with shift-and-invert solver for the eigencomputations in simulation #1. The matrix pencils have 1,163,238 DoF and the error is plotted at the every 10-th iteration step. The convergence of the B-Lanczos solver with shift-and-invert is very fast. The B-Lanczos solver calculates additional 30 large-most eigenfrequencies in order the requested 70 eigenfrequencies to be reached.	103
6.10. Computational time (left) and memory consumptions (right) of selected eigenvalue solvers for the determination of 100 large-most eigenvalues (©2013 IEEE). Different number of curvilinear tetrahedral and hexahedral discretization meshes for the billiard cavity are used within the frequency- and the time-domain methods, respectively [14].	104
6.12. Weak scaling tests: Parallel efficiency conducted for 100 iteration steps of the Lanczos solver with polynomial filtering. The problem size and the number of processors are kept in such a way that the amount of data per processor stays constant. The tests are performed on the computer cluster TEMFCL1000, without employing the hyper-threading technology.	108
6.13. Illustrative description of the level spacings. A level spacing Δf_n is defined as difference between each consecutive eigenfrequencies f_n	109
6.15. Level-spacing analyses conducted for different hexahedral meshes. For each distribution, around 2,300 eigenfrequencies are calculated using the Lanczos solver with polynomial filtering.	112



6.16. Superconducting microwave Dirac billiard cavity containing 888 metal cylinders with radius $r = 4$ mm and height $h = 3$ mm, squeezed between two metallic plates. The cavity is constructed from brass and coated with lead. The lattice constant is $a = 12$ mm and the resulting photonic crystal has a size of 249.42 mm \times 420 mm \times 3 mm. 113

6.17. Comparison of the spectral properties for a superconducting Dirac billiard cavity, which were measured and numerically calculated. The frequency-domain approach using the Lanczos solver with polynomial filtering has been used. As reference data, the level-density distribution computed with the CEM3D eigenmode solver has been considered. 115



Acronyms and Symbols

Acronyms

2D	Two Dimensional
3D	Three Dimensional
ARPACK	Arnoldi Package
BEM	Boundary Element Method
BLAS	Basic Linear Algebra Subprograms
CEM	Computational Electromagnetics
CEM3D	Computational Electromagnetics 3D
CG	Conjugate Gradient
CPU	Central Processing Unit
CSR	Compressed Sparse Row
CST MWS	CST Microwave Studio [®]
DFT	Discrete Fourier Transform
DoF	Degrees of Freedom
FD	Finite Differences
FD	Frequency Domain
FTD	Finite-Difference Time-Domain Method
FEM	Finite Element Method
FFT	Fast Fourier Transform
FIT	Finite Integration Technique

GMRES	Generalized Minimal RESidual method
GoF	Goodness of the Fitting
GPU	Graphics Processing Unit
IFFT	Inverse Fast Fourier Transform
LAPACK	Linear Algebra Package
LU	Lower Upper
MKL	Math Kernel Library
MoM	Method of Moments
MPI	Message Passing Interface
PETSc	Portable, Extensible Toolkit for Scientific Computation
PRIMME	PREconditioned Iterative MultiMethod Eigensolver
RAM	Read Access Memory
RF	Radio Frequency
SI	Shift-and-Invert
SLEPc	Scalable Library for Eigenvalue Problem Computations
SPL	Superconducting Proton Linac
TD	Time Domain

Roman Letters

A	Area in \mathbb{R}^3
\mathbf{A}	Matrix from an eigenvalue problem
\mathbf{A}_{CC}	Curl-curl matrix
$A(i, j, k)$	Primary elementary surfaces
$\tilde{A}(i, j, k)$	Dual elementary surfaces

$A(\omega)$	Amplitude	
a	Scalar	
a	Parameter coefficient	
a, b	Bounds for the spectrum of \mathbf{A}	
a_j	Unknown coefficients	
a_n	Fourier coefficients	
\mathbf{B}	Matrix from an eigenvalue problem	
$\vec{B}, \underline{\vec{B}}$	Magnetic flux density and complex amplitude	$[\text{V s m}^{-2}]$
b	Scalar	
b	Source function	
b	Parameter coefficient	
$\widehat{\mathbf{b}}, \underline{\widehat{\mathbf{b}}}$	Discrete magnetic flux density and complex amplitude	
b_n	Fourier coefficients	
$\widehat{\underline{\mathbf{b}}}(i, j, k)$	Discrete magnetic flux density	$[\text{V s m}^{-2}]$
$\mathbf{C}, \underline{\mathbf{C}}$	Discrete curl operator for primary and dual grid	
\mathbf{C}^T	Transpose of the discrete curl operator for primary grid	
c	Function	
c	Scalar	
c	Parameter coefficient	
c_n	Complex Fourier coefficients	
$\vec{D}, \underline{\vec{D}}$	Electric flux density and complex amplitude	$[\text{C m}^{-2}]$
d	Parameter coefficient	
$\widehat{\mathbf{d}}, \underline{\widehat{\mathbf{d}}}$	Discrete electric flux density and complex amplitude	
$\widehat{\underline{\mathbf{d}}}(i, j, k)$	Discrete electric flux density	$[\text{C m}^{-2}]$
$dA, d\vec{A}$	Infinitesimal area element, scalar and oriented	
$ds, d\vec{s}$	Infinitesimal path element, scalar and oriented	
dV	Infinitesimal volume element	
dx	Infinitesimal path element, oriented in x direction	
dy	Infinitesimal path element, oriented in y direction	
dz	Infinitesimal path element, oriented in z direction	
E	Total number of edges	
$\underline{\vec{E}'}$	Test field	

\vec{E}, \underline{E}	Electric field strength and complex amplitude	[V m ⁻¹]
$\underline{e}, \underline{\hat{e}}$	Discrete electric voltage and complex amplitude	
$\hat{e}(i, j, k)$	Discrete electric voltage	[V m ⁻¹]
e_j	Unknown coefficients	
F	Operator	
F	Total number of facets	
F_s	Sampling frequency	[s ⁻¹]
\vec{F}	Vector	
f	Function	
f	Frequency	[s ⁻¹]
$\widehat{f}(\omega)$	Fourier transform of the function $f(t)$	
$\widehat{f}_{im}(\omega)$	Dispersion part	
$\widehat{f}_{re}(\omega)$	Absorption part	
G	Primary grid	
\widetilde{G}	Dual grid	
\vec{G}	Vector	
g	Function	
g	Weighting function	
$\widehat{g}(\omega)$	Fourier transform of the function $g(t)$	
\vec{H}, \underline{H}	Magnetic field strength and complex amplitude	[A m ⁻¹]
h	Function	
$\underline{\hat{h}}, \underline{\hat{h}}$	Discrete magnetic voltage and complex amplitude	
$\hat{h}(i, j, k)$	Discrete magnetic voltage	[A m ⁻¹]
\mathbf{I}	Identity matrix	
i, j, k	Indices	
\vec{J}, \underline{J}	Current density and complex amplitude	[A m ⁻²]
\vec{J}_c	Conduction current density	[A m ⁻²]
\vec{J}_{cv}	Convection current density	[A m ⁻²]
\vec{J}_i	Impressed current density	[A m ⁻²]
j	Imaginary unit, $j = \sqrt{-1}$	
$K_m(\mathbf{A}, \vec{v})$	Krylov subspace	
L	Length of a cylindrical cavity	
$L(i, j, k)$	Primary elementary edges	

$\tilde{L}(i, j, k)$	Dual elementary edges	
M	Total number of time steps	
\vec{M}	Magnetization	[A m ⁻¹]
$\mathbf{M}_e, \mathbf{M}_\mu$	Material matrices	
m	Time step	
m	Dimension of a Krylov subspace	
N	Total number of nodes	
N	Total number of time samples	
N	Length of a discrete signal	
N_A	Total number of primary elementary facets	
$N_{\tilde{A}}$	Total number of dual elementary facets	
N_L	Total number of primary elementary edges	
$N_{\tilde{L}}$	Total number of dual elementary edges	
N_p	Total number of primary elementary points	
$N_{\tilde{p}}$	Total number of dual elementary points	
N_V	Total number of primary elementary volumes	
$N_{\tilde{V}}$	Total number of primary elementary volumes	
N_x, N_y, N_z	Number of points in each coordinate direction of the primary grid	
n	Dimension of a matrix	
n	Index	
n	Positive integer	
\vec{n}	Normal vector	
n_{freq}	Number of eigenfrequencies	
nnz	Non-zero elements	
\vec{P}	Electric polarization	[C m ⁻²]
$P(i, j, k)$	Primary elementary points	
$\tilde{P}(i, j, k)$	Dual elementary points	
$P(\omega)$	Phase	
p	Half period of a function	
$p \in \{x, y, z\}$	Cartesian coordinate	
R	Residual	
R	Radius of a cylindrical cavity	

r	Radius of a billiard cavity	
\vec{r}	Position vector in \mathbb{R}^3	[m]
\vec{r}	Residual vector	
r_i	Residual for the i -th data point	
S	Summed squares of residuals	
$\mathbf{S}, \tilde{\mathbf{S}}$	Discrete divergence operator for primary and dual grid	
$s(\lambda)$	Polynomial	
T	Time grid	
T	Duration of a time signal	
T	Total number of tetrahedra	
\mathbf{T}	Tridiagonal matrix	
T_s	Sampling time	[s]
t	Time	[s]
U	Function space	
u	Unknown function	
u	Function	
$u(t)$	Heaviside step function	
V	Volume in \mathbb{R}^3	
\mathbf{V}	Matrix that contains Lanczos vectors	
$V(i, j, k)$	Primary elementary volumes	
$\tilde{V}(i, j, k)$	Dual elementary volumes	
\vec{W}^e	Space of edge functions	
w	Basis function	
w	Gaussian window	
\vec{w}^e	Edge basis function	
\vec{w}^f	Face basis function	
X	Design matrix for a fit model	
x	Generic point of the domain Ω	
x	Cartesian coordinate	
\mathbf{x}	Eigenvector	
\vec{x}	Vector	
\vec{x}	Lanczos vector	

$x(n)$	Discrete signal
Y	Fit model
y	Vector of fit responses
y	Cartesian coordinate
\vec{y}	Ritz eigenvector of \mathbf{T}
\vec{y}	Vector
y_i	Observed response value for the i -th data point
\hat{y}_i	Fitted response value for the i -th data point
z	Cartesian coordinate

Greek Letters

α	Scalar	
β	Vector of fit parameters	
β	Scalar	
γ	Scalar	
δ	Delta function	
ε	Vector of errors	
ε	Permittivity	[F m ⁻¹]
ε_0	Permittivity of free space, $\varepsilon_0 = 8.854 \cdot 10^{-12} \text{ F m}^{-1}$	[F m ⁻¹]
$\bar{\varepsilon}(i, j, k)$	Averaged permittivity	[F m ⁻¹]
ε_r	Relative permittivity	
θ	Ritz eigenvalue of \mathbf{T}	
θ	Eigenvalue	
λ	Eigenvalue	
μ	Permeability of a magnetic material	[H m ⁻¹]
μ	Mean value for a Gaussian pulse	
μ_0	Permeability of free space, $\mu_0 = 4\pi \cdot 10^{-7} \text{ H m}^{-1}$	[H m ⁻¹]
$\bar{\mu}^{-1}(i, j, k)$	Averaged inverse permeability	[m H ⁻¹]
μ_r	Relative permeability	
ξ, η	Bounds for desired eigenvalues	
$\Pi_a(t)$	Rectangular function	

ϖ	Shifted angular frequency	$[s^{-1}]$
ρ	Polynomial	
ρ	Charge density	$[C\ m^{-3}]$
$\rho(\lambda)$	Polynomial that approximates the filter $\varphi(\lambda)$	
σ	Electric conductivity	$[S\ m^{-1}]$
σ	Shift	
σ	Standard deviation	
τ	Time shift	$[s]$
φ	Phase of a sinusoid	$[rad]$
$\varphi(\lambda)$	Base filter	
ω	Angular frequency, $\omega = 2\pi f$	$[s^{-1}]$
Ω	Domain of interest in the continuous space	
Ω	Shifted angular frequency	$[s^{-1}]$

General Symbols and Conventions

\mathcal{F}	Fourier transform
\mathcal{F}^{-1}	Inverse Fourier transform
\mathcal{O}	Order of complexity
\mathbb{R}	Real numbers
\mathbb{R}^+	Positive real numbers
Re	Real part of a complex number
\vec{x}	Spatial vector in \mathbb{R}^3
$\vec{x} \cdot \vec{y}$	Dot product of vectors \vec{x} and \vec{y}
$\vec{x} \times \vec{y}$	Cross product of vectors \vec{x} and \vec{y}
\underline{x}	Complex value
∇	Nabla operator, $\nabla = (\frac{\partial}{\partial x}, \frac{\partial}{\partial y}, \frac{\partial}{\partial z})^T$ in Cartesian coordinates
\in	“Element of” symbol
∂	Partial derivative operator

Bibliography

- [1] Institute for Nuclear Physics, Technical University of Darmstadt, Darmstadt. [Online]. Available: <http://www.ikp.tu-darmstadt.de> (Cited on pages 3 and 123.)
- [2] CST - Computer Simulation Technology AG, CST 2012, Darmstadt, Germany, MICROWAVE STUDIO. [Online]. Available: <http://www.cst.com> (Cited on pages 5, 6, 58, and 85.)
- [3] MATLAB R2011b, The MathWorks Inc., Natick, MA, 2011. (Cited on pages 6, 58, and 73.)
- [4] FFT window functions: Limits on FFT analysis. [Online]. Available: <http://www.bores.com/courses/advanced/windows/files/windows.pdf> (Cited on page 54.)
- [5] Understanding FFT Windows. [Online]. Available: <http://www.physik.uni-wuerzburg.de/~praktiku/Anleitung/Fremde/ANO14.pdf> (Cited on page 54.)
- [6] W. Ackermann, G. Benderskaya, and T. Weiland, "State of the art in the simulation of electromagnetic fields based on large scale finite element eigenanalysis," *International COMPUMAG Society Newsletter*, vol. 17, 2010. (Cited on pages 5 and 102.)
- [7] W. Ackermann and T. Weiland, "High precision cavity simulations," in *Proceedings of the 11th International Computational Accelerator Physics Conference*, 2012, pp. 1–5. (Cited on pages 5, 6, 31, 70, 85, 86, and 95.)
- [8] W. E. Arnoldi, "The principle of minimized iteration in the solution of the matrix eigenvalue problem," *Quarterly of Applied Mathematics*, vol. 9, no. 17, pp. 17–29, 1951. (Cited on page 6.)
- [9] C. Baker, U. Hetmaniuk, R. B. Lehoucq, and H. Thornquist, "Anasazi software for the numerical solution of large-scale eigenvalue problems," *ACM Transactions on Mathematical Software (TOMS)*, vol. 36, no. 3, pp. 1–23, 2009. (Cited on page 6.)

-
- [10] D. Balay, J. Brown, K. Buschelman, V. Eijkhout, W. Gropp, D. Kaushik, M. Knepley, L. McInnes, B. Smith, and H. Zhang, “PETSc users manual.” Argonne National Laboratory, 2011. (Cited on page 86.)
- [11] T. Banova, W. Ackermann, and T. Weiland, “Accurate determination of thousands of eigenvalues for large-scale eigenvalue problems,” in *Proceedings of the 19th Conference on the Computation of Electromagnetic Fields (Compumag 2013)*, July 2013, pp. 1–2. (Cited on page 118.)
- [12] —, “Eigenvalue extraction from time domain computations,” *Advances in Radio Science*, vol. 11, pp. 23–29, July 2013. (Cited on pages 60, 61, 74, 75, 76, 78, 82, 118, 123, and 124.)
- [13] —, “Eigenvalue study of a chaotic resonator,” in *Proceedings of the Frühjahrstagung der Deutschen Physikalischen Gesellschaft (DPG)*, March 2013. (Cited on page 61.)
- [14] —, “Performance analysis of eigenvalue extraction from time-domain computations,” in *Proceedings of the 43rd European Microwave Conference (EuMC)*, October 2013, pp. 1–4. (Cited on pages 61, 96, 99, 104, 105, 118, 119, 125, and 126.)
- [15] —, “Accurate determination of thousands of eigenvalues for large-scale eigenvalue problems,” *IEEE Transactions on Magnetics*, February 2014. (Cited on pages 69, 71, 87, 88, 89, 104, 118, and 125.)
- [16] S. Bittner, B. Dietz, M. Miski-Oglu, P. Oria Iriarte, A. Richter, and F. Schäfer, “Observation of a Dirac point in microwave experiments with a photonic crystal modeling graphene,” *Phys. Rev. B*, vol. 82, p. 014301, Jul 2010. [Online]. Available: <http://link.aps.org/doi/10.1103/PhysRevB.82.014301> (Cited on pages 3, 113, and 114.)
- [17] S. Bittner, B. Dietz, M. Miski-Oglu, and A. Richter, “Extremal transmission through a microwave photonic crystal and the observation of edge states in a rectangular Dirac billiard,” *Phys. Rev. B*, vol. 85, p. 064301, Feb 2012. [Online]. Available: <http://link.aps.org/doi/10.1103/PhysRevB.85.064301> (Cited on pages 3 and 113.)
- [18] A. Borisenko and I. Tarapov, *Vector and Tensor Analysis with Applications*, ser. Dover Books on Mathematics. Dover Publications, 1979. (Cited on page 10.)

-
- [19] A. Bossavit, *Computational Electromagnetism: Variational Formulations, Complementarity, Edge Elements*, ser. Academic Press series in electromagnetism. Academic Press, 1998. (Cited on page 30.)
- [20] O. Brunner, S. Calatroni, E. Ciapala, M. Eshraqi, R. Garoby, F. Gerigk, A. Lombardi, R. Losito, V. Parma, C. Rossi, J. Tückmantel, M. Vretenar, U. Wagner, and W. Weingarten, “Assessment of the basic parameters of the CERN Superconducting Proton Linac. Assessment of the basic parameters of the CERN SPL,” *Phys. Rev. Spec. Top. Accel. Beams*, vol. 12, no. CERN-AB-2008-067-BI-FR, p. 070402. 35 p, Oct 2008. (Cited on page 2.)
- [21] K. Bryan and T. Leise, “The \$25,000,000,000 eigenvector: the linear algebra behind Google,” *SIAM Review*, vol. 48, pp. 569–581, 2006. (Cited on page 2.)
- [22] T. Butz, *Fourier Transformation for Pedestrians*, ser. Fourier Series. Springer, 2006. [Online]. Available: <http://books.google.de/books?id= XKY30p72gesC> (Cited on pages 45, 48, 50, 51, and 54.)
- [23] D. Calvetti, L. Reichel, and D. C. Sorensen, “An implicitly restarted lanczos method for large symmetric eigenvalue problems,” *ETNA*, vol. 2, pp. 1–21, 1994. (Cited on page 6.)
- [24] C. Cuno, “Randzustände in einem supraleitenden Mikrowellen-Diracbillard,” 2012. (Cited on pages 114 and 115.)
- [25] C. Daniel and F. Wood, *Fitting Equations to Data*. John Wiley, 1980. (Cited on page 56.)
- [26] C. Dembowski, B. Dietz, T. Friedrich, H.-D. Gräf, H. L. Harney, A. Heine, M. Miski-Oglu, and A. Richter, “Distribution of resonance strengths in microwave billiards of mixed and chaotic dynamics,” *Phys. Rev. E*, vol. 71, p. 046202, Apr 2005. [Online]. Available: <http://link.aps.org/doi/10.1103/PhysRevE.71.046202> (Cited on pages 3 and 91.)
- [27] C. Dembowski, B. Dietz, H.-D. Gräf, A. Heine, T. Papenbrock, A. Richter, and C. Richter, “Experimental test of a trace formula for a chaotic three-dimensional microwave cavity,” *Phys. Rev. Lett.*, vol. 89, p. 064101, Jul 2002. [Online]. Available: <http://link.aps.org/doi/10.1103/PhysRevLett.89.064101> (Cited on pages 3, 92, 95, 109, 110, and 123.)

-
- [28] B. Dietz, F. Iachello, M. Miski-Oglu, N. Pietralla, A. Richter, L. von Smekal, and J. Wambach, “Lifshitz and excited-state quantum phase transitions in microwave Dirac billiards,” *Phys. Rev. B*, vol. 88, p. 104101, Sep 2013. [Online]. Available: <http://link.aps.org/doi/10.1103/PhysRevB.88.104101> (Cited on pages 4 and 123.)
- [29] B. Dietz, B. Mößner, T. Papenbrock, U. Reif, and A. Richter, “Bouncing ball orbits and symmetry breaking effects in a three-dimensional chaotic billiard,” *Phys. Rev. E*, vol. 77, p. 046221, Apr 2008. [Online]. Available: <http://link.aps.org/doi/10.1103/PhysRevE.77.046221> (Cited on pages 3, 109, 110, and 123.)
- [30] M. Dohlus, “Ein Beitrag zur numerischen Berechnung elektromagnetischer Felder im Zeitbereich,” 1992. (Cited on page 29.)
- [31] S. Gallagher and W. J. Gallagher, “The spherical resonator,” *IEEE Trans. on Nuclear Sci*, vol. 32, no. 5, 1985. (Cited on pages 82 and 88.)
- [32] R. Geus, “The Jacobi-Davidson algorithm for solving large sparse symmetric eigenvalue problems with application to the design of accelerator cavities,” Ph.D. dissertation, ETH Zurich, 2002. (Cited on page 6.)
- [33] R. Graglia, D. Wilton, and A. Peterson, “Higher order interpolatory vector bases for computational electromagnetics,” *Antennas and Propagation, IEEE Transactions on*, vol. 45, no. 3, pp. 329–342, Mar 1997. (Cited on page 32.)
- [34] G. Hager and G. Wellein, *Introduction to High Performance Computing for Scientists and Engineers*, 1st ed. Boca Raton, FL, USA: CRC Press, Inc., 2010. (Cited on pages 106 and 108.)
- [35] V. Hernandez, J. Roman, and V. Vidal, “SLEPc: A scalable and flexible toolkit for the solution of eigenvalue problems,” *ACM Trans. on Math. Software*, vol. 31, 2005. (Cited on page 6.)
- [36] P. Ingelström and C. tekniska högskola. Department of Electromagnetics, *Higher Order Finite Elements and Adaptivity in Computational Electromagnetics*, ser. Doktorsavhandlingar vid Chalmers Tekniska Högskola. Chalmers tekniska högsk., 2004. [Online]. Available: <http://books.google.de/books?id=uILkAAAACAAJ> (Cited on page 32.)
- [37] Intel, “Intel Math Kernel Library,” 2010. (Cited on page 86.)

-
- [38] J. Jin, *A Finite Element Method in Electromagnetics*. John Wiley & Sons, Incorporated, 1994. (Cited on page 30.)
- [39] W. Kesheng and S. Horst, “Thick-restart Lanczos method for large symmetric eigenvalue problems,” *SIAM*, 2000. (Cited on page 6.)
- [40] E. Kokioioulou, C. Bekas, and E. Gallopoulos, “Computing smallest singular triplets with implicitly restarted Lanczos bidiagonalization,” *Appl. Numer. Math.*, 2004. (Cited on page 6.)
- [41] C. Lanczos, *Linear Differential Operators*, ser. Dover books on mathematics. Courier Dover Publications, 1997. (Cited on page 6.)
- [42] —, “An iteration method for the solution of the eigenvalue problem of linear differential and integral operators,” *Journal of Research of the National Bureau of Standards*, vol. 45, no. 4, pp. 255–282, 1950. (Cited on pages 6 and 64.)
- [43] R. H. Landau, M. J. Páez, and C. C. Bordeianu, *Fourier Analysis of Linear and Nonlinear Signals*. Wiley-VCH Verlag GmbH, 2008, pp. 245–265. [Online]. Available: <http://dx.doi.org/10.1002/9783527618835.ch17> (Cited on pages 40 and 50.)
- [44] R. Lehoucq, D. Sorensen, and C. Yang, “ARPACK users guide: Solution of large-scale eigenvalue problems with implicitly restarted Arnoldi methods,” *SIAM*, 1998. (Cited on page 6.)
- [45] K. Levenberg, “A method for the solution of certain problems in least squares,” *Quart. Applied Math.*, vol. 2, pp. 164–168, 1944. (Cited on page 58.)
- [46] J. Lewis, S. Lakshmivarahan, and S. Dhall, *Dynamic Data Assimilation: A Least Squares Approach*, ser. Dynamic data assimilation: a least squares approach. Cambridge University Press, 2006, no. v. 13. (Cited on page 57.)
- [47] X. Li, *An overview of SuperLU: Algorithms, implementation, and user interface*. Lawrence Berkeley National Laboratory, 2003. (Cited on page 86.)
- [48] M. Mandal and A. Asif, *Continuous and Discrete Time Signals and Systems*. Cambridge University Press. (Cited on page 74.)
- [49] D. W. Marquardt, “An algorithm for least-squares estimation of nonlinear parameters,” *SIAM Journal on Applied Mathematics*, vol. 11, no. 2, pp. 431–441, 1963. (Cited on page 58.)

-
- [50] I. MathWorks, *Curve Fitting Toolbox: for Use with MATLAB® : User's Guide*. MathWorks, 2011. (Cited on page 56.)
- [51] J. Maxwell, *A Treatise on Electricity and Magnetism*, ser. A Treatise on Electricity and Magnetism. Dover Publications, 1954, no. 1. (Cited on page 9.)
- [52] P. Monk, *Finite Element Methods for Maxwell's Equations*, ser. Numerical Mathematics and Scientific Computation. Clarendon Press, 2003. (Cited on page 30.)
- [53] J. Moré, *Levenberg–Marquardt algorithm: implementation and theory*, Jan 1977. (Cited on page 58.)
- [54] I. Munteanu, “Technical Electrodynamics for iCE (Part II: Numerical Simulation of Electromagnetic Devices),” *Technische Universität Darmstadt*, 2011. (Cited on pages 30 and 35.)
- [55] P. Nahin, *Oliver Heaviside: The Life, Work, and Times of an Electrical Genius of the Victorian Age*, ser. Oliver Heaviside. Johns Hopkins University Press, 2002. (Cited on page 10.)
- [56] S. Nash and A. Sofer, *Linear and Nonlinear Programming*. McGraw-Hill Science/Engineering/Math. (Cited on page 57.)
- [57] J. Nédélec, “Mixed finite elements in \mathbb{R}^3 ,” *Numerische Mathematik*, vol. 35, no. 3, pp. 315–341, 1980. (Cited on page 32.)
- [58] K. S. Novoselov, A. K. Geim, S. V. Morozov, D. Jiang, M. I. Katsnelson, I. V. Grigorieva, S. V. Dubonos, and A. A. Firsov, “Two-dimensional gas of massless dirac fermions in graphene,” *Nature*, vol. 438, no. 7065, pp. 197–200, Nov. 2005. (Cited on pages 3 and 112.)
- [59] K. S. Novoselov, A. K. Geim, S. V. Morozov, D. Jiang, Y. Zhang, S. V. Dubonos, I. V. Grigorieva, and A. A. Firsov, “Electric field effect in atomically thin carbon films,” *Science*, vol. 306, no. 5696, pp. 666–669, 2004. (Cited on pages 3 and 112.)
- [60] B. Osgood, “The Fourier transform and its applications (lecture notes),” *Stanford University*. (Cited on pages 42 and 50.)
- [61] H. Padamsee, J. Knobloch, and T. Hays, *RF superconductivity for accelerators*, ser. Wiley series in beam physics and accelerator technology. Wiley-VCH, 2008. (Cited on page 2.)

-
- [62] T. Papenbrock, “Numerical study of a three-dimensional generalized stadium billiard,” *Physical Review E*, vol. 61, no. 4, pp. 4626–4628, April 2000. (Cited on page 92.)
- [63] A. Peterson, S. Ray, R. Mittra, I. Antennas, and P. Society, *Computational Methods for Electromagnetics*, ser. IEEE Press Series on Electromagnetic Wave Theory. Wiley, 1998. (Cited on page 30.)
- [64] D. M. Pozar, *Microwave Engineering*, 2nd ed. New York, NY: John Wiley and Sons, Inc., 1998. (Cited on pages 1, 82, and 88.)
- [65] J. Reitz and F. Milford, *Foundations of Electromagnetic Theory*, ser. Addison-Wesley series in physics. Addison-Wesley Pub. Co., 1960. (Cited on page 82.)
- [66] H. ren Fang and Y. Saad, “A filtered Lanczos procedure for extreme and interior eigenvalue problems,” *SIAM J. Scientific Computing*, vol. 34, no. 4, 2012. (Cited on pages 66, 68, and 69.)
- [67] Y. Saad, “Filtered conjugate residual-type algorithms with applications,” *SIAM J. Matrix Analysis Applications*, vol. 28, no. 3, pp. 845–870, 2006. (Cited on pages 68 and 69.)
- [68] —, *Numerical methods for large eigenvalue problems*, 2nd ed. Society for Industrial and Applied Mathematics, 2011. (Cited on pages 2, 66, 69, and 87.)
- [69] J. Santamarina and D. Fratta, *Discrete signals and inverse problems: an introduction for engineers and scientists*. Wiley, 2005. [Online]. Available: <http://books.google.de/books?id=GZ1RAAAAMAAJ> (Cited on page 50.)
- [70] R. Schumann and T. Weiland, “A stable interpolation technique for fdtd on nonorthogonal grids,” *International Journal on Numerical Modelling*, vol. Vol. 11, pp. 299–306, 1998. (Cited on page 16.)
- [71] H. D. Simon, “The Lanczos algorithm with partial reorthogonalization,” *Mathematics of Computation*, vol. 42, no. 165, pp. 115–142, January 1984. (Cited on pages 66 and 87.)
- [72] G. L. G. Sleijpen and H. A. V. D. Vorst, “A Jacobi-Davidson iteration method for linear eigenvalue problems,” *SIAM Journal on Matrix Analysis and Applications*, vol. 17, pp. 401–425, 1996. (Cited on page 6.)

-
- [73] A. Stathopoulos and J. McCombs, "PRIMME: Preconditioned iterative multi-method eigensolver: Methods and software description," *ACM Transaction on Mathematical Software*, vol. 37, no. 2, 2010. (Cited on page 6.)
- [74] G. W. Stewart, "A Krylov-Schur algorithm for large eigenproblems," *SIAM J. Matrix Anal. Appl.*, vol. 23, no. 3, pp. 601–614, 2001. (Cited on page 6.)
- [75] K. Tang, *Mathematical Methods for Engineers and Scientists 3: Fourier Analysis, Partial Differential Equations, and Variational Methods*, ser. Mathematical Methods for Engineers and Scientists. Springer, 2007. [Online]. Available: <http://books.google.de/books?id=gG-ybR3uIGsC> (Cited on pages 39, 40, 41, 42, 45, 48, and 51.)
- [76] U. van Rienen and T. Weiland, "Triangular discretization method for the evaluation of rf-fields in cylindrically symmetric cavities," *IEEE Transactions on Magnetics*, vol. Vol. MAG-21, No. 6, pp. 2317–2320, 1985. (Cited on page 16.)
- [77] J. Webb, "Hierarchical vector basis functions of arbitrary order for triangular and tetrahedral finite elements," *Antennas and Propagation, IEEE Transactions on*, vol. 47, no. 8, pp. 1244–1253, Aug 1999. (Cited on page 32.)
- [78] T. Weiland, "On the numerical solution of Maxwell's equations and applications in the field of accelerator physics," *Part. Accel.*, vol. 15, pp. 245–292, 1984. (Cited on page 17.)
- [79] —, "Time domain electromagnetic field computation with finite difference methods," *International Journal of Numerical Modelling: Electronic Networks, Devices and Fields*, vol. 9, no. 4, pp. 295–319, 1996. (Cited on page 22.)
- [80] —, "Communication Technology II (Part I: Fields and Waves)," *Technische Universität Darmstadt*, 2009. (Cited on pages 10 and 11.)
- [81] —, "Verfahren und Anwendungen der Feldsimulation I (Skriptum zur Vorlesung)," *Technische Universität Darmstadt*, 2012. (Cited on pages 16, 17, 22, and 28.)
- [82] —, "Skriptum zum Praktikum Verfahren und Anwendungen der Feldsimulation," *Technische Universität Darmstadt*, 2013. (Cited on pages 16 and 17.)
- [83] —, "A discretization method for the solution of Maxwell's equations for six-component fields," *AEU - International Journal of Electronics and Communications*, vol. 31, no. 3, pp. 116–120, 1977. (Cited on pages 5 and 15.)

-
- [84] —, “Finite integration method and discrete electromagnetism,” in *Computational Electromagnetics*, ser. Lecture Notes in Computational Science and Engineering, P. Monk, C. Carstensen, S. Funken, W. Hackbusch, and R. Hoppe, Eds. Springer Berlin Heidelberg, 2003, vol. 28, pp. 183–198. (Cited on page 15.)
- [85] K. S. Yee, “Numerical solution of initial boundary value problems involving Maxwell’s equations in isotropic media,” *IEEE Trans. Antennas and Propagation*, pp. 302–307, 1966. (Cited on pages 10 and 27.)



Danksagung

Während meiner Promotion am Institut für Theorie elektromagnetischer Felder der TU Darmstadt habe ich viel Unterstützung erfahren. An dieser Stelle möchte ich mich bei allen bedanken, die in den letzten drei Jahren zum Gelingen dieser Arbeit beigetragen haben. Insbesondere gilt mein Dank:

- Herrn Prof. Dr.-Ing. Thomas Weiland für die wissenschaftliche Betreuung der Arbeit und für die Bereitstellung der ausgezeichneten Arbeitsumgebung am Institut.
- Herrn Dr.-Ing. Wolfgang Ackermann für die kompetente und hervorragende fachliche Betreuung der Arbeit sowie für die Durchsicht des Manuskriptes.
- Frau Prof. Dr. rer. nat. habil. Ursula van Rienen für die freundliche Übernahme des Korreferats.
- Herrn PD Dr. rer. nat. Erion Gjonaj und Frau Prof. Dr.-Ing. Irina Munteanu für die angenehme und konstruktive Zusammenarbeit.
- der Graduate School of Computational Engineering für die finanzielle Unterstützung in den letzten drei Jahren.
- allen jetzigen und ehemaligen Kollegen des Institutes TEMF und der Graduate School of Computational Engineering für die freundschaftliche und konstruktive Zusammenarbeit.
- den Projektmitarbeiter des Institutes für Kernphysik der TU Darmstadt für die Bereitstellung der Messergebnisse und die angenehme Zusammenarbeit.
- Meinem Bruder M. Banov und seiner Familie für alle ihre Hilfe.
- meinen Freunden, insbesondere A. Pepa, E. Lazovska und J. Mersini.

Meinen lieben Eltern und meinem Freund A. Avdić danke ich für die großartige Unterstützung in den vergangenen Jahren sowie für die bedingungslose Unterstützung in jeder Hinsicht in meinem gesamten Werdegang. Danke!



Curriculum Vitae

Persönliche Daten

Name: Todorka Banova
Geburtsdatum: 22.03.1986
Geburtsort: Shtip, Mazedonien



Ausbildung / Werdegang

03/2011 - 07/2014 Dr.-Ing. in Elektrotechnik und Informationstechnik, Technische Universität Darmstadt, Darmstadt, Deutschland
11/2008 - 11/2010 Junior Lehr- und Forschungsassistentin, FON Universität, Fakultät für Informatik, Skopje, Mazedonien
10/2008 - 05/2010 M.Sc. in Elektrotechnik und Informationstechnik, Universität St. Kyrill und Method, Skopje, Mazedonien
06/2006 - 01/2012 Softwareentwicklerin, Ultra Computing GmbH, Skopje, Mazedonien
10/2004 - 09/2008 B.Sc. in Elektrotechnik und Informationstechnik, Universität St. Kyrill und Method, Skopje, Mazedonien
09/2000 - 06/2004 Gymnasium, Mittelschule Kocho Racin, Sveti Nikole, Mazedonien

BTodorka